——Fakultät für Physik——-

A low noise Laser system for high fidelity Rydberg atom manipulation

February 29, 2019

MAX-PLANCK-GESELLSCHAFT

——Division of Quantum Many Body Systems——-

Masters thesis by:
Joop Age Harm Adema
03698781
ge56sum@tum.de

First evaluator:
Prof. R. Gross
Second evaluator:
Prof. I. Bloch
Supervisor:
Prof. C. Gross

Abstract

In this thesis, I consider a low-noise two-photon setup for accessing Rydberg states in Potassium-39. Originally used grating-based External Cavity Diode Lasers (ECDLs) are replaced by homebuilt interference filter-based ECDLs at 810 and 980 nm. A detailed analysis of ECDLs was performed to characterize the limited single mode behaviour of the 810 nm laser and to find optimal operational parameters. Subsequently, more than 100 mW of 405 nm light was generated by optimization of a previously built Second Harmonic Generation (SHG) cavity around a nonlinear crystal. Furthermore, we obtain approximately 450 mW from a 980 ECDL setup. In addition, in order to reduce excess laser phase noise originating from the Rydberg excitation ECDL, detrimental to experimental coherences in cold Rydberg atom experiments, a high finesse filter cavity was designed and characterized. However, the cavity power transmission at 980 nm is insufficient to directly seed a Tapered Amplifier. The same cavity was used to quantify the phase noise of a constructed 980 nm ECDL. Ultimately, using the constructed ECDLs and SHG cavity, a setup for spectroscopy on a hot Potassium vapour cell was set up. Although finding the $4S_{1/2} \to 5P_{1/2}$ transition was relatively straightforward using a Modulation Transfer Spectroscopy (MTS) addressing both hyperfine ground states, locating the Rydberg line $5P_{1/2} \to 35S_{1/2}$ in wavelength showed more challenging. The relevant Optical Bloch Equations were solved to find the Rabi frequencies that maximize the expected MTS signal and to calculate the expected signal size with respect to the $4S_{1/2} \to 5P_{1/2}$ signal.

Contents

Chapter 1

Introduction

Ultracold atom physics enables the study of many emerging phenomena at low temperatures using both bosonic and fermionic neutral atoms, ranging from optical clocks to quantum information and simulating quantum many body physics in an analog fashion [1]. Excellent control over temperature of a dilute gas enabled observation of a Bose-Einstein Condensate in (BEC) [2, 3] and the quantum degeneracy of a Fermi gas using evaporative cooling [4]. Optical trapping methods have evolved from single dipole traps to optical lattices and arrays of optical tweezers, allowing for varying trap depth and geometry [5, 6, 7]. Detection through quantum gas microscopes allows for detection of atomic signals at single lattice sites [8, 9]. Contrary to the original hosts of quantum many body physics, solid-state systems, the purity, controllability and detectability is superior in cold atom experiments.

Various interesting Hamiltonianshave been realized and phase transitions have been tuned over [10, 11]. To simulate those models, the analog quantum simulator's Hamiltonian needs to map to e.g. the pure Fermi-Hubbard Hamiltonian.To realize more complex Hamiltonians, different interactions than the effective contact interaction for ground state atoms are required [12]. Furthermore, disordered and non-equilibrium systems, frustrated magnetism, topological order and spin models have been simulated and proposed using cold atoms [13, 14, 15, 16].

Spin models can be studied through various interacting mechanisms: dipolar quantum gases of polar molecules [12], Feshbach resonances [17], and Rydberg atoms [16]. The latter is the interaction of the experiment in scope, and has been proposed to construct next-nearest neighbour or even longer range interactions. In order to realize such long-range interacting atom arrays, appropriate ways of cooling, trapping, loading, and detection are required.
The atomic species employed for Rydberg atom-based lattice and tweezer experiments are alkaline or alkaline-earth atoms. The former have a single unpaired s-electron, which dictates a simple electronic level structure, whereas the latter (two s-electrons in the outer shell) is characterized by a singlet-triplet structure, characterized by very narrow transitions, useful to clock experiments [18]. Alkali atoms are very suitable for laser cooling because of the ease of forming closed transitions with only a few laser fields [19]. In order to achieve an ultracold neutral atom setup, multi-stage cooling and trapping are essential prerequisites. Combinations of magnetic and optical traps have been employed to cool atoms down to tens of μK scale. More elaborate methods, such as grey molasses and Raman sideband cooling, allow for sub-Doppler temperatures [20, 21]. Spatial Light Modulators (SLMs) allow for arbitrary arrays of tweezers with high-power [22]. To enhance the loading of the array, carefully tuning light-assisted colli-

sions allows for giving one atom after the collision enough energy to leave the trap but not two. In this case, starting from doubly occupied traps, unity loading can be enhanced [23]. Furthermore, resorting a partially occupied array with an Acousto-Optic Deflector (AOD)allows for preparation of a unity filled array [24, 25].

Atoms with an electron excited to a high principal quantum number n state are called Rydberg atoms. They have caught attention in the last decade especially because of their long lifetime and strong long-range interaction for both quantum information as well as quantum simulation [26, 27]. However, the lifetime of Rydberg atoms limits the physics to a regime where motional dynamics is not at play. The lifetime of several µs suffices to observe the strong dipole-dipole interaction through the blockade of a nearby Rydberg excitation and the implementation of a two-qubit gate [28, 29]. Furthermore, it was shown that the blockade radius initiates spatial structures depending on the wavefunction symmetry [30] and that multiple atoms close to a Rydberg atom behave as an effective two-level atom [31]. Among others, dynamics of XY and Ising spin models have been probed [32, 33], 1D Ising interactions with tunable interactions have been realized [34], Bosonic Su-Schrieffer-Heeger model in two nearby S and P Rydberg states has been realized [35], Greenberger-Horne-Zeilinger states involving many atoms have been prepared [36], and individual Rydberg atoms have been trapped [37].

Next to resonantly exciting atoms to the Rydberg state, off-resonantly addressing atoms enables the preparation of tunable dressed states. Those Rydberg dressed-states state contain an admixture of Rydberg state properties: longer lifetimes are attainable at the expense of interaction strength. The interaction between Rydberg dressed atoms has a soft-core shape, which enables to realize different Hamiltonians than resonant Rydberg excitation. Although not much experimental work has been published, many proposals have been made. Among other experiminents, entangled two-atom state preparation has been shown [38], a resonant alternative to obtain dressed states [39], measurement of dynamics and correlations in a large 2D dressed sample [40], dressing of one of the hyperfine states of Potassium and characterization of the dressing by a Ramsey sequence [41] or generating the transverse field Ising model at a Förster enhanced Rydberg state [42]. It has been shown that atom losses and linewidth broadening in a many-body environment heavily limit coherence times for dressing experiments [43]. In addition, proposals for observing supersolid phases [44], accessing various spin models by dressing both ground states [45] and efficient spin squeezing have been made.

To benchmark Rydberg atom experiments to identify the limiting factors, measuring the number of Rabi oscillation cycles and two-atom gate fidelities can be performed. The Doppler effect, intermediate state scattering, and laser phase noise severely limit those benchmarks [46]. In order to manipulate atoms for the aforementioned purposes, one thus requires stable and low phase noise light sources. It has been shown that laser phase noise reduction is necessary for obtaining high fidelities [47, 48]. This motivated the project presented in this work: the construction and characterization of a laser system for two-photon excitation of Rydberg atoms. The laser system serves a cold atom experiment of bosonic species Potassium-39, which employs Rydberg atoms to study quantum many-body physics. The aim of the experiment is to realize arrays of Rydberg (dressed) atoms with near-arbitrary 2D geometries, interacting through long-range potentials [44].

This thesis proceeds in the following order. In Chapter 2 an introduction to the required atomic physics is given, with a specific focus on Rydberg atom-induced interactions and the limitations of current Rydberg

experiments. Chapter 3 discusses the theory of External Cavity Diode Lasers (ECDLs) as a low-noise optical excitation source and characterizes the homebuilt interference filter-based ECDLs. The setups built with those lasers, amplification stages and frequency doubling is discussed in Chapter 4. Subsequently, Chapter 5 discusses the construction and characterization of a linear cavity to filter phase noise. The optical sources of 4 are employed in chapter 6 to perform a spectroscopy on a hot Potassium vapour cell. Chapter 7 concludes and gives an outlook over future improvements of our setup for two-photon excitation of Rydberg atoms.

Chapter 2

Theory of ultracold Rydberg atoms

To understand the purpose and experimental requirements of the following chapters, this chapter starts with discussing the basic theory behind the experiments and proposals discussed in the introduction: Rydberg atoms and their properties are considered in section 2.1, Potassium atoms as an atomic species to realize Rydberg atoms are discussed in section 2.2 and the limiting factors to current cold atom experiments in section 2.3.

2.1 Rydberg atoms

The discrete level structure of atoms was first universally described by the Rydberg formula in the end of the 19th century. Theoretically, this was explained for the Hydrogen atom by assuming a quantized level theory of a positive and a negative point source with distinct masses leading to an inversely quadratic energy structure. In first approximation, atoms with more than a single electron can be described by solely describing the atoms in the outer shell with principal quantum number n, justified by the partial shielding of the nucleus by the inner electrons. Similar to Hydrogen, alkali atoms (e.g. Rubidium and Potassium) have a single electron in the outer shell with angular momentum $l = 0$. However, the imperfection of the hydrogenic model to account for low-l states being close to the nucleus led to the development of a correction: the quantum defect theory. In this way, atomic levels and their energies E_{nlj} can be characterized by the quantum numbers n, l and j [26]:

$$E_{nlj} = E_{ion} - \frac{R_{red}}{(n - \delta_{nlj})^2} \tag{2.1}$$

Where E_{ion} is the ionization energy of the atom, $R_{red} = Ry/(1 + m_e/m)$ is the reduced Rydberg constant, l is the orbital angular momentum, j the total angular momentum and we simplify $n^* = n - \delta_{nlj}$. m is the nuclear mass and m_e is the electron mass. The defect theory allows for calculation of the radial wavefunctions $|nljm_j\rangle$, which gives access to calculations of the radial transition matrix elements [49]. Rydberg atoms are atoms that have electrons excited to higher ($n \gtrsim 15$) energy levels, obtained through optical excitation. The average radius of the Rydberg atom scales as $\langle r \rangle \propto n^2$. As high-$n$ electrons are spatially separated from the core, Rydberg atoms possess interesting properties, summarized in table 2.1.

The lifetime of Rydberg atoms is fundamentally limited by two processes: the radiative lifetime $\tau_{nl}(0)$

and the temperature-dependent blackbody rate τ_{nl}^{BB}. Adding up both decay rates gives us the effective lifetime of the Rydberg state [50]:

$$\frac{1}{\tau_{nl}(T)} = \frac{1}{\tau_{nl}(0)} + \frac{1}{\tau_{nl}^{BB}(T)} \tag{2.2}$$

Spontaneous emission to all lower lying states $A_{nl} \rightarrow A_{n'l'}$ relates to the radiative lifetime:

$$\tau_{nl} = \left[\sum_{n'l'} A_{n'l',nl} \right]^{-1} \tag{2.3}$$

Where A is the Einstein coefficient, which depends on the initial n, l and final n', l' state:

$$A_{n,l,n',l'} = \frac{4\omega^3}{\hbar c^3} \frac{max(l,l')}{2l+1} \left| \langle n'l' | er | nl \rangle \right|^2 \tag{2.4}$$

The quadratic amplitude is the transition dipole element amplitude known as the (Fermi) golden rule of time-dependent perturbation theory. The strong dependence on transition frequency ω shows that spontaneous emission favours the highest frequency transition. For large n-states, the transition frequency is practically n-independent. As the dipole matrix element (overlap of the wavefunctions) between low-lying and Rydberg levels scales $\propto n^{-3/2}$ for low l states, the radiative lifetime scales independently on n and l for alkali atoms, for which $\beta \approx 3$ [50]:

$$\tau_{nl}(0) = \tau_l \, (n^*)^\beta \tag{2.5}$$

Blackbody radiation is induced by both absorption and emission to other Rydberg states and ionization of Rydberg atoms. The average number of photons occupying blackbody modes is temperature- and frequency-dependent: its lifetime depends approximately on the principal quantum number as $\propto n^2$ and temperature as $\propto T^{-1}$ for large n states [51]:

$$\frac{1}{\tau_{nl}^{BB}(T)} = \frac{4\alpha^3 k_B T}{3\hbar n^2} \tag{2.6}$$

Where α is the fine structure constant. Equations 2.5 and 2.6 show that lifetime drastically increase with n. Using the ARC package [52] for calculating transitions in Alkali atoms we find that until $n \approx 50$, the radiative lifetime is limiting. As the level spacing scales $\propto n^{-3}$, after $n \approx 50$ the blackbody term is the limiting factor.

Another striking property of Rydberg atoms is their large dipole moment, enabling large interactions between two Rydberg atoms. As the excited electron's average radius $\langle r \rangle$ is far from the ionic core, the atom is very sensitive to external electric fields. Likewise, the dipole moment of one atom affects neighbouring atoms. It can be shown that two atoms with dipole moment $\hat{d}$ spaced by distance R interact via the dipole-dipole interaction [53]:

$$V_{dd} = \frac{1}{4\pi\epsilon_0 R^3} \left(\hat{\mathbf{d}}_\mathbf{A} \cdot \hat{\mathbf{d}}_\mathbf{B} - 3(\hat{\mathbf{d}}_\mathbf{A} \cdot \hat{\mathbf{r}})(\hat{\mathbf{d}}_\mathbf{B} \cdot \hat{\mathbf{r}}) \right) \tag{2.7}$$

Where one Rydberg atom is at **A** and the other at **B** and $\hat{\mathbf{r}}$ is the unit vector defining the interatomic axis. In the limit of moderate spacing between the different two-atom states (in other words: the wavefunctions do

Variable	n-scaling
Average Distance to core $\langle r \rangle$	n^2
Polarizability α	n^7
Dipole-Dipole interaction C_3	n^4
van der Waals interaction C_6	n^{11}
Blackbody radiation lifetime τ_{nl}^{BB}	n^2
Natural lifetime $\tau_{nl}(0)$	n^3
Binding Energy E_{nlj}	n^{-2}
Rabi frequency Ω	$n^{-3/2}$

Table 2.1: *Scaling dependency on the principal quantum number n for several relevant quantities [50]*

not overlap) nearby two-atom levels do barely admix. Considering the shift of the eigenenergy of a two-atom state when two Rydberg atoms approach gives an approximation to the interaction: the interaction strength between two atoms in the same (n,l)-state can be written as a van der Waals potential [54]:

$$V_{vdW} = \frac{C^6}{R^3} = \frac{d^4}{\Delta R^6} \tag{2.8}$$

Where Δ is the unperturbed energy spacing between upper and lower atomic level: this scales as n^{-3}, whereas the dipole moment d scales as $\propto n^2$, giving a strong n^{11} dependence of the energy shift and a moderate r^{-6} dependence. In a more realistic setting by taking into account more atomic levels, considering higher l-states, and spin-orbit interaction, the van der Waals coefficient C_6 does not change drastically. More importantly, although C_6 is positive for S-states, and thus repulsive, P and D-states show both attractive and repulsive regimes, changing as a function of n [54]. In addition, P and D-states allow for anisotropic interactions [31].

When this van der Waals shift exceeds both the natural linewidth as well as the excitation laser linewidth, when a single atom is excited, the second atom at distance R is not in resonance any more. As Rydberg levels have small linewidths, usually the power-broadened linewidth Ω (assuming $\Omega \gg \Gamma$)limits the resonance and we arrive at the radius where a second excitation becomes non-resonant:

$$R_b = \left(\frac{C_6}{\hbar \Omega} \right)^{1/6} \tag{2.9}$$

This is usually several μm large, which is an attainable distance by adjacent optical lattice sites and two neighboring optical tweezers. In a setting where two or more atoms are within each others blockade radius, interesting properties arise. The Hamiltonian of N atoms within the blockade radius contains a symmetric (to any 2-particle exchange) eigenstate which has $\sqrt{N}$ enhanced overlap with the groundstate compared to the single atom, at the expense of the other eigenstates that are dark states. A so-called superatom behaves as an effective two-level system, as realized in Rubidium [31]. Therefore, Rydberg excitation of closely spaced atoms is also a way to create entangled states.

2.1.1 Two-photon excitation

Exciting S-shell ground states via an intermediate P level enables access to S- and D-Rydberg states and is achievable using available laser wavelengths (see chapter 4). However, two-photon Rydberg excitation

requires light of two different frequencies. Furthermore, scattering on the intermediate state decreases effective coherence times. The one-photon Rabi frequency is given by:

$$\Omega = \frac{\mu_{if} E}{\hbar} \tag{2.10}$$

Where $\mu_{if} = \langle \psi_f | e\vec{r} | \psi_i \rangle$ is the transition dipole element between ground and excited state, and E is the amplitude of the electric field of the applied resonant field. The former depends on the Rydberg level as $\propto n^{-3/2}$ [50]. In a two-photon excitation at large detuning $\Delta \gg \Omega_1, \Omega_2$, the effective Rabi frequency is given by [55]:

$$\Omega_{eff} = \frac{\Omega_1 \Omega_2}{2\Delta} \tag{2.11}$$

This renders an effective two-level system with a small admixture in the intermediate state, which has a linewidth Γ. This leads to an increased decoherence from the Rydberg state [54]:

$$\Gamma_{dec} = \frac{\Omega_2^2}{4\Delta^2}\Gamma + \frac{1}{\tau_r} \tag{2.12}$$

Here, τ_r is the Rydberg atom lifetime. Furthermore, the non-negligible admixture of the intermediate state and laser noise leads to the following dephasing:

$$\gamma_{deph} = \frac{\Omega_2^2}{4\Delta^2}\Gamma + \gamma_L \tag{2.13}$$

Where γ_L is noise attributable to the laser. The effective decoherence is given by a weighted sum of decoherence and dephasing [31]:

$$\Gamma_{eff} = \frac{3\Gamma_{dec} + 2\gamma_{deph}}{4} \tag{2.14}$$

The scattering rate Γ_{eff} depends on the intermediate state detuning as $\propto \Delta^{-2}$, whereas the Rabi frequency only scales as $\propto \Delta^{-1}$. As the ratio of the Rabi frequency over the effective decoherence rate ($\Omega_{eff}/\Gamma_{eff}$) is to be optimized, optimal detunings are rather large. If one of the Rabi frequencies is substantially stronger than the other, further increasing that Rabi frequency affects effective decoherence quadratically and deteriorates the ratio between the two. Therefore, it is favourable to have similar Rabi frequencies. Furthermore, intermediate states with a relatively low linewidth Γ are favoured. The optimal detuning nevertheless depends on the further experimental design: the more atoms to be be addressed, the lower the effective Rabi frequencies and the lower the optimal detuning. Although generally the aforementioned ratio is less for two-photon excitation than for single photon excitation, there are some advantages to the former. First of all, the recoil energy, leading to motional dephasing, is less for counterpropagating two-photon excitation. Furthermore, detection of Rydberg atoms can proceed without the need of a depumping scheme typical to single photon excitation, but with a resonant laser between the intermediate and the Rydberg state [31]. Ultimately, two-photon excitation provides access to S- and D Rydberg states, whereas one-photon excitation can only achieve P-states.

2.1.2 Rydberg dressing

Next to the resonant driving outlined above, one can dress the atoms to an admixed state by an off-resonant light field. In the simplest case, we obtain an admixture of β in the Rydberg state:

$$|\psi\rangle = \alpha |g\rangle + \beta |r\rangle \tag{2.15}$$

Where β is the admixture of excited state atoms. The combined radiative lifetime $\tau_{eff} = \tau/\beta^2$ of this superposition is higher than that of a pure $|r\rangle$ state, as the ground state is stable.

Contrasting the van der Waals potential between pure Rydberg atoms, the interaction between Rydberg dressed atoms has a soft-core shape. The interaction saturates as $R \to 0$, which renders atoms practically noninteracting and may allow to realize exotic supersolid phases [44, 54]. The dressed interaction strength scales to the two-photon Rabi frequency as $\propto \Omega^4$ [54]. Furthermore, the typical antitrapping of Rydberg atoms to red-detuned optical traps designed to trap ground state atoms is not an issue: for a small admixture β trap depth only reduces slightly. Therefore, read-out of ground-state atoms can be done with higher fidelity than that of Rydberg atoms: adiabatically tuning the dressing back to the undressed case allows for detection of ground state atoms [31]. Whereas Rydberg dressing has been shown for one-photon excitation, to date off-resonant Rydberg dressing in two-photon setups has not been shown because of the large intermediate state decoherence rate.

2.2 Potassium

Potassium has three isotopes that occur naturally. The Bosons ^{39}K (93.26%) and ^{41}K (6.73%) are stable, whereas the Fermion ^{40}K (0.01%) is very long-lived ($\tau_{1/2} = 1.2$ million years) [56]. It is part of the Alkali atoms, meaning that it has a single valence electron, implying a relatively simple atomic level structure. In this thesis we use the most naturally abundant boson, ^{39}K. The nuclear spin of this isotope is $I = 3/2$ [57]. This paragraph discusses the level structure, relevant transition strengths and the advantages of potassium as the atomic species of choice.

2.2.1 Level structure and Rydberg excitation

Potassium has a $4S_{1/2}$ ground state, which has a hyperfine splitting of 461.719 700(5) MHz [58], large enough to optically address a single one, and small enough to bridge by Acousto-Optic Modulators (AOMs). Addressing the Rydberg states can proceed in two distinct ways: by a single photon one addresses P-states or by a two-photon excitation one addresses S-states (leading to isotropic interactions) or D-states. In the former case an UV photon is required. Figure 2.1 shows all atomic levels used in the current experiment. The two-photon excitation via the $5P_{1/2}$ state shown is the so called inverted scheme. The non-inverted scheme uses the $4P_{1/2}$ intermediate state. Table 2.2 shows the dipole moments for the various transitions. The $4P_{1/2}$ (D1) and $4P_{3/2}$ (D2) lines are used for various cooling schemes [20].

Table 2.2 shows the transition frequencies and transition matrix element strength to the $n = 35$ Rydberg state for the various transitions shown in figure 2.1 [52]. Coherent optical sources for those wavelengths (404.5, 975, 767 and 770 nm) are attainable with relatively inexpensive semiconductor lasers, gain chips and nonlinear crystals.

In order to consider which of the possible two-photon excitaton schemes is favoured, we should consider the ratio between effective Rabi frequency and effective decoherence (see equations 2.11 and 2.14). For
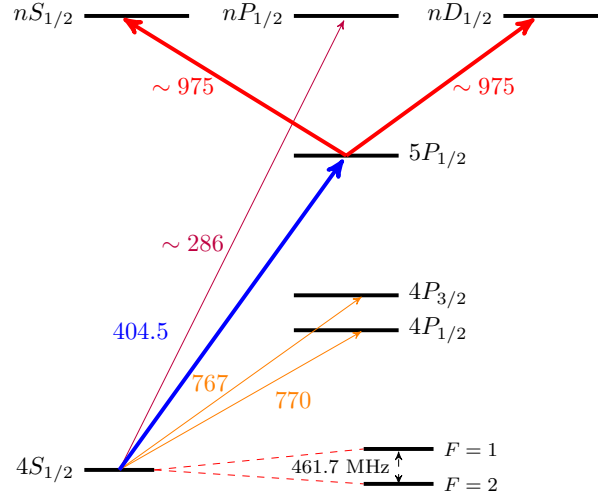
Figure 2.1: *Stylized atomic level structure of K-39. Shown are one- and inverted two-photon excitation to S, P, and D-states and the D1 and D2 lines of the 4P manifold, which are used for cooling and imaging. Intermediate states and transitions are omitted if they do not play a direct role in the current setup. Transitions to Rydberg level are approximate, as they depend on n. The hyperfine splitting of 461.7 MHz of the ground state is shown. The wavelengths of optical transititions shown are in nm.*

both the inverted and non-inverted scheme, the transition to the Rydberg state has a lower dipole element than the transition to the intermediate state. Using the aforementioned sources the inverted scheme might yield a better ratio because of available optical power in the upper transition. As single-mode blue-violet (400-490 nm) laser diodes usually yield very low power and NIR laser diodes and tapered and fiber amplifiers yield up to Watts of power, it is preferred to use the blue-violet light on a transition with higher transition strength. Moreover, the intermediate state decay rate Γ is a factor 5 less for the inverted scheme, reducing the effective decoherence. Therefore, it is opted for to explore the inverted scheme: one requires an optical source at 404.5 nm and one between 970 (ionization) and 990 ($n = 25$) nm. Nevertheless, higher power alternatives for addressing the upper transition in the non-inverted scheme exist [59].

2.2.2 Advantages of Potassium

The workhorse of early cold atom experiments is Rubidium-87. Compared to Rubidium, Potassium has a rather small hyperfine splitting, easily overcome by Acousto-Optical Modulators (AOMs). This allows for laser cooling using less sources and enables to encode spin states in the ground state. Furthermore, Potassium also has a metastable fermionic isotope. Moreover, with the aim of unity filled arrays of atoms, Potassium may have favourable parameters to induce light-assisted 2-atom collisions that supply less energy than the twice the trap depth, allowing only a single atom to escape an optical trap [23].

2.2.3 Attainable Rabi frequencies

In order to discuss the Rabi frequencies that we can obtain on the inverted scheme in Potassium, we turn to the earlier work in our group [60]. As we discussed in section 2.1, the two-photon excitation favours equal Rabi frequencies and therefore we want to maximize $min(\Omega_1, \Omega_2)$. Due to physical constraints, the minimal waist we can focus the 405 nm beam is estimated to be 40 μm. The 980 nm beam can be

Transition	Wavelength [nm]	Transition strength [a_0e]
$4S_{1/2} \to 4P_{1/2}$	770.110	2.366
$4S_{1/2} \to 4P_{3/2}$	766.702	1.673
$4P_{1/2} \to 35S_{1/2}$	456.147	0.011
$4P_{3/2} \to 35S_{1/2}$	457.351	0.008
$4S_{1/2} \to 5P_{1/2}$	404.835	0.159
$4S_{1/2} \to 5P_{3/2}$	404.528	0.117
$5P_{1/2} \to 35S_{1/2}$	979.767	0.022
$5P_{3/2} \to 35S_{1/2}$	981.569	0.015
$4S_{1/2} \to 35P_{1/2}$	286.445	0.001

Table 2.2: *Relevant transitions to non-inverted, inverted and one-photon schemes to $n = 35$ Rydberg states (lifetime is 41 µs), their wavelengths and their dipole transition matrix elements. Wavelengths and matrix element strength are obtained from [52].*

Transition	P_{405} [W]	P_{980} [W]	Ω_{405} [MHz/2π]	Ω_{980} [MHz/2π]
single atom	0.1	0.5	674	3014
many atoms	0.1	0.5	674	61

Table 2.3: *Attainable Rabi frequencies for two different experimental settings using the inverted two-photon excitation $4S_{1/2} \to 5P_{1/2} \to 35S_{1/2}$ in Potassium.*

focused (through a high Numerical Aperture (NA) lens), depending on the setting: address single atoms (focus to 1 µm waist) or the whole 2D array of atoms (focus to 50 µm waist). Table 2.3 summarizes the attainable Rabi frequencies for excitation to a sublevel of $35S_{1/2}$. For single site addressing the blue is the bottleneck, whereas the 980 is for addressing many atoms. The attainable powers reported are achieved in Chapter 4.

2.3 Limitations of current cold atom experiments

When assessing the usefulness of a Rydberg experiment for quantum computing and quantum many body physics, we can define two simple benchmarks: the fidelity of two-atom gates and the number of Rabi oscillation cycles of a single atom that can be completed within the effective coherence time of the atom (see section 2.1). The former has been explored by [47] using Rubidium (an alkali atom), who achieve a fidelity of 0.97(3) for preparing a two-atom entangled state. Recently, a fidelity of 0.995(3) has been achieved in a strontium experiment (an alkaline-earth atom) [48]. The authors of [46] give a detailed analysis of the latter for a Rubidium-based tweezer experiment in the non-inverted scheme (see section 2.2). One can broadly classify two kinds of imperfections: State Preparation And Measurement (SPAM) and dephasing errors.

2.3.1 SPAM errors

State preparation by optical pumping and detection in certain states is not fully efficient. Detection of Rydberg atoms usually relies on detection of non-excited atoms, which is vulnerable to both false positives and negatives, leading to a finite contrast of Rabi oscillations. Underlying those false positives

are background gas collisions, atom dynamics under illumination of cooling light, or losing ground state atoms in the experimental sequence, when the tweezers are switched off. False negatives arise because of a non-zero recapture possibility and subsequent decay of the Rydberg atom to the ground state during detection.

2.3.2 Dephasing errors

Atoms experience dephasing through the Doppler effect, scattering on the intermediate state and laser phase noise. The trapped atoms have a finite velocity spread at finite temperature $\Delta_v(T) = \sqrt{k_b T/m}$ giving rise to an effective spread in detunings of the final excitation laser. By using counterpropagating beams in two-photon excitation, the broadening in detuning is limited. Furthermore, by using Rabi frequencies that exceed the Doppler broadening, the effect is suppressed.

As the intermediate state in Alkali atoms has a finite lifetime, spontaneous emission to other hyperfine and Zeeman levels than the relevat one occurs. This remains an issue at higher Rabi frequencies. This can be overcome by using a single photon excitation (at the expense of a larger Doppler shift) or choosing an intermediate state with small linewidth. The natural lifetime of the Potassium 5P state (for the inverted scheme) is almost an order of magnitude higher than the Potassium 4P (for the non-inverted scheme) intermediate state.

Ultimately, laser phase noise affects Rabi oscillations as the light's phase $\phi(t)$ changes randomly over time. The power spectrum of this phase noise $S_\phi(f)$ typically shows a resonance (larger at larger open-loop gain) near the edge of the bandwidth of the laser stabilization. This originates from an amplification of phase noise due to reduced stability margin of the closed-loop transfer function at the bandwidth edge. For Rabi oscillations with similar frequencies, this amplified noise has a dephasing effect (see section 3.2.2). A readily achievable improvement is the reduction of laser phase noise. Appropriately setting the lock feedback parameters is essential: excess feedback loop gain can increase phase noise within its bandwidth by orders of magnitude. Furthermore, one can actively filter the light by filtering using a high-finesse optical cavity. Active filtering is the route explored in this thesis in Chapter 5.

Concluding remarks

For exciting cold atoms to the $35S_{1/2}$ Rydberg state we require narrow low-noise coherent sources of light. In the inverted two-photon scheme presented we require both a 405 nm and a 980 nm light source. A straigthforward way of providing coherent light is through diode lasers: how to construct and characterize such sources is the subject of the next chapter.

Chapter 3

External Cavity Diode Lasers

Ultracold atom experiments require single frequency, narrow-linewidth, low phase noise and time-stable light sources. Wavelength tunability, temperature and acoustic stability are necessary to meet those requirements. Originally, semiconductor laser diodes had moderate or no anti-reflection coated front facets which enabled lasing from the bare diode. However, free-running laser diodes are characterized by multi-mode behaviour, large linewidths and large phase noise. Those can be effectively reduced using external feedback provided by an external cavity and active frequency stabilization methods.

Previously used Littrow configuration lasers showed limiting behaviour in our laboratory. Those Littrow lasers showed severe jittering when scanned over a cavity resonance, whereas this did not occur for an interference-filter based ECDL at 770 nm (The lowest D1 line in potassium) [60]. This is a known issue for grating-based lasers: they even show strong mechanical resonances when frequency stabilized, which can easily drive them out of lock [61]. Therefore, all one- (1150nm) and two-photon (810 nm and 980 nm) Littrow configuration excitation lasers were replaced by interference-filter based designs.

This Chapter outlines the working principle of External Cavity Diode Lasers (ECDLs) in section 3.1. We consider the theory of linewidth and phase noise of lasers in section 3.2 and of active frequency stability in section 3.3. Section 3.4 presents a recently popularized design which uses an interference filter for frequency discrimination. The homebuilt ECDLs are characterised in section 3.5, with a focus on the linewidth and single mode lasing to benchmark the lasers. Ultimately, the amplification of diode lasers using Tapered Amplifiers is is discussed in section 3.6.

3.1 Working principle

Laser diodes nowadays have a broad range of applications in industry and daily life. Most of those applications (e.g. fiber-optic telecommunications) require long coherence lengths and thus single frequency and low linewidths, precise transversal mode control (e.g. DVD drives), or high power. However, design considerations also vary wildly for different purposes. For atomic physics experiments, many requirements are even far more stringent, such as for Strontium clock lasers [62]. Although there are different types of semiconductor laser diodes that use an integrated grating (so-called Distributed Feedback (DFB) laser diodes), those have larger linewidth and are not as tunable as required for Rydberg excitation (see section 2.1). First of all, to understand the considered diode lasers we consider the working principle of a bare single mode laser diode and the effect that wavelength-dependent optical feedback has to the emission of the laser.

3.1.1 Index-guided laser diodes

The prevailing material for the Near Infrared (NIR) wavelength region are (Al)GaAs-based laser diodes, as its bandgap is in the NIR wavelength range and as it is most efficient in recombining carriers because it is a direct semiconductor [63]. With various doping regions, one is able to constitute a so-called index-guided laser diode, as shown in figure 3.1. The waveguide comprises a small region of (slightly p-doped) GaAs where the carriers recombine and emit light: it is sandwiched in-between a p- and n-doped AlGaAs region, which are connected to the cathode and anode. To ensure optimal confinement of photons in the waveguide, it is buried in lower refractive index areas. The front side of the laser diode is usually Anti-Reflection (AR) coated, whereas the back side is designed to have a high reflectivity. Typical transversal sizes of the active area are around the wavelength of the emitted light, to ensure lasing in the TEM_{00}-mode. Higher order modes cause large spatial inhomogeneities in field and allow for multimode lasing and a large Amplified Spontaneous Emission (ASE) background. The limited size of laser diodes limit the optical output power to about 100 mW, as heating effects would destroy the device otherwise.
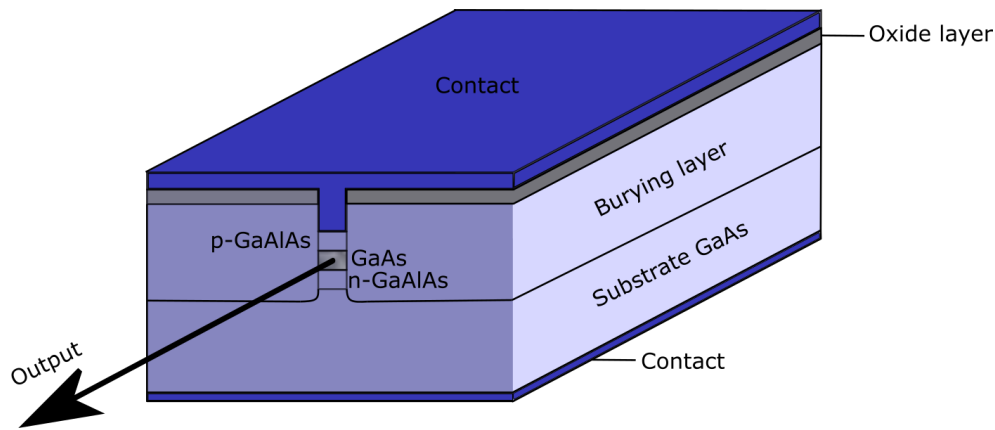

Figure 3.1: *Schematic of a typical index-guided laser diode. The small waveguide in the center is the active region of the p-n junction formed in vertical direction. The cladding around the waveguide has a substantially lower refractive index than the waveguide itself. The back facet of the waveguide is coated to have high reflection, whereas the facet shown is usually anti-reflection coated.*

Different instances of the same product line of laser diodes can show significantly different gain curves due to varying geometry and material quality. For those laser diodes, single scattering centers might affect the gain curve significantly and show a Double Gain Peak (DGP) for spectrally distant modes [64].

3.1.2 Optical feedback

The laser diode presented is a low-finesse cavity with a gain medium inside. Because of the large refractive index of GaAs, the Gaussian mode is partially reflected back (around 35%) into the non-AR coated laser diode, which enhances the field strength. Except for this process of self-feedback, it is also possible to couple in feedback into the laser diode from an external mirror [65]. Providing external optical feedback constitutes a longer laser cavity, reducing the linewidth of the laser (see section 3.2.1.1). It was found that feedback dramatically suppresses the power in side modes [66], whereas bare index-guided laser diodes achieve only 5-10 dB suppression of adjacent longitudinal cavity modes. Furthermore, due to mode competition, intensity noise measured in the dominant mode can be large and anticorrelated to that of other longitudinal modes [67]. Next to providing feedback from an external cavity, feedback

from another laser (a so-called injection lock) or from a cavity-filtered laser (see chapter 5) itself has similar effects [68, 69]. Optical feedback should also ensure that single-mode lasing is sustained, which is discussed next.

3.1.2.1 Regimes of operation

In the simplest case of feeding light back into a laser diode, one places a partially reflective mirror in front of a laser diode. Optical feedback has varying effects for different strengths of external feedback (tuned by different mirror reflectivities), which can be summarized in five categories [70].

1. At minimal feedback levels, less than 1 ppm, it marginally affects the laser operation and linewidth, independent on the phase of the feedback. This regime can be ensured by placing a 60 dB optical isolator after a laser.

2. Increasing the mirror reflectivity up to 30 ppm leads to mode-hopping behaviour when the feedback phase is different, leading to increased noise. This mode-hopping behaviour is not between adjacent cavity modes, but rather a steady state result of two possible resonance frequencies which can be 100s of MHz apart.

3. Further increasing feedback to up to 200 ppm might lead to stable single-mode lasing.

4. In contrast to the previous regime, another very instable regime arises at higher feedback rates: linewidths can become as large as several GHz. Regime 3 allows us to describe carrier density, optical phase and photon density by three coupled differential equations. At higher levels of feedback those equations are coupled in a nonlinear fashion (the so-called Lang-Kobayashi equations) which has no stable steady-state solutions. The coupling between phase and photon density is absent in a bare laser diode, as there is no effect of phase on photon number [71].

5. Ultimately, when feedback levels exceed 10%, the Lang-Kobayashi equations break down: the external cavity is dominating as the laser is lasing on a mode of the external cavity [65]. As the longer external cavity has a much smaller free spectral range than the bare diode, the linewidth of the laser is drastically reduced (see section 3.2). Those lasers are commonly referred to as External Cavity Diode Lasers (ECDLs). In order to obtain high feedback levels, an AR-coated diode is usually required as a non-AR coated surface has a low incoupling efficiency. Nowadays, AR-coatings can be applied to the front-facet which decrease the reflectivity to below 500 ppm. The drawback of feedback is that it lowers achievable output power due to the unavoidable losses in the diode and the elements to provide feedback and possible detrimental effects caused by saturating gain (see section 3.4.2.1.1). This reduces the field strength in the laser diode and therefore the ability to lase without feedback, but facilitates the use of the diode in an ECDL. However, stable lasing still requires appropriate stabilization (see section 3.3).

3.1.3 Wavelength-selective feedback

A major advantage of frequency-selective feedback is that the wavelength of operation is tunable, without changing injection current or temperature. With regular feedback, nearby modes might experience comparable gain rendering operation on a single mode is rather unpredictable and possibly unstable as spectrally distant modes might have comparable gain. By giving frequency-dependent feedback, some modes are favoured over others and it is possible to (roughly) tune the wavelength in a controlled manner. A figure of merit of a single mode's tunability is the mode-hop free tuning range (MHFTR). It is defined

as how much the wavelength can be tuned before it starts lasing on a different cavity mode, which is called a mode hop. A drawback of ECDLs is their limited MHFTR: because of the longer (typically 5 cm) cavity, adjacent modes are relatively close in wavelength and thus face comparable gain. Altogether, optical feedback serves several goals: side mode suppression, wavelength selection, and intensity and phase noise reduction [72].

3.2   Laser linewidth and noise

Laser linewidth and frequency noise are intricately related [73]. As the frequency noise relates to the frequency spectrum of noise itself and the linewidth is a derived property of this spectrum, we firstly consider the frequency spectrum of noise. One can describe the emitted electromagnetic field of a laser by [74]:

$$E(t) = E_0 e^{i2\pi\nu_0 t} e^{i\phi(t)} \tag{3.1}$$

where $\phi(t)$ is a time-dependent random phase, ν_0 is the center frequency, and E_0 is the amplitude. Fluctuations in the phase are related to the frequency ν through:

$$\nu(t) = \nu_0 + \frac{1}{2\pi}\frac{d\phi(t)}{dt} = \nu_0 + \delta\nu(t) \tag{3.2}$$

Here the second term on the right hand side is the frequency change term expressed in terms of the temporal change in phase. Therefore, phase and frequency noise are used interchangeably. The power distribution of those frequency deviations $\delta\nu$ as a function of frequency is denoted as $S_{\delta\nu}(f) \equiv \Delta\nu^2(f)$, which is obtained by Fourier transformation with Fourier frequency f.

$$S_{\delta\nu}(f) = \lim_{T\to\infty}\frac{1}{T}\left|\int_0^T \delta\nu(t)e^{-i2\pi ft}dt\right|^2 \tag{3.3}$$

To consider the effect of those phase fluctuations on the optical spectrum, we calculate the autocorrelation $\Gamma_E(\tau)$ of the electric field E in equation 3.1 at a time difference τ [73]:

$$\Gamma_E(\tau) = E_0^2 e^{i2\pi\nu_0\tau} e^{-2\int_0^\infty S_{\delta\nu}(f)\frac{\sin^2(\pi f\tau)}{f^2}df} \tag{3.4}$$

Here the integral is the Fourier transform of the frequency noise interference between the electric field $E(t)$ and its delayed counterpart $E(t+\tau)$. The lineshape of E is then given through the Wiener-Khinchine theorem:

$$S_E(f) = 2\int_{-\infty}^\infty e^{-i2\pi f\tau}\Gamma_E(\tau)d\tau \tag{3.5}$$

3.2.1   Lineshape and linewidth

Various effects affect the frequency noise distribution and thus the lineshape in distinct ways. Quantum-mechanical shot noise has a white noise spectrum, leading to a Lorentzian lineshape. A usually more

prevalent type of noise is flicker noise: it shows a typical $1/f$-dependence in its power spectral density and originates from noise in e.g. injection current or laser diode dynamics [75]. This type of noise leads to a Gaussian lineshape. As flicker noise is important at very low noise modulation frequencies, it is time-dependent: this leads to the notion of instantaneous linewidth. The instantaneous linewidth is characterised by a small measurement time t which allows us to neglect $1/f$ noise. Hence, this linewidth has no Gaussian contribution and can be modelled as a Lorentzian linewidth. A realistic setting will have both present, which leads to a convolution of both lineshapes: a Voigtian [74]. Moreover, thermal, acoustic and electrical noise are injected when operating an external cavity that is frequency stabilized to an optical reference cavity (see section 3.3).

The authors of reference [73] derive a modulation frequency-dependent cut-off $S_{\delta\nu}^{*} = 8\ln(2)f/\pi^2$, which is coined the β separation line. Frequency noise $S_{\delta\nu}$ above this line does affect the lineshape, whereas below the line it does not affect the lineshape. This originates from the fact that the relative frequency deviation for low-frequency noise is higher in the former compared to the latter case: the modulation frequency is low, but it has a larger impact on the lineshape in the central region. Therefore, a distinct part of the frequency noise spectrum affects the linewidth.

3.2.1.1 The quantum limit and suppression by feedback

Considering an ideal environment without thermal and acoustic noise, the Schawlow-Townes model allows us to consider the quantum limit of a laser cavity emitting light on a single longitudinal mode [74]:

$$\Delta\nu_{S-T} = \frac{\pi h\nu(\Delta\nu_c)^2}{P_{out}} \tag{3.6}$$

Where $\Delta\nu_c$ is the cavity linewidth, P_{out} the optical power, and ν the frequency of the emitted light. However, semiconductor lasers face a higher laser linewidth ($\Delta\nu = (1 + \alpha^2)\Delta\nu_{S-T}$), due to the relation of carrier density on the refractive index: initial spontaneous emission-induced intensity fluctuations lead to enhanced phase fluctuations that increase the linewidth [76]. For typical diode lasers, α takes a value of around 4. Calculating the linewidth for bare diode lasers with an output facet reflectivity of 30% yields several tens of MHz. Optical feedback provides a tool to narrow the cavity linewidth $\Delta\nu_c$.

By means of a much lower cavity linewidth, passive optical feedback through an external cavity of length l_ext can suppress the Schawlow-Townes linewidth of a diode of length l_{diode} with a factor:

$$\left(1 + k\frac{l_{ext}}{l_{diode}}\sqrt{1+\alpha^2}\right)^2 \tag{3.7}$$

Where the coupling factor $k = \sqrt{\frac{R_{OC}}{R_{diode}}(1 - R_{diode})}$ is a measure of the coupling between laser diode cavity and the external cavity. Here, R_{OC} is the reflectivity of the external outcoupling mirror, and R_{diode} is the reflectivity of the front facet of the laser diode. Note that the coupling factor k can not exceed unity, a regime that is usually achieved using AR-coated diodes. The achievable instantaneous linewidth for typical values ($l_{ext} = 1.5$ mm, $l_{diode} = 500$ mm, $\alpha = 4$) are around 1 kHz. Laser linewidths of several kHz are sufficient for excitation to Rydberg states as the broadened linewidth of the transitions is larger. Reduction of $1/f$ noise is possible by active rather than passive feedback, considered in section 3.3.

3.2.2 Phase noise

The concept of the phase noise power spectral density is trivially related (through the Fourier transform of $\nu(t)$ in equation 3.2) to the aforementioned power spectral density distribution of frequency noise $S_{\delta\nu}(f) \equiv \Delta\phi^2(f)$[77]:

$$S_\phi(f) = \frac{S_{\delta\nu}(f)}{f^2} \tag{3.8}$$

This quantity is directly accessible by measuring the PSD of the beat of two identical lasers, or the beat with itself over a distance longer than the coherence length of the source [74].

Phase noise has the most detrimental effect on coherent excitation around the Rabi frequency Ω_R, as noise at low Fourier frequencies $f \ll \Omega_R$ gives a constant phase factor to the excitation pulse. Fast frequency noise $f \gg \Omega_R$ averages out to zero over the length of the Rabi pulse. Hence, reduction of phase noise it is of utmost importance if the bandwidth of frequency stabilisation (see section 3.3) is larger than the attainable Rabi frequencies ($\omega_{servo} > \Omega_R$) [46]. Alternatively, if $\Omega_R \approx \omega_{servo}$, the servo bandwidth can be limited on purpose.

We can asses the effect of laser phase noise on decoherence of a two-level system. Various spin-cycle sequences, such as Rabi oscillations or Ramsey pulses, have different spectral responsitivity to an effective distribution of detunings due to laser phase noise. The function $r(t)$ describes the temporal sensitivity of the excited state population (the amplitude of the Rabi oscillation) to a phase fluctuation . It is defined as [62]:

$$r(t) = 2\frac{\partial \delta p_e}{\partial \delta\phi(t)} \tag{3.9}$$

Considering the Fourier transform of $r(t)$ gives the spectral distribution of sensitivity $R(f)$. This can be analytically obtained and is shown in figure 3.2 using a Rabi frequency of $2\pi \cdot 160$ kHz and a detuning of $\Delta_0 = 100$ kHz.

However, to accurately analyse the effect of phase noise of frequency f on a two-photon excitation, numerical analysis may be required (see e.g. [78]).

3.2.3 Intensity noise

In contrast to frequency noise, intensity noise relates to the fluctuations in the amplitude E_0^2 of the field in equation 3.1. Although typically less detrimental than phase noise [46], the area under e.g. a π-pulse is uncontrolled, leading to damping of Rabi oscillations. Weak suppression of laser side modes is likely to increase intensity noise because of the aforementioned issue of correlated intensity fluctuations, which vanish at larger suppression ratios [67].

3.3 Active Frequency stabilization

Although several alternative methods (e.g. modulation transfer spectroscopy and polarization spectroscopy) for stabilising a laser (often referred to as a 'lock') to an absolute reference exist [79], the Pound-Drever-Hall (PDH) locking technique is most commonly used because of its immunity to amplitude noise and large bandwidth. The PDH lock requires a stable optical reference cavity of high finesse.
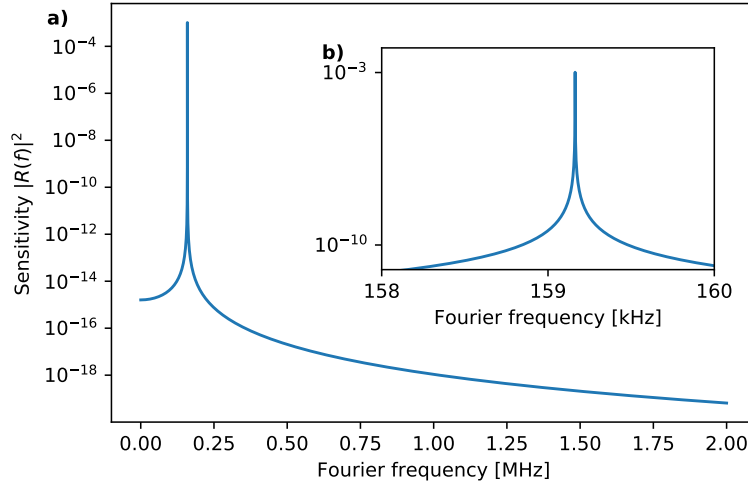
Figure 3.2: ***a)*** *Sensitivity $|R(f)|^2$ of excited state population on the phase noise at frequency f for Rabi Oscillations at frequency 1 MHz. The highest sensitivity is obtained at the frequency $f = \omega/2\pi$ **b)** inset around the Rabi frequency $f = \Omega/2\pi$*

3.3.1 Pound-Drever-Hall lock

The laser is kept on-resonance with the reference cavity by appropriate feedback to tunable elements. In order to provide feedback, we need an appropriate error signal. To derive the error signal, we consider an optical field E_{in} of frequency ω and phase modulation frequency Ω, obtained by an Electro-Optical Modulator (EOM) or modulation of laser diode injection current:

$$E_{in}(t) = E_0 \exp\{i(\omega t + m \sin \Omega t)\} \tag{3.10}$$

Where m is the modulation strength (in our case significantly smaller than unity). The carrier in the power is denoted as P_c and in a single sideband as P_{SB}. The fraction of the field reflected (E_{ref}) by the cavity is given by: $F(\omega) \equiv \frac{E_{ref}}{E_{in}}$. It is frequency dependent because the carrier and two sidebands are reflected differently. On a photodiode we can detect the interference of those fields:

$$\begin{aligned}
P_{ref} = |E_{ref}|^2 = {}& P_c |F(\omega)|^2 + P_{SB}\{|F(\omega + \Omega)|^2 + |F(\omega - \Omega)|^2\} \\
& + 2\sqrt{P_c P_{SB}}\{\text{Re}\{F(\omega)F^*(\omega + \Omega) - F^*(\omega)F(\omega - \Omega)\}\cos \Omega t\} \\
& + 2\sqrt{P_c P_{SB}}\{\text{Im}\{F(\omega)F^*(\omega + \Omega) - F^*(\omega)F(\omega - \Omega)\}\sin \Omega t\} + h.o.t. \quad (3.11)
\end{aligned}$$

Which has a DC component (first line), in-phase components (second line), a quadrature component and higher order terms that we neglect (third line). We should ensure that the modulation frequency Ω is bigger than the transmission width of the cavity ($\Omega \gg \Delta\nu_{\text{FWHM}}$), to ensure that the sidebands are fully reflected when the carrier is fully transmitted: $F(\omega \pm \Omega) \approx -1$ and $F(\omega)F^*(\omega + \Omega) - F^*(\omega)F(\omega - \Omega) = i2\,\text{Im}\{F(\omega)\}$ is purely imaginary, rendering the in-phase term zero. Mixing the signal down with frequency Ω with the correct phase and low-pass filtering the signal to eliminate the other terms of equation 3.11, makes the quadrature term survive and in the vicinity of a resonance peak the quadrature

function is linearly related to the detuning from resonance $\delta\nu$:

$$V_{\text{PDH}}\delta\nu = -8\kappa\sqrt{P_c P_{SB}}\frac{\delta\nu}{\Delta\nu_{\text{FWHM}}} = -k_0 \cdot \delta\nu \tag{3.12}$$

which we call the PDH error signal. κ is an optical power-to-voltage conversion factor, $\Delta\nu_{\text{FWHM}}$ is the transmission linewidth of the reference cavity and k_0 denotes the overall slope of the PDH signal. The linearity of equation 3.12 enables a carefully configured PID-loop to 'lock' the laser to the stable cavity by feedback to the external cavity length (piezo) or laser diode length and temperature (modulating current). An important advantage of the PDH method is that it is rather independent of input power fluctuations, as it does not affect the error signal's offset, but only the slope.

3.3.2 Limits to stabilization

3.3.2.1 Noise

The most fundamental limitation of PDH-locking is given by the photon shot noise [80], which shows a white spectrum. The minimum frequency deviation due to shot noise $\delta\nu_{sn}$ is given by:

$$\delta\nu_{sn} = \frac{\sqrt{hc^3}}{8}\frac{1}{\mathcal{F}L\sqrt{\lambda P_c}} \tag{3.13}$$

Here λ is the wavelength of the incident light, P_c is the power coupled to the cavity, and $\mathcal{F}$ is the finesse of the reference cavity. Regularly used reference cavities are made out of Ultra-Low Expansion (ULE) glass, which are operated at a zero crossing of the thermal expansion coefficient. For such a cavity with finesse $\mathcal{F} = 10^4$, 10 μW of input power leads to a (white) shot noise of around 10 $\text{mHz}/\sqrt{\text{Hz}}$. However, input power should be limited because of heating, which induces thermal noise on the length of the cavity. Furthermore, acoustic noise, pressure and external temperature fluctuations reduce the achievable linewidth of the PDH lock [62].

Furthermore, technical noise in e.g. the photodiode and the mixer limit the attainable linewidth. Accounting for all noise sources, we have a approximate way to calculate the linewidth of a PDH lock with a signal-noise ratio (SNR) of its error signal to a reference cavity of width $\delta\nu_{\text{FWHM}}$ [74]:

$$\delta\nu = \frac{\delta\nu_{FWHM}}{SNR} \tag{3.14}$$

Several effects (such as heating in optical elements) lead to Residual Amplitude Modulation (RAM) of the optical signal coupled to the reference cavity. After demodulating the signal of the reflected field, RAM induces an offset in the error signal and the laser is not stabilized to full transmission through the cavity. Additionally, if an EOM is used to provide the sidebands, the PDH method is susceptible to RAM noise. The EOM's performance depends on the input polarization, which needs to be carefully controlled. Similarly, temperature fluctuations of the EOM crystal can rotate the light's polarization and thus alter the relative power in the carrier to sidebands: it leads to a RAM effect. Therefore, control of the temperature of the EOM crystal is essential to the PDH method [62].

3.3.2.2 Control

To stabilize the laser to the zero crossing of the PDH error signal, we provide feedback through a piezo that changes the cavity length of the laser and the current through the diode. Modulating the length of a cavity

has a straightforward effect: the longer the cavity length, the larger the wavelength. Altering the laser diode current has two counteracting effects. As heating effects (through the increase in refractive index and thermal expansion) dominate the low modulation frequency domain, the sign of $\partial\lambda/\partial I$ is positive: however, at larger modulation frequencies (around a few MHz), this effect is counteracted by carrier effects, reducing the feedback's effectiveness and even reversing the sign of the feedback. Therefore, the bandwidth of effective feedback is limited [81].

3.3.3   Implementation
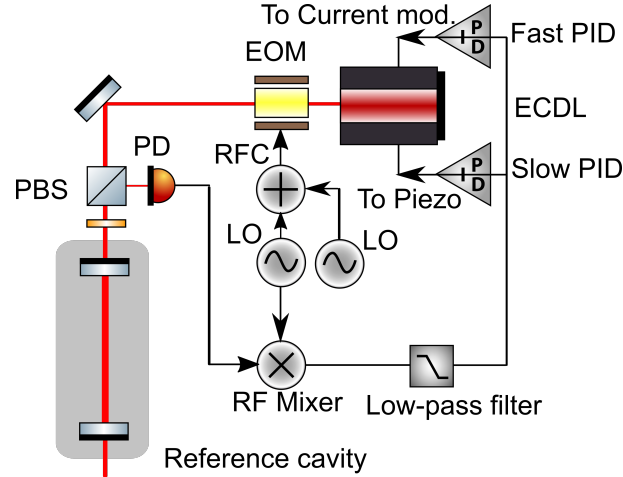

Figure 3.3: *Ourtandard implementation of PDH lock to a stable reference cavity. LO - Local Oscillator, PBS - Polarizing beam splitter, PID - Proportional/Integral/Differential controller, EOM - Electro-Optical Modulator, RFC - Radiofrequency Combiner. An EOM provides sidebands at Ω and optionally Ω_t. The ECDL output is coupled to a reference cavity and its reflection is observed by a photodiode. The photodiode signal is demodulated at the sideband frequency Ω and low-pass filtered to obtain the error signal. Two PID control loops are employed to stabilize the ECDL output to the zero crossing of the error signal. The fast PID controls the current of the laser diode, whereas the slow PIC controls the piezo-electric transducer controlling the laser cavity length.*

Figure 3.3 shows our implementation of frequency stabilization of lasers. A phase modulator (EOM or fiber-coupled EOM) or laser diode modulation supply sidebands for the PDH lock. In the case we want to be able to tune our ECDL frequency in between the modes of the reference cavity, another sideband Ω_t tunable up to half the free spectral range of the reference cavity is given by the EOM. The schematic of the optical and electronic circuit used is shown in figure 3.3.The parts used for the electronic circuits including relevant powers are shown in Appendix C.

3.4   Interference filter-based ECDLs

Various (commercial) designs of grating-based ECDLs are used in atomic physics nowadays. Those grating-based configuration lasers use the angle-dependent feedback of a grating to provide feedback to a laser diode, supporting a narrow wavelength range (around 0.1 nm) [82]. More recently, a different method of providing frequency discrimination gained significant attention in academic literature. However, the initial idea traced back to 1988, where Zorabedian et al. [83] identified the larger alignment

tolerance of filter-based ECDLs. In 2006, a very narrow (0.3 nm FWHM) filter was used to construct an ECDL [84]. It was also shown that a broad (3 nm) filter on the edge of the diode gain curve of a non-AR coated diode could also be used to construct a single-mode ECDL [61].

3.4.1 Design

A schematic of the design of [84] is shown in figure 3.4. The laser diode's emission is collimated by a lens and impinging an interference filter, which transmits a narrow angle-dependent band of the Amplified Stimulated Emission (ASE) background of the laser. A next lens focuses the light onto the partially reflecting outcoupler mirror, with a typical reflectivity of around 30 %. This fraction goes back through the interference filter and is focused into the diode again. The light transmitted through the outcoupler is collimated by another lens.
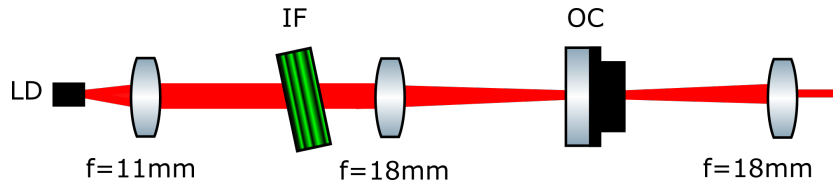

Figure 3.4: *Schematic of the linear interference filter based ECDL. LD - Laser Diode, IF - Interference Filter, OC - Outcoupling Mirror. The outcoupler position is controlled by a piezo-electric transducer.*

The cat-eye reflector geometry is self-aligning and thus mechanically more robust to misalignment: an angular misalignment of the outcoupling mirror only leads to a slight transversal displacement of the reflected light after the lens, which for reasonable parameters does not decrease the feedback by more than 10% [84].

To calculate the center transmission wavelength when impinging the interference filter at an angle θ, we use:

$$\lambda(\theta) = \lambda_0 \sqrt{1 - \left(\frac{\sin\theta}{n_{eff}}\right)^2} \tag{3.15}$$

Here λ_0 is the wavelength at normal incidence, θ the angle with respect to the normal and $n_{eff} \approx 2$ is the refractive index of the interference filter. The sensitivity of the center wavelength on angle is a factor 60 smaller than for regular grating based designs at $6°$, without compromising tunability. This robustness is crucial to prevent detrimental effects from acoustics. Tuning from 0 to $25°$ enables a center wavelength change of around 20 nm.

3.4.2 Frequency discrimination

The gain picture of an ECDL is an intuitive way to understand frequency discrimination in single mode lasers [61]. The cavity, the filter and the gain of the diode determine which modes of the laser cavity are part of the ex-cavity optical spectrum. However, this neglects the reflection and (diode) dynamics that might be crucial to tunability and mode selection, as considered in section 3.1.2. The total gain is the product of the individual elements:

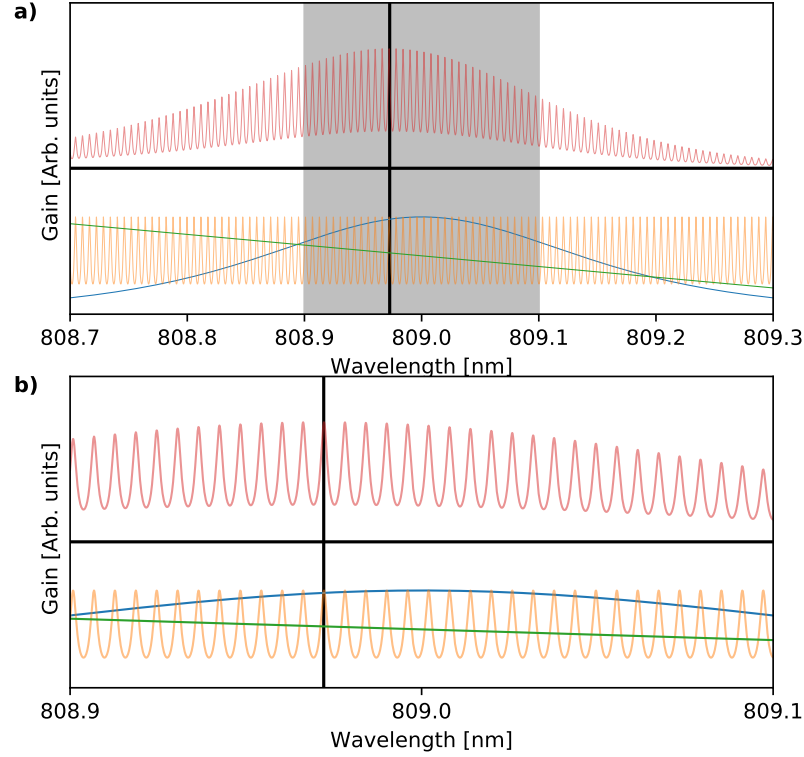$$T = G_D T_f^\alpha T_c \tag{3.16}$$

Figure 3.5: *Longitudinal mode selection in interference filter-based ECDLs.* **a)** *a schematic of the frequency discrimination in an interference-filter based ECDL at 809 nm with a diode gain curve center wavelength larger than 810 nm.* **b)** *a zoom into the shaded area of the upper plot. The pink curve is the product given in equation 3.16, whereas below the G_D (green) T_f (blue) and T_c (yellow) are plotted. The interference filter has been positioned such that the highest diode gain occurs at $\lambda = 809.00$. The laser diode its gain curve peak is located at 780 nm at $25°C$ and is therefore sloping downward. The black vertical line indicates the mode with largest gain.*

The cavity transmission is given by: $T_c = \frac{1}{1+F sin^2(\delta(\nu))}$. Here $F = 4r_1 r_2/(1 - r_1 r_2)^2$ is the coefficient of finesse and $\delta(\nu) = 2\pi n L_D \nu/c$ is the phase shift of a single traversal of the whole cavity. G_D is the gain of the bare diode and T_f is the transmission function of the filter, which has a peak transmission of around 80-90% and is effectively encountered $\alpha > 1$ times, which depends on the reflectivity of the outcoupler and other losses. The product T is shown in figure 3.5 for realistic parameters using the diode later used in 4.1.1.

A limiting factor to this analysis is lack of knowledge of the gain curve of the diode. The producer of the FP diodes specified a measured gain curve, but this gain curve has limited detail. The slope of the diode gain curve over several nm of wavelength range is obtained from the producers note, but small scale features can not be resolved and appear noisy. Nevertheless, by increasing temperature, the gain curve can

be shifted to higher wavelengths and tuned to a different slope of the gain curve. The interference filter has been modelled as a Lorentzian with a FWHM of 0.5 nm, centered at 809.00 nm, with a transmission of 90% and $\alpha = 1.3$. Due to the small facet reflectivity (around 500 ppm for typical AR coatings) the diode transfer function is very close to unity everywhere and therefore it is omitted in figure 3.5 separately.

3.4.2.1 Lasing condition

The discussion in this section follows the approach and nomenclature of [85]. The ECDL is able to lase at cavity modes that have more than unity gain, which depend on the roundtrip losses. This depends on the effective roundtrip gain $\tilde{g}$ per unit length from the diode's stimulated emission exceeds the roundtrip losses by transmission through both facets R_{back} and R_{OC}, the medium itself ($\tilde{\alpha}$), and in the ECDL presented the interference filter T_f. This condition can be written as:

$$R_{back}R_{OC}T_f e^{(\Gamma_a\tilde{g}-\tilde{a})2L} = 1 \tag{3.17}$$

Here, the net gain along the length of the waveguide is an exponential function of the net roundtrip gain coefficient. Γ_α captures the fraction of light emitted into the cavity mode. The gain coefficient $\tilde{g}$ is approximately a logaritmic function of carrier density, which depends linearly on injection current I when $I < I_{th}$. I_{th} is the current at which equation 3.17 is just satisfied. The number of charge carriers n_{th} of the medium at $I > I_{th}$ is independent of the current: the carrier density in the semiconductor does not exceed n_{th} in steady state. In other words, the gain $\tilde{g}$ saturates above the threshold level and therefore operation above the threshold current may induce spatial hole burning.

Considering figure 3.5, several modes have comparable gain. However, the dynamics of the strong feedback regime favours a single mode and suppresses other modes. When the gain profile of the laser is initially largest at a specific cavity mode, a change in e.g. cavity length (which shifts the modes left-right in figure 3.5), might favour another mode. Similarly, a shift in the gain of the diode does only affect the relative gain of modes as the shape of the gain curve has a nonlinear slope. The overtaking of one cavity mode to another is referred to as a mode-hop and is triggered by spontaneous emission. If spontaneous emission over stimulated emission is minimized, even though the next mode has higher even, the laser keeps lasing on a single mode. This enhanced tunability of the laser is captured in the Mode-Hop Free Tuning Range (MHFTR), introduced in section 3.1.3. This also implies a hysteresis of lasing wavelength as a function of adjustable parameters.

3.4.2.1.1 Spatial hole burning

As the gain of the medium is limited because of the available number of carriers, the gain at high optical powers necessarily decreases [86]. This implies that at the antinodes (located at $n\lambda/2$) of the standing wave of wavelength λ in the laser cavity the gain is saturated. On the other hand, in the nodes of this standing wave, the field strength is zero: the gain is unsaturated. Increasing the current further does enhance the optical field in the cavity, which reduces the effective gain at the antinodes. Moreover, an electromagnetic wave that locally has a $\pi/2$ phase shift to the dominant mode faces high, unsaturated gain, and no mode competition with the dominant mode. However, the boundary condition of a node at both ends of the cavity makes it impossible that it is the same mode as the mode that lases: other nearby modes might locally satisfy this condition of a $\pi/2$ phase shift. To illustrate: an alternative mode spaced

by m modes from the dominant wave undergoes a $2\pi m$ phase shift over a length L, meaning a crossing of node at antinode of the dominant wave at $2m$ locations in the waveguide [86]. This effect can be seen as a modification of the gain curve, reducing the effective gain of the dominant lasing mode. Therefore, spatial hole burning has spectral effects.

Stronger feedback (by e.g. a higher reflectivity outcoupler R_{OC}) increases the field in the antinodes, without affecting the nodal gain. As the overlap of a mode m with the dominant mode is independent of m, a regime with severe spatial hole burning has the ability of lasing at many different modes that might have the $\pi/2$ phase shift positions at different positions along the waveguide. A laser that faces those effects might lase single mode at lower injection currents as frequency discrimination is equally strong and gain is not saturated. However, as another mode takes over lasing, the same happens to that mode: mode hopping persists.

3.5 Homebuilt ECDLs

This section presents our realisation of the ECDL of figure 3.4 and characterises the stability and MHFTR of those ECDLs through observing the I, T-behaviour and linewidth measurements of the lasers. Several of those lasers haven been built, with various Eagleyard EYP and Toptica diodes:

- **980A: EYP-RWE-0980-08020-1500-SOT02-0000**

- 980B: EYP-RWE-0980-08020-1500-SOT02-0000

- **810A: EYP-RWE-0810-03010-1300-SOT02-0000**

- 810B: EYP-RWE-0840-06010-1500-SOT02-0000

- *1150: Toptica #LD-1200-0100-AR-1*

The 1150 nm ECDL is part of the one-photon Rydberg excitation setup, which is not part of this thesis. The two boldfaced ECDLs are subject of chapter 4, whereas here we characterise the mode stability of the 980B and 810A and linewidth of the 980A and 810B in the current chapter. All 980 and 810 ECDL are based on doped (Al)GaAS semiconductor junctions.

3.5.1 Design

Figure 3.6 shows a schematic of the main components of the ECDL. For a step-by-step guide of the construction process and parts used, we refer the reader to [87]. The cavity length, from diode to outcoupler, is circa 6 cm. The other design considerations are the width and transmission of the interference filter and the reflectivity of the outcoupler mirror, which both affect the gain picture and effective feedback levels.

3.5.1.1 Optimization

In order to ensure the highest output power and single-mode lasing with the highest possible MHFTR, optimizing the ECDL is essential. To control the temperature of the housing we use a Thorlabs TED200C, and to supply current a Thorlabs LDC202C or LDC205C, connected through a homebuilt protection

---

[1]On the circuit board, a JFET is operated parallel to the laser diode: in this way, modulating the gate voltage, the operating current of the laser diode gets modulated. Nevertheless, when not applying a gate voltage at all, still some current leaks through the JFET. Therefore, the current controller does not indicate the current through the junction accurately, but rather overestimates it by around 30 mA
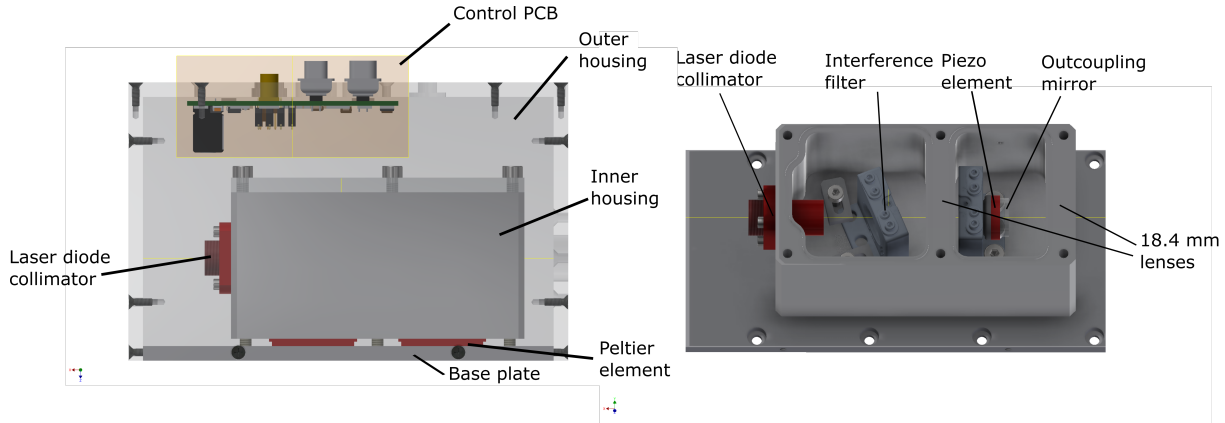
Figure 3.6: *Monolithic Interference Filter based ECDL.* **a)** *shows the external transparent plastic housing that is screwed on the base plate. On that base plate two series-connected piezo-elements are placed below the inner housing, that is connected to the base plate with plastic screws. Below the top lid of the external housing the homebuilt control PCB is placed. It provides current from a current controller to the diode and protects it from a negative current by a parallel diode in opposite direction, connects the thermistor and the peltier to the temperature controller.* **b)** *shows the elements inside the inner aluminium housing. The laser diode is collimated in a SuK 20C collimator that is screwed to the housing. In the first cavity of the aluminium housing an interference filter is placed in a clamped down rotatable mount (Newport HVM-05R). In the center wall the lens* $f = 18.4$ *mm for the cat's eye reflector is screwed. The beam is focused onto the outcoupling mirror, which is glued to a piezoelectric transducer (Piezomechanik HPst 150/14-10/12) that is in its turn glued to a tube that is held by the mount (Newport HVM-05R). At* $2f$ *from the previous lens an identical lens collimates the beam. Not shown are the thermistor, which is (with thermal glue) attached in a hole very close to the collimator tube, the top lid and viton rings that seal this inner housing.*

board[1]. The laser diode output is centered through the bare housing as well as possible and the beam is collimated by tuning the lens position of the collimation tube. This centering process is not trivial as it requires iterative use of tightening and removal of tilting screws; it is described in [87]. Thereafter, the 18.4 mm lenses were put into the housing and the outcoupling mirror was placed. To optimize the feedback, we minimize the lasing threshold. The basic idea of minimization of the lasing threshold is maximization of the incoupling to the laser diode: the lower the current injected into the laser diode given lasing action, the better the coupling efficiency η_c [65]. As adding the interference filter ideally only displaces the beam (see section 3.4), we first optimize lasing threshold without and then insert the interference filter mount. Nevertheless, tuning of the interference filter requires next to rotation around the $\hat{z}$-axis also some rotation around the axis perpendicular to the beam.

3.5.1.2 Feedback levels

Another Master's project achieved single mode lasing of diodes with very similar output reflectivities at 690 nm with no transmission filter a reflectivity of 10% sufficed to obtain single mode lasing for some parameters [88]. Furthermore, a bare non-AR coated laser diode departs the Lang-Kobayashi equations governed regime at around 20%. The 30% reflectivity used in our design is based on [84], who use a interference filter with 80% transmission and an AR coated diode. Nevertheless, the same paper already

Laser	R_{diode}	R_{OC}	$1 - T_{IF}$	F_{eff}	Mode behaviour	Reference
980A&B	$3 \cdot 10^{-4}$	0.31	0.2(01)	0.31	Single mode	This work
810A&B	$3 \cdot 10^{-4}$	0.28	0.15(01)	0.29	Single mode for some I, T	This work
810A	$3 \cdot 10^{-4}$	0.49(2)	0.15(01)	0.64	Single mode for some I, T	This work
633	$3 \cdot 10^{-4}$	0.1	-	0.11	Single mode for some I, T	[88]
853	0.04	0.2	0.2	0.14	Single mode	[84]
Non-AR coated	0.33	0.3	-	0.22	Single mode in some regions	[65]

Table 3.1: *Various effective feedback fractions for various diodes and their reported mode behaviour.*

reported single mode lasing at 20%.

We can estimate the effective feedback of an ECDL given the outcoupler reflectivity R_{OC}, the losses of the interference filter $L = 1 - T_{IF}$ and the diode front facet reflectivity R_{diode}. The effective fraction that in the 1st to the nth reflection enters the AR coated diode is given by:

$$F_{eff} = \frac{(1 - L)R_{OC}}{1 - (1 - L)^2 R_{OC}} \tag{3.18}$$

However, this measure might be inaccurate as coupling efficiencies depend strongly on e.g. collimating optics, diode size and wavelength [65]. Table 3.1 shows the estimated feedback fraction for several lasers and their reported behaviour. The reported behaviour might be inprecise as the ECDLs haven't been subject to similar test conditions. The interference filter transmissions have been measured using another interference filter placed after the lasers and optimized for optimal transmission. Similarly, the reflectivity of the outcoupler mirrors was determined.

The 980 nm laser constructed appeared to lase single mode for all injection currents below the damage level specified by the diode producer and between a temperature of 22°C and 37°C. Most of the reported lasers had lower feedback fractions than the 980 nm laser, which has a 30% reflective outcoupler with a 80% transmission interference filter. On the contrary, the 810 nm laser showed multimode lasing and prolonged regions of mode hopping for two different outcoupler reflectivities. The upcoming paragraph discusses this behaviour in more detail.

3.5.2 Mode stability

In order to have an operable ECDL, it has to lase on a single mode and it should be tunable over required detunings, without the need of relocking the laser to an adjacent mode. Lasers with the largest MHFTR are typically based on non-AR coated diodes and have small external cavity lengths [72]. However, in our experiment several GHz of MHFTR suffices.
We observed that one of the lasers that we build, the 810B, showed barely any single mode lasing. Therefore, it was superseded by the 810A, which is based on a different diode. This laser still showed both mode-hopping and multimode behaviour. An outcoupler with higher reflectivity was used as multimode behaviour might be related to a lack of feedback [84]. To set our lasers to the most favourable parameters and to understand the behaviour of the ECDLs, we want to characterize the mode behaviour as a function of two well-controllable parameters: the temperature of the housing and the injected current [89]. Therefore, we need to sweep those two parameters and observe the DC and AC components of the laser's output

power: different modes have different gain and thus a mode-jump changes the output power of the laser. If such mode-jumps occur continuously, it can be observed in the AC component of the laser output.

3.5.2.1 Obtaining stability map

In order to characterize the temporal behaviour of the laser for various injection currents and operating temperatures, a Python procedure was written. Current and Temperature of the laser were swept by connecting a programmable signal generator (Rigol DG1032Z) to the modulation channels of both a current (Thorlabs TED500C) and a temperature controller (Thorlabs TEC). To consider the low-frequency behaviour of the laser, the DC output of a homebuilt photodiode is connected to a programmable oscilloscope (Rigol DS2000) which, after an equilibration period, records several 10s of ms of waveform data. This is read out by the Python procedure, the Fourier Transform is taken and we separately consider the DC component and the AC components (minimum frequency 4 Hz, maximum frequency 40 kHz) of the signal.

The disadvantage of such a scan is that after setting a new temperature one needs to wait for a period of time until the temperature of the laser housing (and thus the diode) is stable: it requires several hours to complete. Furthermore, using a standard signal generator limits the resolution of the scan as we can't supply a voltage to the temperature and voltage controller more precise than 2mV per 1000 seconds. The slope of the temperature controller and voltage controller are very linear and thus we can accurately determine the axes.

3.5.2.2 Effect of temperature and current on mode behaviour

Changing current and temperature has various effect on the operation of the ECDL: those are summarized in table 3.2. The peak of the gain curve crucial to mode selection described in section 3.4 depends on the bandgap of the (doped) semiconductor. The effect of heating in GaAs has a well defined effect on the bandgap and thus on the peak gain [90]:

$$E_g(T) = 1.519 - \frac{T^2}{T + 204} 5.404 \cdot 10^{-4} \tag{3.19}$$

Which has an effect of $0.14 \ \mathrm{nm \, K^{-1}}$ on the gain curve peak at typical operating temperatures. Thermal expansion of the aluminium cavity, which has a thermal expansion coefficient $\alpha = 24 \cdot 10^{-6} \ \mathrm{K^{-1}}$, contributes to a shift of modes of $0.019 \ \mathrm{nm \, K^{-1}}$ (810 nm) and $0.023 \ \mathrm{nm \, K^{-1}}$ (980 nm). Nevertheless, the external cavity modes are periodic with 2.5 GHz, which is reached at a temperature hike of only 0.029 K and 0.035 K only, respectively.

Similarly, the diode expansion shifts the modes by $0.00046 \ \mathrm{nm \, K^{-1}}$ (810 nm), corresponding to 2.1 $\mathrm{GHz \, K^{-1}}$ for a cavity length of 1500 μm of GaAs[2]. A more important effect of heating of the diode is the change is the change in refractive index due to the increase in the number of carriers: in GaAs the refrective index increases by $5 \cdot 10^{-5} \mathrm{K^{-1}}$, which shifts the modes by $0.0046 \ \mathrm{nm \, K^{-1}}$. Next to effects on the mode behaviour, the gain curve peak shifts: this leads to a modest change in output power.

Those factors affect the gain curve and the shift of modes. Those both affect the gain picture drawn in

---

[2]This also implies that a non-AR coated diode of this size needs to be tuned up to 14°C to match the mode of the external cavity

Parameter	Effect	Wavelength selection	Other
$T \uparrow$	$T_{diode} \uparrow$	Gain curve peak $\lambda_p \uparrow$	$P_{out} \uparrow (\downarrow)$ if $\lambda_p < (>)\lambda$
$T \uparrow$	Thermal expansion housing	Modes move to higher λ	Possible misalignment
$I \uparrow$	$T_{diode} \uparrow$	Modes move a bit to higher λ	-
$I \uparrow$	$T_{diode} \uparrow$	Gain curve peak $\lambda_p \uparrow$	-
$I \uparrow$	Carrier density $n \uparrow$	Modes move to higher λ	$P_{out} \uparrow (\downarrow)$ if $\lambda_p < (>)\lambda$

Table 3.2: *Expected effects on the wavelength selection of adjusting temperature and current of the housing and the laser diode, respectively.*

equation 3.16 and thus the stability of single mode lasing and the susceptibility to mode-hopping[3]. Spatial hole burning, imperfect incoupling or inhomogeneities in the gain medium might all give rise to low mode competition and co-existence of modes. A combination of the slope of the gain curve and the interference filter affects the likelihood of mode-hopping.

3.5.2.2.1   Stability maps for 980 and 810 nm ECDLs

Figure 3.7 reports the stability map of two lasers: the 980B and the 810A with two different outcoupler mirrors. A few datapoints with a value far off the scale are deleted: those are attributable due to a faulty scope readout, caused by zooming in (which is a necessary step for detailed readout for varying DC photodiode voltages) to the wrong voltage range. The results for the DC result of the 980 (**a**)) and 810 nm (**b), c**)) look similar: we observe a DC component that scales positively to injected current and around 15 lines of equal power that have a negative slope that are regularly spaced. These lines are separated by extended regions of continuous signal: this is a stable supported mode, whereas the lines indicate a change in output power. Using a simultaneously coupled cavity (Sirah EagleEye), it is verified that the downward sloping ridges are the border between two modes. The ridge spacing is lower at lower resistances, as temperature does not scale linearly to resistance, but rather $\propto 1/R$. The origin of the negative slope is that both the housing temperature as the injection current increases the actual diode temperature. The 810 nm laser with 30% outcoupler has a lasing threshold that depends on temperature much more than the 50% outcoupler: this is attributed to an initial misalignment that worsened due to thermal expansion.

The 980 nm ECDL's AC component is very low for all values of I and T. The mode-hops happen instantaneously, and no sustained range of modehopping is observed. This is very favourable behaviour for our experiment: the laser do not need to be adjusted continuously to prevent multi-mode lasing by carefully selecting a wavelength far away from the nearest mode hop. The 810 nm laser with a 30% outcoupler shows a different behaviour: at both low and high temperatures, there are extended ranges of mode-hopping. This reduces the effective MHFTR. Examination of the individual Fourier components showed that mode-hopping occurs at frequencies below 50 Hz.

---

[3]Semiconductor laser diodes are often described in terms of the photon and carrier rate equations. [89] present a model of two adjacent modes and considers the mode behaviour. Treating spontaneous emission in both modes as a random variable (the so-called classical Langevin equation), one is able to derive a Fokker-Planck form PDE for the probability distributions of the field strength. Depending on the gain, saturation and cross-saturation parameters, the solution for the steady-state probability distribution is either centered at one mode or at the two modes, separated by a potential barrier. The co-existence of two modes is possible if the cross-saturation (mode competition) is low with respect to the self-saturation. The potential barrier height determines the rate of mode hopping. Among others, this barrier depends positively on the difference in gain between the two modes and negatively on the extent of mode competition between the two modes.
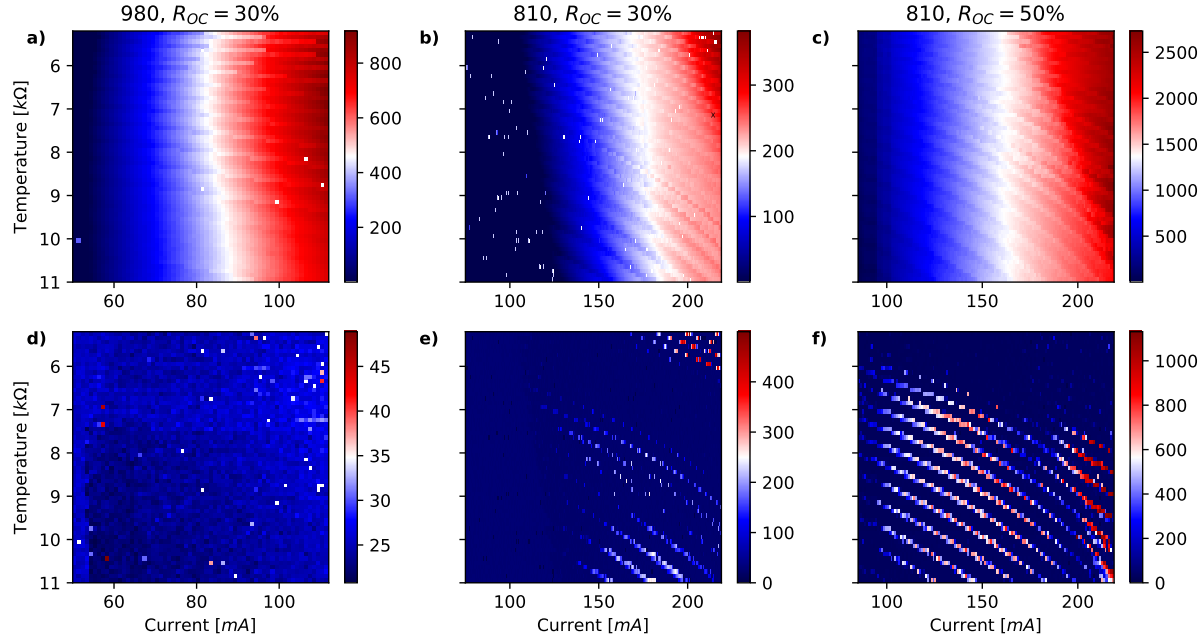
Figure 3.7: I, T-stability maps of photodiode voltage of DC (**a**), (**b**), (**c**)) and AC (**d**),(**e**), (**f**)) components for the 980B ECDL (**a**), (**d**)) and a 810A ECDL with a 30% (**b**),**e**)) and 50% (**c**), (**f**)) outcoupler. The DC signal scales linearly to laser output power, whereas the AC signal is the sum of all Fourier components between $f_{min} = 4$ Hz and $f_{max} = 40$ kHz. The inverse temperature is given as the resistance of the thermistor of the ECDL: the minimum (maximum) resistance R_{min} (R_{max}) corresponds to a temperature of $37°C$ ($21°C$).

In the middle temperature region of the 810 nm the AC ridges vanish and the DC ridges become less intense. It was nevertheless observed that there were multiple modes lasing simultaneously using the coupled cavity. To investigate this behaviour, a wavemeter (High Finesse WS6-600) is used to observe the modes of the ECDL. We observe that in this middle regime several mode-hops of 9 free spectral ranges of the ECDL (corresponding to 22 GHz) apart [4]. Considering the gain curve (which is strongly sloping downwards as a function of wavelength) it is plausible that the gain curve slopes steep enough, that the product of the interference filter and the gain curve shows a double peaked spectrum. At even higher temperature (and current) we observe a return to mode-hopping phases. As the total shift of the cavity modes is periodic with FSR_{ECDL} its effect is much smaller than the total shift of the gain curve because of a change of temperature and carrier density, the behaviour normal to the ridges is dominated by changes in the gain curve slope. Therefore, the transitory multimode behaviour might be well explained by encountering a flatter part of the combined gain curve T encountered in equation 3.16.

Furthermore, increasing the outcoupler reflectivity to 50% did not reduce the prolonged mode hopping regimes. Furthermore, a similar region with multimode behaviour and no mode-hopping is observed. In addition, mode hops strictly continue down to the lasing threshold: this makes it unlikely that spatial hole

---

[4]In comparison, for the 980 nm laser, the mode hops occur between modes that are less than 3 modes away. Please note that a laser with a large MHFTR also mode hops between modes that are spaced many free spectral ranges apart. However, in that case the number of mode hops observed in figure 3.7 would be much less than 15

burning effects are responsible for the deviating behaviour. As with the 30 % outcoupler, a period with sustained multimode behaviour arose.

3.5.2.2.2 Wavelength tuning

As considered in section 3.4, broad tuning of the interference filter enables to select the wavelength roughly. Given the temperature and current, this enables to select the wavelength at a precision of around 4 free spectral ranges of the ECDL (10 GHz). Next to current and temperature, the piezoelectric transducer is a third element that is able to finely tune the ECDL. Very fine tuning (below 1 MHz bandwidth) to stabilize the laser is performed by the piezo, but broad tuning (several free spectral ranges) is also possible. The maps of figure 3.7 have been produced at 0 V supplied to the piezo crystal. Changing this voltage changes the length of the ECDL cavity: this moves the features of figure 3.7 perpendicular to the ridges periodically with a period equal to the free spectral range of the ECDL. The wavelength changes gradually until an instantaneous mode-hop or continuous mode-hopping is encountered. To ensure stability and prevent mode-hopping to adjacent modes as much as possible, current and temperature need to be changed as such that the desired wavelength is in the middle of two mode-hops in figure 3.7 **a), b),c)** and that the piezo is in the middle of its range. Ultimately, as the 810 nm laser does not show single mode behaviour in any range of current and temperature, the most favourable condition have to be selected for operation. As the region where mode-hopping is absent is characterised by multimode behaviour, it is hard to observe the proximity of mode-changes: this poses the risk of a gradual decrease in power in the right mode. Therefore, the operating temperature and current should be tuned to avoid multimode operation.

3.5.3 Linewidth

The linewidth of a single laser can be estimated in several ways. An involving but accurate method is either self-homodyning of self-heterodyning [91]. A less costly way is to heterodyne the ECDL with an identical ECDL: we can approximate the linewidth of the spectrally broadest laser by analyzing the beat note of the two. The PDH error signal is a way to estimate the linewidth when locking, but is less accurate: the height of the error signal is a measure of how large the difference between the resonance and the actual frequency is. The slope of the PDH discriminator is derived from the unlocked signal, which is affected by the free-running jitter of the laser when slowly sweeping over the resonance. However, a faster sweep faces the issue that the photon storage time in the cavity is finite, limiting the achievable resolution [92]. Using the PDH error method, the linewidth over 1ms of the previously built 810 nm and 980 nm Littrow lasers was estimated to be 37 and 1.6 kHz, respectively [60]. To characterise the linewidth of our homebuilt ECDL, we use a commercially available frequency-discriminator-based linewidth analyzer.

3.5.3.1 Linewidth analyzer

We were able to use a low-noise linewidth analyzer (High Finesse LWA-1k), which can measure linewidths down to a few kHz. This should be sufficient to analyse the free-running linewidth of our ECDLs. The linewidth analyzer is an interferometer that transforms frequency- into amplitude noise and amplitude fluctuations are detected. The estimated linewidth is derived from the Fourier spectrum of frequency fluctuations above the β separation line rather than from an optical spectrum measurement, see section 3.2 for an explanation. Figure 3.8 shows the lineshape of two different lasers (810B and 980A). In **a)** and **b)** observe the lineshapes of the 980 nm and 810 nm laser both locked and free-running, and after the Tapered Amplifier (TA) for the 980. When free-running, the laser jitters around freely, increasing the

linewidth significantly (blue traces). Surprisingly, the noise at higher frequencies is significantly higher for the 810 nm laser w.r.t the 980 laser. For the 810 nm laser the servo bandwidth is clearly visible: a bump can be observed at 600 kHz. For the 980 nm laser (right) we suppressed the servo bump by decreasing the gain. Interestingly, the lineshape is much narrower after the TA than it is before: this seems an odd result, as the coherence of a TA chip is usually limited by its seed. It is therefore plausible that it is an erroneous measurement.

In **c)** and **d)**, we fit the lineshapes of the locked lasers to a Voigtian line profile, which is the convolution of a Gaussian and Lorentzian, with a single amplitude but different Full Width at Half Maxima (FWHMs) σ_G and γ_L, respectively. This enables to separately fit the instantaneous linewidth (Lorentzian) and the broadened linewidth (Gaussian), which can be used to identify excess noise sources or bad frequency stabilization [93]. Both the locked and free-running linewidth of the 810 nm ECDL were much higher than that of the 980 nm ECDL. The 980 nm ECDL shows a linewidth very comparable to the estimated linewidth of a grating-based ECDL with the same diode [60].
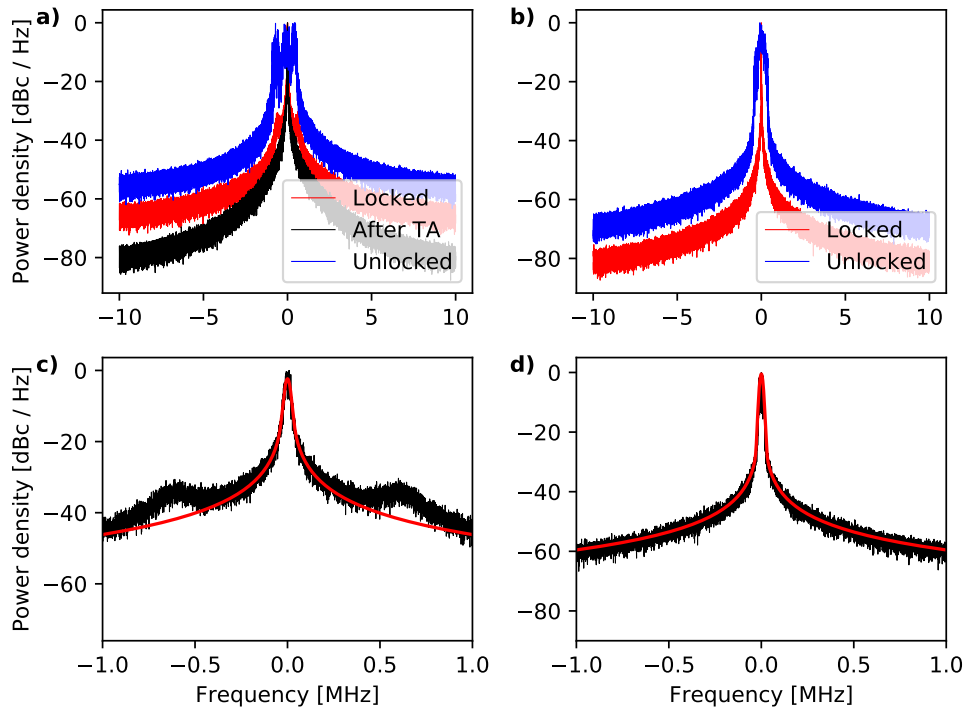

Figure 3.8: *Lineshapes of two different lasers. **a)** lineshape of locked, after-TA, and free-running 810 nm laser. **b)** lineshape of locked, and free-running 980 nm laser. The free-running FWHM linewidth of the 1200 kHz for the 810 laser, and only 240 kHz for the 980 laser. **c)** Voigt fit of the locked 810 nm laser with $\sigma_G = 13.5$ kHz, $\gamma_L = 3.6$ kHz. **d)** fit of the locked 980 nm laser with $\sigma_G = 18$ kHz, $\gamma_L = 1.8$ kHz. The integration time used in all figures is 20 ms.*

The fit parameters are given in figure 3.8. As we fit the Voigtian profile to the 980 nm, the contribution of the peak is much more important than that of the tails. To fit it properly, we use the natural logarithm of the y-axis to give more importance to the peaks. This enabled us to properly fit the curve.

As we discussed in section 3.2, we can distinguish the instantaneous linewidth by observing the Lorentzian from the broadened linewidth that takes a Gaussian lineshape. Comparing the 810 nm and the 980 nm

laser, the latter has a 4 times lower instantaneous linewidth than the former. The difference between the free-running linewidths is also remarkable: the 980 nm laser shows much lower linewidth: this might be the result of unstable mode behaviour observed in the 810B ECDL leading to noisy dynamics. As the mechanical design is the same and both the 980A and 810B are located at the same table, it sees that the origin of the larger linewidth of the 810 nm ECDL is a result of its unstable behaviour.

3.6 Power amplification

In order to amplify the signal substantially, we use Tapered Amplifier (TA) chips [94]. Tapered Amplifiers can be used as a laser when the facets are high-reflection coated and it is given frequency dependent feedback. However, a more common approach is to seed an anti-reflection coated TA chip with a coherent source. Whereas the laser diodes described in section 3.1 are limited in size to ensure single mode lasing and thus in power due to heating, the TA chips are larger and the electrical contacts have a characteristic tapered design with an opening angle of around $6°$. The input is at the narrow input of the gain region, whereas the output tapers outward: this design enables seeding by a high intensity laser without lasing on an own cavity mode. Along the length of the chip, the optical gain from the previous part ensures that although the gain area is larger, stimulated emission exceeds spontaneous emission. Thus, when properly seeded, the TA outputs coherent light in the same longitudinal mode as the seed. Nevertheless, the inherent design of the gain chip delivers an astigmatic beam. Typical curves for output power and temperature for the TAs we use can be found in [60].

Concluding remarks

The interference filter-based External Cavity Diode Lasers presented in this chapter have been built to establish suitable sources for two-photon Rydberg excitation. The free-running linewidth of the 980 nm ECDL was found to be only 240 kHz, whereas the measured linewidth with active frequency stabilization was 1.8 kHz only. Furthermore, for all currents and temperatures considered, it lases single mode. The 810B laser characterised in section 3.5.3 has been discarded because of its multimode lasing behaviour. It has been replaced by the 810A ECDL in section 3.5.2, which shows extended regions of single-mode behaviour. Changing the outcoupling mirror reflectivity did not eliminate the regions of mode hopping, but the laser is operable at the expense of regular remodification of current and temperature. The appearance of mode-hopping and multimode lasing in the 810 nm ECDL is considered to be inherent to the diode and is likely affected by the temperature-dependent slope of the gain curve at the wavelength of interest. The next Chapter will focus on the use of the ECDL characterized in this Chapter: setups to provide frequency-stable light sources at high power will be presented.

Chapter 4

Laser systems

This chapter discusses the revised excitation laser systems. Most setups rely on the work of [60], but several adjustments have been made. Foremost, seed lasers have been changed to interference filter-based ECDLs, that have shown to be more robust to acoustic noise [84]. Furthermore, filters have been added to block the Amplified Stimulated Emission (ASE) background, beam-shaping was optimized to provide optimum power to the experiment and the previously built SHG cavity was altered to give more than 100mW of 405 nm light. First of all, we consider the 405 nm setup that (section 4.1) uses the 810A seed ECDL from Chapter 3 and a Second Harmonic Generation (SHG) stage. Secondly, we consider the 980 nm setup using the 980A ECDL seed (section 4.2).

4.1   405 nm setup

4.1.1   810 nm ECDL

The current setup for the 810 nm is shown in figure 4.1. The diode gain peak at 25°C is located at 840 nm for the former and 780 for the latter. Although it shows regions where it lases multimode, there are extended regions in (I, T)-space where we can operate single mode with an acceptable Mode Hop Free Tuning Range (MHFTR) of around. Around the wavelength of the $4S_{1/2} \rightarrow 5P_{1/2}$ transition that we want to address, we obtained a MHFTR of 4 GHz.

Figure 4.1 shows the setup used to provide stable single-mode laser and high power in the optical fiber to the experimental table. The optical output of the ECDL is linearly polarized and only slightly astigmatic: no further beam shaping is required. 55 dB of backreflection isolation is provided by two optical isolators. A branch of 2.5 mW (a waveplate and beam sampler control the power reflected) for the wavemeter (coupled into fiber by a Thorlabs F230APC-780 collimator) and the lock to the transfer cavity (coupled into fiber by a Thorlabs F230APC-780 collimator) is coupled out by a beam sampler. The lock is in accordance to the implementation shown in figure 3.3. The subsequent lock of the transfer cavity to a more stable cavity is described in 4.1.2.1. Previously, an EOM in the setup provided for the sidebands of the PDH lock. This EOM has been replaced by a fiber-coupled EOM (EOSPACE PM-0S5-10-PFA-PFA-810), as we want to give the light both a sideband for the PDH lock, as well as a sideband of up to 1/2 of the FSR of the transfer cavity (1.15 GHz) [60]. The free-space EOM crystal shown is used for the lock of the SHG cavity, as described in section 4.1. The TA (Eagleyard EYP-TPA-0808-02000-4006-CMT04-0000) is seeded with 25 mW of light to achieve 2.2 W of output power (the TA its maximum rating).

The TA housing has a tunable 18.4 mm lens before and after the gain chip, to optimize incoupling and to collimate one direction of the output. As the TA output is heavily astigmatic (see section 3.6), a cylindrical lens is used to collimate the second direction of the TA output beam. A concave-convex telescope pair of lenses ensures the right beam size for incoupling into the fiber collimator (SuK FC-F-4-M5-10). To prevent backreflections a optical isolator (Thorlabs IOT-5-780) with 23 dB attenuation is placed in after the TA. To filter out any background spontaneous emission, the same interference filter as used in the ECDL is employed, which transmits 85% of the light. A waveplate ensures the correct polarization for the polarization-maintaining fiber. Around 800 mW is coupled into the fiber further used in section 4.1.
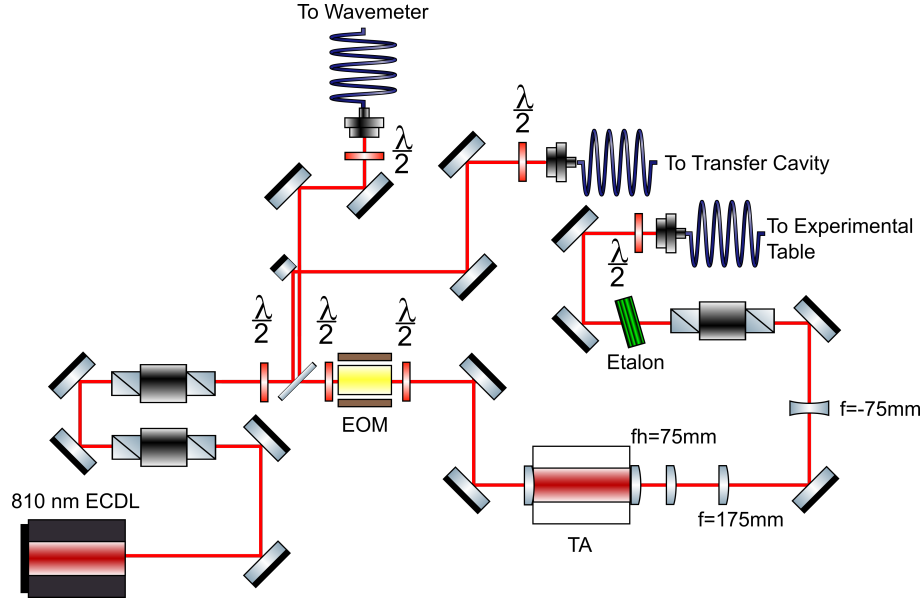

Figure 4.1: *Setup of 810 nm laser until fiber coupling, which continues in figure 4.5. EOM - Electro-Optical Modulator, TA - Tapered Amplifier, f - focal length of a normal lens, fh - focal length in horizontal direction of a cylindrical lens.*

4.1.2   Characterization

Figure 4.2 shows the output power of the laser: this measurement is a cross-section of figure 3.7 at $T = 25(1)°$C (green), $T = 30(1)°$C (blue), and $T = 37(1)°$C (red) for the outcoupler reflectivity $R_{OC} = 30\%$ and at $T = 30(1)°$C for the outcoupler reflectivity $R_{OC} = 50\%$ (black). At higher temperature both the threshold current as well as the slope efficiency is higher: this is the result of the higher diode gain as the gain curve peak is closer the the transmission filter maximum at higher temperature. However, the slope of the curve obtained using the 50% outcoupler does not show changing slopes, but only deviant jitter during mode hopping. The gradually decreasing slope efficiency is likely to be caused by gradual misalignment due to an initial misalignment. Increasing the outcoupler reflectivity increases R_{OC} in equation 3.17, which lowers the current required to fulfill the lasing condition. This increases the threshold current. Nevertheless, as the losses in the cavity are nonzero, the slope efficiency decreases as well. The maximum rating of the ECDL at 810 nm is at around 70-80 mW.

Figure 4.3 shows the lock of the 810 laser to the unstabilized transfer cavity. A step-by-step overview of the locking electronics can be found in figure C.1. The PDH sideband given is at 12 MHz, which allows
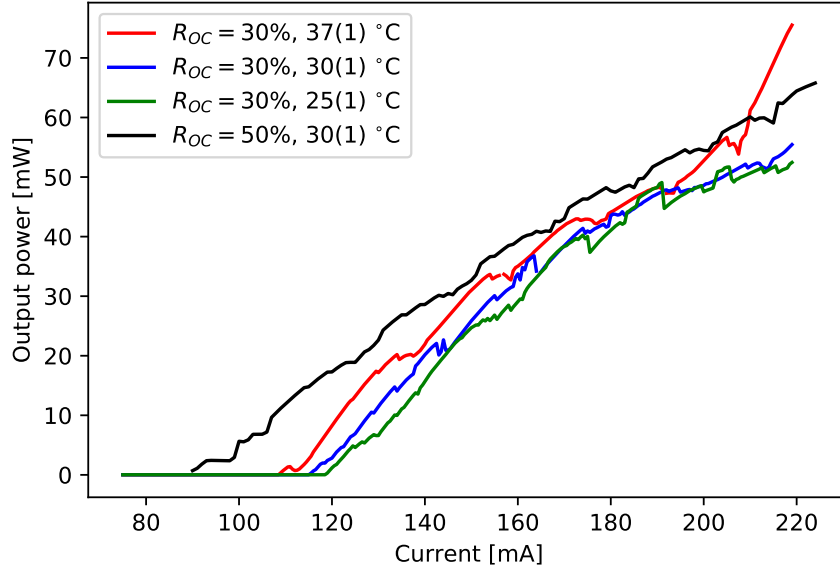
Figure 4.2: *Output power directly after the bare laser for three different temperatures using an outcoupler of 28% and using an outcoupler of 50%. This figure is a cross-section of figure 3.7 **b**) and **c**).*

for determining the PDH discriminator slope k_0. Using the PDH discriminator from figure C.1 **a**) we are able to determine the frequency deviation shown by the error signal. From the in-loop error signal in C.1 **b**), we find a root mean square deviation of 4.11 kHz over a measurement time of 1 ms. However, as noted in section 3.5.3, this method might be inaccurate.
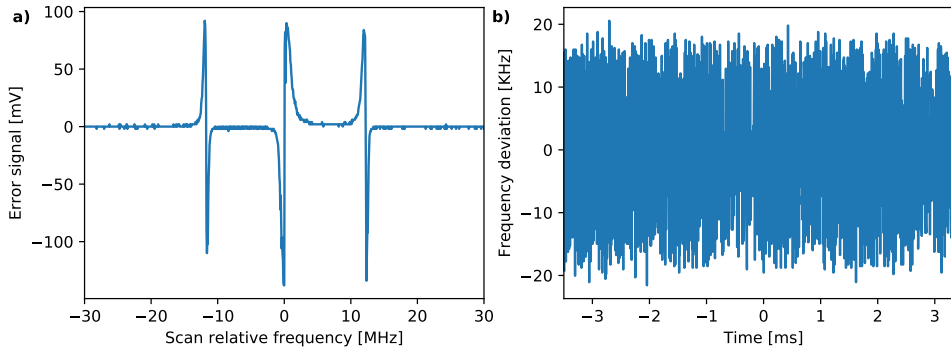

Figure 4.3: **a**) *Scannning PDH error signal over the resonance and **b**) in-loop error signal of the 810A laser using a 50 % outcoupler.*

4.1.2.1 Transfer cavity lock

The transfer cavity is not a stable cavity, as thermal and acoustic noise affect the length and thus the transmission window of the cavity. The transfer cavity is therefore locked to a laser that has a stable

frequency. The lock of the tra nsfer cavity interchanges the role of ECDL and reference cavity encountered in section 3.3.3: the transfer cavity is locked to a 770 nm ECDL (close to the Potassium's lowest D1 line), that is in its turn locked to a Ultra-Low Expansion glass (ULE) cavity according to the scheme of figure 3.3. A piezo altering the length of the cavity suffices to counteract the relatively slow (compared to a laser's noise originating from e.g. injection current noise) thermal and acoustic noise. If we would not stabilize the length of the transfer cavity, thermal drifts, acoustic noise and pressure would drift the 810 nm ECDL's frequency over GHz per day and MHz over experimental timescales.

4.1.2.2   Incommensurability of wavelengths and reference cavities

However, as the two wavelengths coupled to the transfer cavity are different and the free spectral range (FSR) is different for the ULE cavity ($FSR_{\mathrm{ULE}} = 1.5\mathrm{GHz}$) than for the transfer cavity (FSR_{TC}), relocking after the lock has been lost is slightly tedious.

To be able to keep the 810 nm laser on the same wavelength every time the ECDL has to be relocked, the transfer cavity has to be locked to the same transmission peak every time. To understand the effect of a changed transfer cavity lock on the 810 nm laser, we consider locking to an adjacent peak of the transfer cavity. Initially, n wavelengths of the 770 nm laser are supported and m wavelengths of the 810 nm laser are supported in cavity of length L_{TC}. If we now lock the transfer cavity to the 770's $(n+1)^{th}$ peak we slightly (by exactly λ_{770}) increase the cavity's length L_{TC}. When we then lock the 810 nm laser at its closest $(m+1^{th})$ peak to the transfer cavity of changed length, we have shifted our 810 nm laser's wavelength with approximately $(810 - 770)/m$ nm, which for our cavity corresponds to approximately 115 MHz.

Similarly, locking the 770 nm laser to l modes further on of the ULE cavity (spaced by $l \cdot FSR_{\mathrm{ULE}}$ in frequency) requires a shift in the large sideband frequency to have a transfer cavity peak at the same frequency for the 810 nm laser. This shift is given by:

$$\Delta f = -\min_{n}((l \cdot FSR_{\mathrm{ULE}}) \mod (n \cdot FSR_{\mathrm{TC}})) \tag{4.1}$$

If $\Delta f > FSR_{\mathrm{TC}}/2$ shifting with $\Delta f - FSR_{\mathrm{TC}}$ is a smaller shift. Nevertheless, if the new sideband frequency $f' = f + \Delta f < 0$ or $f' = f + \Delta f > FSR_{\mathrm{TC}}/2$ it is necessary to lock to a different sideband. This is relevant to our experiment, as the 770 nm laser coupled to the transfer cavity is simultaneously used for Raman Sideband Cooling.

4.1.3   SHG cavity

As single-mode laser diodes at 405 nm have very low output power, we obtain the blue light by frequency doubling of the 810 nm ECDL described previously. Because non-linear crystals require relatively high power to efficiently generate the first harmonic, an enhancement cavity is required. A so-called unidirectional bow-tie cavity has been constructed in a previous thesis [60].

4.1.3.1   Theory

The polarization $\tilde{P}(t)$ of a material induced by an electric field $E(t)$ of fundamental frequency ω can be expressed as a power series of up to n^{th} order effects [95]:

$$\tilde{P}(t) = \epsilon_0 \left[\chi^{(1)} \tilde{E}(t) + \chi^{(2)} \tilde{E}^2(t) + h.o.t. \right] \tag{4.2}$$

Where $\chi^{(2)}$ is the second order nonlinear optical susceptibility. Applying an oscillating electric field $\tilde{E} = Ee^{-i\omega t} + c.c.$ with frequency ω induces a secondary polarization $\tilde{P}^2(t)$ when $\chi^{(2)} \neq 0$:

$$\tilde{P}^2(t) = 2\epsilon_0 \chi^{(2)} EE^* + \left(\epsilon_0 \chi^{(2)} E^2 e^{-i(2\omega)t} + c.c. \right) \tag{4.3}$$

where the first term is a constant electric field and the second is a field with double the original frequency 2ω that scales linearly to the nonlinear susceptibility $\chi^{(2)}$ and quadratically to the initial field. This process is named Second Harmonic Generation (SHG).

For SHG to occur efficiently, we should ensure that the 2ω frequency field generated throughout the crystal has the same phase at the end of the crystal. Various methods of so-called phase matching exist, but we only present the relevant in our case: type 1 critical phase matching [96]. If the refractive index of the fundamental and the SHG light is the same ($n_\omega = n_{2\omega}$), the phase acquired over a distance z of at $l = 0$ generated light is half as big as that of the fundamental at z. If the fundamental then at $l = z$ generates SHG, the phase is doubled and it is equal to the phase of the at $l = 0$ generated SHG light.

To match the refractive indices likewise we use the birefringence, that is, the material's response is polarization-dependent. The fundamental wave's polarization is along the ordinary axis, whereas the SHG light is polarized perpendicular to that. By adjusting the tilt of the crystal cut, we change the proportion of polarization in the extraordinary axis. A drawback of this approach is that propagation along other than the optic axis causes a walk-off of the beam [95]. The material chosen in [60] is Beta Barium Borate (BBO), where the phase matching occurs at an angle of 29° [97]. BBO has a large $\chi^{(2)} = 4$ pm V^{-1}. Moreover, to ensure that the incoming fundamental light is not reflected on the crystal surface, the crystal is cut under a Brewster's angle.

The optical power in the SHG of a single pass through the crystal can be described by the non-linear coefficient κ_{NL} and the incoming fundamental power P_F [96]:

$$P_{SH} = \kappa_{NL} P_F^2 \tag{4.4}$$

The nonlinear coefficient is then given by:

$$\kappa_{NL} = \frac{4\pi^2 L \chi^2}{c\lambda_F^3 n_{SH} n_F \epsilon_0} h\left(\sigma, B, \xi\right) \tag{4.5}$$

Here, L is the length of the crystal, d_{eff}^2 is the nonlinear , χ the aforementioned nonlinear susceptibility, n_F and n_{SH} the refractive indices of the fundamental and second harmonic light and λ_F the wavelength of the fundamental light. $h\left(\sigma, B, \xi\right)$ is the so-called Boyd-Kleinman parameter, depending on the phase mismatch through σ, the walk-off through B, and the focal strength through ξ. Optimizing this parameter is essential in the design of the enhancement cavity. Due to impinging the crystal at a Brewster's angle, the crystal is an astigmatic element and gives an elliptic output. Therefore, the longer the crystal, the more elliptic the beam: the size of the BBO crystal is limited to 10 mm. The focus was found to have an optimal value corresponding to a waist of 23 μm: a more focused beam increases SHG in the middle, but worsens it on the ends of the crystal . Due to concerns about thermal lensing effects, and thus loss of phase matching, this waist was chosen to be 40 μm.

Efficiency $\eta = \frac{P_{SH}}{P_F}$ is a concavely increasing function of input power, as losses in the fundamental due to second harmonic generation increase at higher input power which gives an asymptotically maximum of efficiency. Nevertheless, typical seeding power from a diode laser, such as the one in section 4.1.1, is

too low for substantial SHG and the asymptotic regime is not reached. Therefore, enhancement cavities are used to enhance the field inside the cavity, leading to a higher SHG efficiency.

4.1.3.2   Cavity Design

This section is strongly based on the preparatory work of [60]: details and optimization calculations can be found there. Calculation and construction of an enhancement bow-tie cavity was successfully performed. Bow-tie cavities are regularly used for SHG enhancement, as they are able to deal with the astigmatism and are unidirectional. Although limited by crystal losses and the 6 optical surfaces encountered per roundtrip, it was found that efficiencies can increase with a factor 50 compared to the single-pass case.
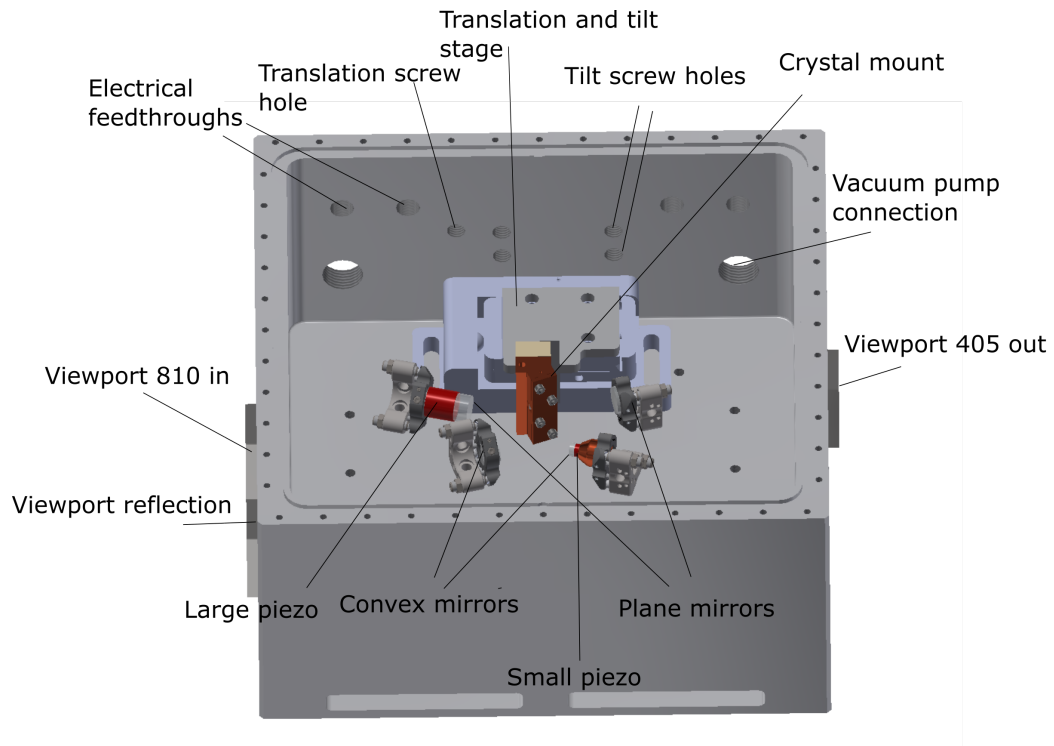

Figure 4.4: *A top-view of the SHG cavity. Through the 810 nm viewport, the fundamental light is coupled into the cavity, where the reflection is leaving the cavity through another viewport. The last mirror of the cavity, which is antireflection coated for the SHG wavelength, leaves the cavity through the 405 nm viewport. The cavity length is controlled by two piezos at two different mirrors. The SHG crystal is connected to a tilt- and translation stage for optimization. Furthermore, a heating element heats the crystal to 80°C, to prevent the surfaces from deteriorating by moisture. Evacuation of the cavity keeps the pressure below 1 mbar to prevent desposition of dirt on the mirrors inside the cavity. The top lid, electrical connectors for heater and piezos, the heating element itself and vacuum connections are not shown.*

The bow-tie cavity design and housing is shown in figure 4.5. All (geometric) parameters are shown in table 4.1. Stability of the cavity for both transversal directions are ensured using a similar approach to section 5.1. Two mirrors are plane, whereas two are convex and form astigmatic elements as the light

Parameter	Value
Crystal length L	10 mm
Calculated coefficient κ_{NL}	$4.9 \cdot 10^{-5}$ W^{-1}
Measured coefficient κ_{NL}	$3 \cdot 10^{-5}$ W^{-1}
Operating Temperature	82°C
Reflectivity incoupling mirror	98.8%
Reflectivity other mirrors	99.95%
Mirror curvature $\mathcal{R}$	50 mm
Crystal waist horizontal	41.9 µm
Crystal waist vertical	64.3 µm
Second waist horizontal	123.7 µm
Second waist horizontal	118.5 µm
Crystal side length	56.88 mm
Second side length	147.8 mm
Full opening angle ϕ	30.01°

Table 4.1: *Parameters of the SHG from 810 nm to 405 nm.*

impinges those at a non-zero opening angle. By choosing the curvatures and opening angles of those two mirrors appropriately, the waists in both directions is similar. Three mirrors have a high-reflective coating of 99.95% for $\lambda_F = 810nm$, whereas the incoupling mirror's reflectivity is chosen to be 98.80% to optimize impedance matching: the back-transmittance from the cavity through the first mirror should match the reflection with a 180° phase shift. To consider the attainable SHG power, we can replace P_F in equation 4.5 by P_{circ}, the circulating power in the cavity. It was calculated that at an incoupling of 800 mW, which is reasonable considering the result of section 4.1.1, the maximal SHG power is 300 mW.

4.1.3.3   Characterisation

Previously the conversion efficiency didn't exceed a few percent. The setup was rebuild to be able to couple in at the height of the housing of the cavity (90 mm) instead of the height of our optics mounts (35 mm), to ease incoupling. The 810 nm light was coupled in at the center of the mirrors using an IR viewer. No increase in conversion efficiency was observed and it was decided to inspect the crystal. After mounting the crystal back and heating it to 80 degrees, it broke and was replaced by a new, identical crystal. In order to test whether the crystal functioned appropriately, the first mirror was temporarily removed and the tilts and lateral position of the crystal were tuned to optimize the single pass efficiency of the SHG. By removing the incoupling mirror of the cavity and focusing into the crystal, we were able to achieve a waist of approximately 35 micrometer. In order to match the incoming beam with the mode of the bow-tie cavity, we employ a concave-convex order of lenses on lateral translation stages to weakly focus the beam to match the waist in the cavity. These elements are shown in figure 4.5.

As the incoupled waist is similar to the calculated size of the Gaussian cavity mode, we are able to estimate the non-linear coefficient using the incoming power in the infrared and the outgoing power in the blue. For a single roundtrip, $P_C = P_F$, and we estimate κ_{NL} to be $3 \cdot 10^{-5} W^{-1}$ in equation 4.4, which is slightly smaller than calculated, which can be attributed to a non-optimal waist.
To realize the cavity enhancement, we return the first mirror and overlap the second roundtrip as good as possible with the first one. Subsequently, we need to adjust the horizontal incoupling of the cavity as the
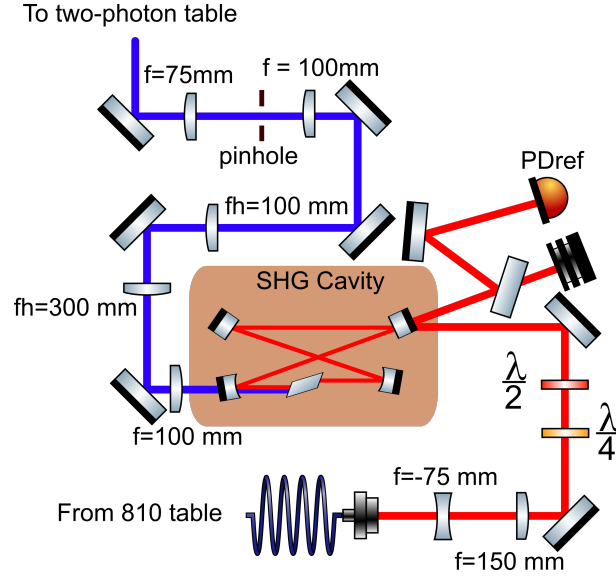
Figure 4.5: *Setup of 405 nm SHG cavity, seeded by the 810 nm laser from figure 4.1. fh - horizontal cylindrical lens with focal length f h, f - normal lens with focal length f. The setup continues in figure 6.11.*

inclusion of the first mirror displaced the beam. Cavity re-alignment and crystal tilt have to be optimized iteratively, as the BBO crystal has a small acceptance angle for correct phase matching. Realigning the crystal displaces the beam and alters the astigmatism in the cavity, require cavity realignment. Conversely, cavity realignment worsens the phase matching condition of the crystal. After slight modifications to the other mirrors, we obtain an incoupling for around 90 % in the fundamental mode of the cavity. However, output power remains slightly below calculated. We are able to achieve 120 mW of 405 nm light right after the cavity when 700 mW is coupled into the cavity. This corresponds to an SHG efficiency of 17%. It is substantially lower than the 37% calculated theoretically for 800 mW incoupling [60]. One explanation might be that the calculated nonlinear coefficient κ_{NL} is higher than the measured coefficient. Although the measured coefficient might not be accurate because we used an external movable lens, it might indicate that the crystal efficiency is simply lower than calculated. Furthermore, the first mirror reflectivity might have been suboptimal (it was chosen to have slight under- rather than overcoupling of the cavity) [60]. Ultimately, the incoupled power is around 700 mW, partially explaining the lower efficiency. A part of the reflection signal is sampled out for the PDH lock, and the transmission of the second harmonic light is beam shaped and used as a $4S_{1/2} \rightarrow 5P_J$ excitation laser.

The lock of the SHG cavity to the 810 nm light is similar to the standard PDH lock of section 3.3.3, but the fast modulation is performed by the small piezo and the slow modulation by a big piezo. The sidebands are provided by an EOM with a resonance at 53 MHz on the 810 nm laser table (see figure 4.1). As the FWHM of the cavity is a few MHz, we need to use sufficiently big sidebands to satisfy the condition that the signal of the sidebands is fully reflected. Figure 4.6 shows the PDH error signal and the cavity incoupling through the DC signal of the reflection photodiode

However, although the transmitted 810 nm light shows a neat TEM$_{00}$ mode, the transmitted 405 nm light does not. As expected, the beam is astigmatic, but the beam shows a region of lower intensity in the middle of unknown origin. Therefore, we require several stages of beamshaping. A convex lens right after the
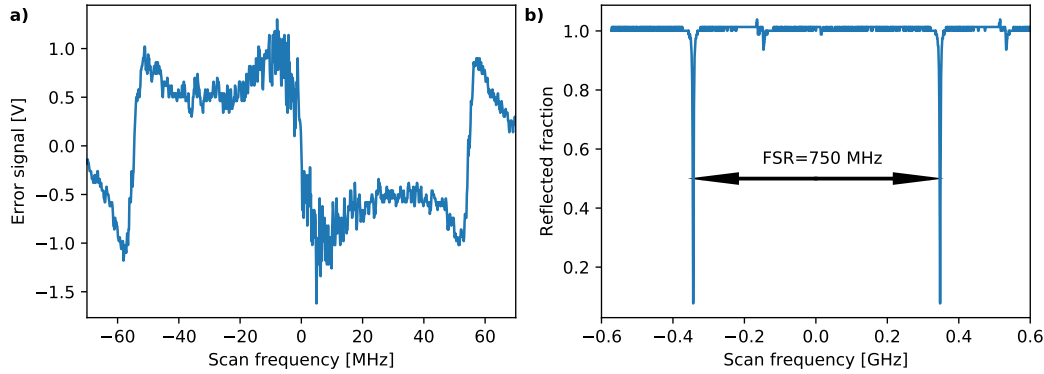
Figure 4.6: *a) PDH signal of the SHG cavity lock to the 810 nm laser. It appear noisy as the transfer cavity of section 4.1.2.1 is not locked to the ULE cavity. b) Cavity incoupling of the 810 nm laser: an incoupling of 93% is achieved. Next to the Gaussian mode, another mode is slighty coupled. The free spectral range (FSR) of the cavity is about 750 MHz.*

cavity collimates the vertical directon. A telescope of two horizontal cylindrical lenses ($f = 300, 100$ mm) is used to also collimate the other direction and equate the waists of the two directions. Ultimately, as the beam is not Gaussian, it is focused through a pinhole to make the intensity profile more homogeneous and slightly smaller in size by a convex-convex ($f = 100, 75$ mm) telescope. After beamshaping with a pinhole of 50 µm, 60 mW of blue-violet light is obtained. The beam is further used in the setup described in figure 6.11.

4.2 980 nm setup

4.2.1 980 nm ECDL

The current setup for the 980 nm light is shown in figure 4.7: it uses the 980A laser discussed in section 3.5. Around the wavelength calculated for the $5P_{1/2} \rightarrow 35S_{1/2}$ transition that we want to address, we obtained a MHFTR of 7 GHz. The laser its output is characterised in secton 3.5.2 and has a few kHz instaneous linewidth. The 980 nm laser's output is slightly astigmatic and rather big when collimated with the last lens. A normal 2:1 convex-concave telescope sufficed to reduce the beam size such that the TA can be properly seeded. 60dB of backreflection attenuation was provided by an optical isolator (IOT-5-980-VLP). Around 2 mW goes to the branch with wavemeter and ULE. We require some filters to ensure only 40 µW is coupled through the fiber EOM (EOSPACE PM-0S5-10-PFA-PFA-970/1005) to the ULE. The setup in the ULE has been kept unchanged (see [60]) and more than 90% incoupling is achieved. The collimator used to couple to the ULE is a SuK 60FC-F-4-M12-08 and to the wavemeter a Thorlabs F230-APC-980. A second 30 dB optical isolator (IO5-980-VLP) had to be placed in the branch to the TA to prevent emission from the TA to affect the laser operating and to reach the ULE. After the TA we obtain 2.1 W of light. Similar to the 810 nm setup, we have to collimate the horizontal direction of the TA emission by a cylindrical lens ($f = -50$ mm) and decrease the beam size with a 2:1 telescope ($f = 100, -50$ mm). We use the interference filter to filter out the spontaneous emission background of the TA.

Additionally, an AOM (Gooch & Housego 3110-197) is placed in the setup to enable fast switching and chopping of excitation pulses. To increase the speed of pulsing the 980 beam and to match the beam size

to the fiber collimator (SuK 60FC-F-4-M12-08), we focus the beam through the AOM with a telescope ($f = 150, -175$ mm). The rise time of pulsing the AOM was around 38 ns when focusing, and 60 ns with a collimated beam with a waist of 500 μm. The AOM efficiency is 76% is the in the first order with a collimated beam, whereas it is 60% for the focused beam. When focusing, the achieved fiber coupling is 450 mW.
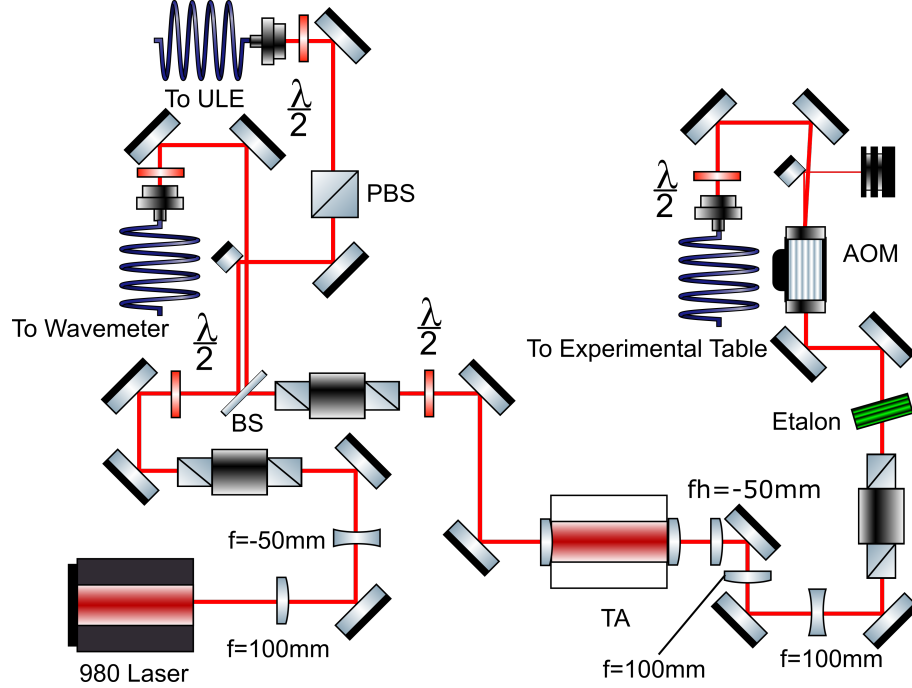

Figure 4.7: *The setup from the 980 ECDL up to the fiber coupling to the experimental table. PBS - Polarizing Beam Splitter, BS - non-polarizing beam splitter, TA - Tapered Amplifier, fh - horizontal cylindrical lens with focal length fh, f - normal lens with focal length f, AOM - Acousto-Optical Modulator, ULE - Ultra-Low Expansion cavity.*

4.2.2 Characterization

Figure 4.8 shows the output power as a function of injection current into the laser diode. We observe minimal power differences between various modes of the laser. This implies a rather flat gain curve and neat single-mode operation. This measurement is a cross-section of figure 3.7 at the operating temperature $T = 27(1)$°C. Nevertheless, this figure is only valid when increasing current from low to high current as the mode behaviour is hysteretic. Therefore, this figure is only valid when increasing current from low to high current. It can be seen that most mode hops (where the output power changes, see section 3.5) barely affect the output power and that the slope efficiency of the laser is similar for all currents.

Figure 4.9 shows the PDH lock to the ULE cavity. As touched upon in section 3.3, EOM crystals may exhibit Residual Amplitude Noise because of thermal fluctuations. In order to prevent this, the EOM mount was connected to the optical table, that has a large heat capacity. Furthermore, the EOM used showed larger insertion loss and lower efficiency at higher frequencies than the EOM used in section 4.1.1. Therefore, a higher power amplifier (RFBay ENA-210T) was used to provide an RF power of 24 dBm, whereas the old amplifier was limited to 20 dBm (Mini Circuits ZFL1000H+). A step-by-step
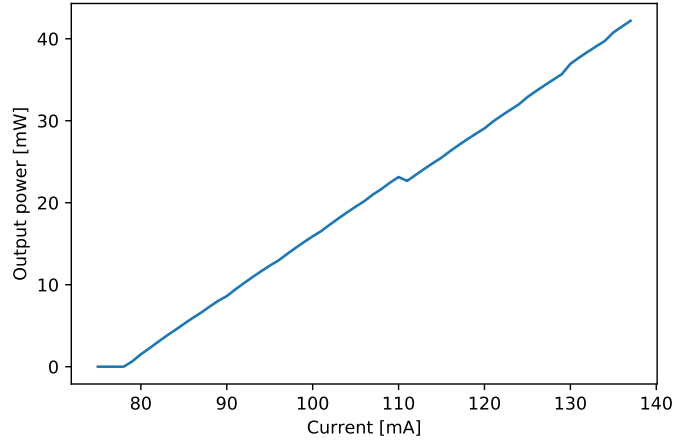
Figure 4.8: *Output power just after the bare laser. This figure is a cross-section of figure 3.7 **a**).*

overview of the locking electronics can be found in figure C.1. Over a span of 1 ms we find a root mean square deviation of 3.26 kHz. However, as noted in section 3.5.3, this method might be inaccurate.
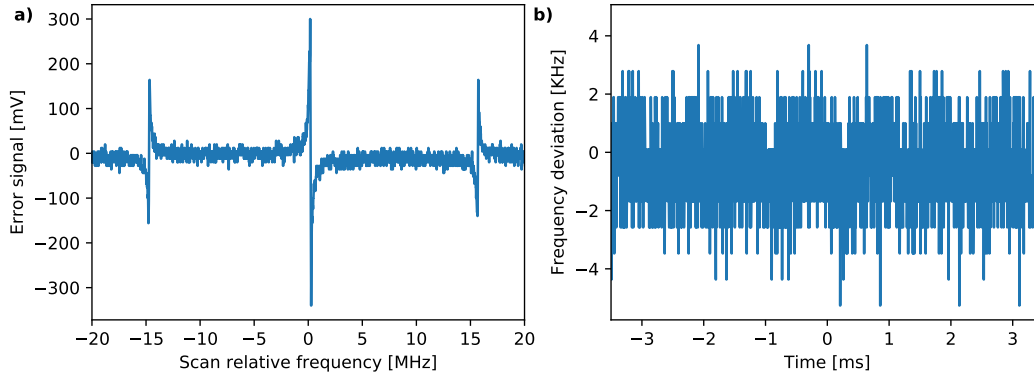

Figure 4.9: ***a**) Scannning PDH error signal over the resonance and **b**) in-loop error signal of the 980A ECDL.*

Concluding remarks

With the laser systems presented in this chapter we are able to obtain $\Omega_{405} = 2\pi \cdot 10$ MHz (60 mW) and $\Omega_{980} = 2\pi \cdot 2.7$ MHz (450 mW) with a TEM$_{00}$ beam of 1 mm in diameter to the $35S_{1/2}$ state. The SHG cavity achieves an efficiency of 17% after extensive optimization, but is still below the calculated efficiency. By analyzing the PDH error signal of the locked ECDLS, we obtain an estimated root-mean-square linewidth of 4.11 (810 nm) and 3.26 kHz (980 nm). As previously considered, one of the limiting factors of coherent excitation is the laser phase noise. The upcoming chapter poses a possibile improvement to that: filtering the laser light through a high-finesse optical cavity.

Chapter 5

Cavity for phase noise filtering

As identified in section 2.3, one of the limiting factors to Rydberg experiments through decoherence is the laser phase noise [47]. We consider the option of a filter cavity as a way to enhancing future experimental coherences, to be built into the setup shown in figure 4.1 between the ECDL and the TA of the previous chapter. First of all, 5.1 discusses the basics of linear cavities to be designed, whereas section 5.2 displays the choices that have been made and section 5.3 characterizes the incoupling achieved in a trial setup. Ultimately, in section 5.4 we use the filter cavity to actually measure the phase noise of Fourier frequencies above the transmission width of the constructed cavity.

5.1 Linear cavities

A cavity is stable if its mode maps onto itself after an additional roundtrip. One can describe the operation of an optical element on a beam by a 2-dimensional unit determinant ray transfer matrix, coined ABCD-matrix after its four elements [98]. As the stability condition requires that after n roundtrips the elements of $\mathbf{M^n}$ should not diverge as a function of n. This is satisfied when the trace of the single roundtrip ABCD matrix obeys the following:

$$-1 < \frac{A+D}{2} < 1 \tag{5.1}$$

In a linear cavity the transfer matrix $\mathbf{M}$ is given by the product of the ABCD matrices of a plane lens, a propagation through a medium with length l, concave lens, and a propagation through a medium with length l, sequentially:

$$\mathbf{M} = \begin{pmatrix} 1 & 0 \\ -2/\mathcal{R}_1 & 1 \end{pmatrix} \begin{pmatrix} 1 & l \\ 0 & 1 \end{pmatrix} \begin{pmatrix} 1 & 0 \\ -2/\mathcal{R}_2 & 1 \end{pmatrix} \begin{pmatrix} 1 & l \\ 0 & 1 \end{pmatrix} \tag{5.2}$$

Where l is the length of the cavity and $\mathcal{R}_{1,2}$ are the radii of curvature of the two mirrors used. Then, the stability criterion becomes:

$$0 < \left(1 - \frac{l}{\mathcal{R}_1}\right)\left(1 - \frac{l}{\mathcal{R}_2}\right) = g_1 g_2 < 1 \tag{5.3}$$

This condition is graphically shown in figure 5.1. The two dots consider two stable hemispherical cavities attainable in section 5.2.
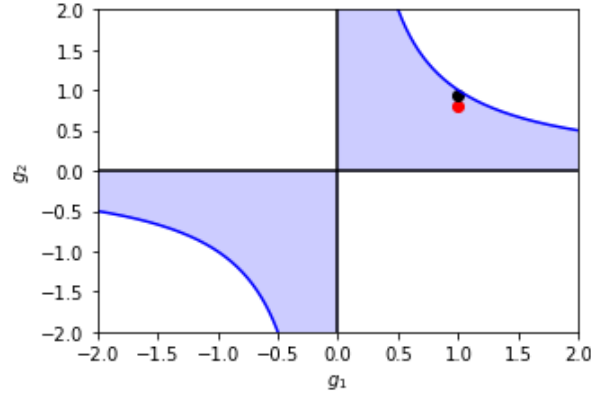
44

Figure 5.1: *Stability map of linear cavities as a function of g_1 and g_2. Shaded areas are stable configurations. The red dot refers to the cavity with a mirror with radius of curvature $\mathcal{R}_1 = 500$ mm used in section 5.2 and the black dot refers to the other mirror available with $\mathcal{R}_1 = 2000$ mm.*

Although we have ensured the stability of the cavity, we have to ensure the fundamental mode (TEM$_{00}$) of the cavity to match the size of the incoupling beam. We can calculate the size of the fundamental mode of the cavity for a hemispherical cavity ($\mathcal{R}_1 > 0$, $\mathcal{R}_2 = -\infty$) with length l by imposing that the radius of curvature should equate the radius of curvature at both of the mirrors. The radius of curvature of a beam is given by $\mathcal{R}(z) = z + z_0^2/z^2$, where z is the length along the beam and $z_0 = \pi\omega_0^2/\lambda$ is the Rayleigh length, defined as the half length along which the beam waist remains a factor of $\sqrt{2}$ within the minimum waist ω_0. Equating to the radius of curvature to that of mirror 1 ($\mathcal{R}(z) = \mathcal{R}_1$) and using $z = l$ we obtain the following (minimum) waist at mirror 2

$$\omega_0 = \sqrt{\frac{\lambda}{\pi}\sqrt{l(\mathcal{R}_1 - l)}} \tag{5.4}$$

and the waist at distance z in the cavity:

$$\omega(z) = \omega_0\sqrt{1 + \left(\frac{z\lambda}{\pi\omega^2}\right)^2} \tag{5.5}$$

5.1.1 Filtering and transmission

As discussed in section 3.2, phase noise around the Rabi frequency is the most detrimental to Rydberg experiments. A linear cavity with sufficiently low FWHM can filter orders of magnitude at attainable Rabi frequencies. In the frequency domain, a filter cavity acts as a low pass filter for laser phase noise: slowly changing phase fluctuations, slower than the cavity photon storage time, are transmitted, whereas fluctuations faster than that average out. In the frequency picture this is equivalent to a narrow band pass filter around the resonance. The finesse of a cavity $\mathcal{F}$ is given by:

$$\mathcal{F} = \frac{\pi\left(R_1 R_2\right)^{1/4}}{1 - \left(R_1 R_2\right)^{1/2}} \tag{5.6}$$

Where $R_{1,2}$ is the reflectivity of the first and second mirror, respectively. The mode spacing, or Free Spectral Range (FSR) is given by:

$$FSR = \frac{c}{2L} \tag{5.7}$$

Where L is the length of the cavity and c the speed of light. The previous two equations combinedly determine the transmission linewidth of the cavity:

$$\nu_{\text{FWHM}} = \frac{FSR}{\mathcal{F}} \tag{5.8}$$

In order to consider the transmission of the filter cavity, we need to calculate how large the transmission is with respect to the absorption and scattering losses in the coating. The circulating field strength E_{circ} as a multiple of E_{in} can be calculated in terms of the coefficients of reflectivity (r) and transmission (t):

$$\frac{E_{circ}}{E_{in}} = \frac{t_1}{1 - \bar{g}_{rt}} \tag{5.9}$$

Here we can tune the exponential term in $\bar{g}_{rt} = r_1 r_2 e^{i2\pi 4d/\lambda}$ to unity by tuning the cavity length to a multiple of wavelength. Similarly, we can define the relative transmission through the cavity:

$$\frac{E_t}{E_{in}} = -\frac{t_1 t_2 e^{i2\pi d/\lambda}}{1 - \bar{g}_{rt}} \tag{5.10}$$

Where losses L of a single reflection event enter into $t^2 = T = 1 - R - L$. Impedance matching of the cavity is optimal when the reflected signal is zero. This occurs when reflection of the first mirror equals all the losses including tranmission at the second mirror inside the cavity. Ideally this is only the transmission of the second mirror. The relative reflection is given by:

$$\frac{E_r}{E_{in}} = r_1 - \frac{t_1^2}{r_1} \frac{\bar{g}_{rt}}{1 - \bar{g}_{rt}} \tag{5.11}$$

Again setting $d = n\lambda$ and considering lossless mirrors, this condition is fulfilled if $R_1 = R_2$. To calculate the power in all of the previous equations we take $I = |E|^2$.

5.2 Cavity design

5.2.1 Mechanical

Within the group, linear cavities were designed before, and we adopted a slightly modified version of this design. Figure 5.2 shows a top view of the spacer which holds the mirrors and of the whole evacuated cavity design. For a detailed description of the construction and parts used, we refer the reader to [99].

Evacuation and isolation of the cavity reduces air fluctuations and the possiblity of dirt on the mirrors. With an appropriate pump the cavity has been evacuated to a pressure below 1 mbar. Underneath the $L = 100$ mm long spacer two small spacers provide insulation and prevent outgassing over time. The spacer is made out of brass, which has a non-negligible thermal expansion coefficient. Furthermore, as we do not have temperature control of the cavity, the cavity is not as stable as e.g. the ULE-cavity used in chapter 4. Nevertheless, if the laser frequency is stable, the piezo is able to stabilize the cavity to a coupled laser to counteract slow temperature drifts and fast acoustic deviations. The mirrors that form the cavity are clamped between a viton ring and a ring that can be inserted in the large spacer. On one side a piezo is connected between the ring and mirror to tune the length of the cavity.
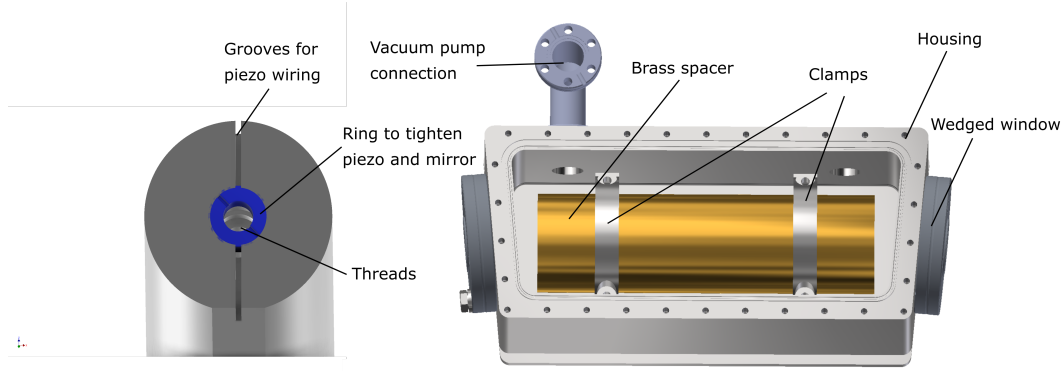
Figure 5.2: *Design of the filter cavity. Left picture shows the end of the brass spacer that contains the concave mirror and piezo. In blue the spacer that tightens the piezo and the mirror is shown. On the side that is not shown here a similar construction appears: nevertheless, no piezo is necessary there, so the grooves are absent. On the right the whole outer housing is shown.*

5.2.2 Optical

The higher mirror reflectivities, the lower the cavity transmission width and the lower the transmission (see section 5.1.1). However, as losses are finite, transmission decreases rapidly if the transmission rate approaches the inherent losses of the mirrors. To quantify this trade-off, we show the result of equation 5.8 and 5.10 in figure 5.3. Although filtering phase noise with a high-finesse cavity is effective, losses limit
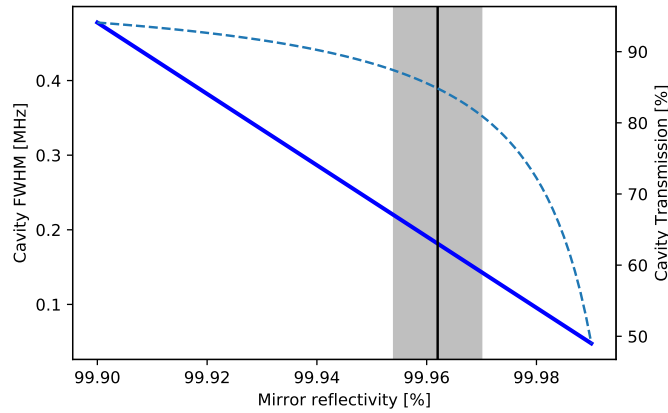

Figure 5.3: *Theoretical FWHM of a filter cavity as a function of mirror reflectivity, where $R_1 = R_2$ and it is assumed that scattering and absorbtion losses are 30 ppm. The left axis shows the FWHM of the cavity its transmission window (blue line), whereas the right (blue dashed line) shows the power transmission through the cavity using 5.10. The vertical line shows the middle reflectivity chosen whereas the shaded area shows the minimal and maximal value as specified by the producer.*

the power transmitted, and thus available optical power to seed an optical amplifier or to excite atoms. The horizontal line in figure 5.3 shows the chosen mirror reflectivity, where the shaded area corresponds to the uncertainty provided by the producer. As we are able to obtain 30 mW before the TA in figure 4.7, we need at least 80 % of transmission to sufficiently seed the TA with a bit more than 20 mW. Therefore,

Mirror $\mathcal{R}$	ω_0	$\omega(z = l)$
$\mathcal{R} = 500$ mm	250 μm	279 μm
$\mathcal{R} = 2000$ mm	369 μm	378 μm

Table 5.1: *Cavity waists at both ends of the cavity for two different concave mirror curvatures.*

the chosen reflectivity is 99.962%. Error bounds using the uncertainty in mirror reflectivity have been reported: the minimum theoretical transmission is 81%.

Figure 5.4 shows the filtering of the phase noise as a function of a phase noise Fourier frequency using the suggested mirror reflectivity. As the servo bandwidth resonance of the 980B ECDL is around 300 MHz and that of the 980A ECDL somewhat higher, we are able to filter at least an order of magnitude at those Fourier frequencies. Nevertheless, obtaining at a servo resonance at 1 MHz already allows for two orders of magnitude filtering.

The other variables are the mirror curvatures, which should give a stable cavity as shown in section
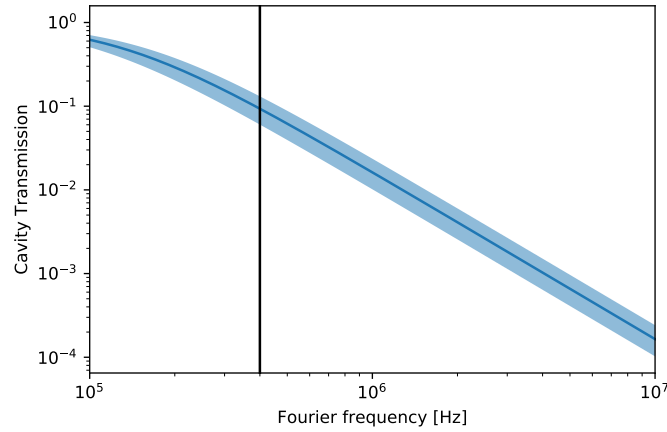

Figure 5.4: *Theoretical filtering of a filter cavity as a function of mirror reflectivity, where $R_1 = R_2$ and it is assumed that scattering and absorption losses in the mirror coatings are 30 ppm. The left axis shows the FWHM of the cavity its transmission window (blue line), whereas the right (blue dashed line) shows the transmission through the cavity. The vertical line shows the end of the servo bandwidth of the 980B laser.*

5.1. We choose a hemisherical cavity with a plane mirror and concave mirror curvatures $\mathcal{R} = -500$ and $\mathcal{R} = -2000$ mm. The waists of the TEM$_{00}$-mode at mirror 1 and 2, calculated by equations 5.4 and 5.5, are given by table 5.1. Those waists are slightly below the size of the collimated beam sizes of Chapter 4. A batch of mirrors, with the High Reflection (HR) coating discussed on one and Anti-Reflection (AR) coating on the other side was ordered from LaserOptik which specifies scattering and absorption losses of 30 ppm in an Ion Beam Sputtered (IBS) coating run. The mirrors coatings are similar for both 980 and 1150nm (for the one-photon setup) to be able to also build a filter cavity for the 1150 nm laser at a later stage. The coatings have a reported reflectivity of 99.962(8)%, leading to a finesse $\mathcal{F}$ between 6827 and 10470 and a most likely value of 8265. As a reference, another experiment employed a filter cavity with $\mathcal{F} = 3000$ [47].

5.3 Characterization

To characterize the cavity we couple in light from the homebuilt 980B ECDL according to the setup shown in figure 5.8. In order to characterize the transmission of the laser through the cavity the laser is locked to the cavity (although in the experiment it would be the other way around).

5.3.1 Laser lock

The lock employed is again along the lines of section 3.3. We obtain a root-mean-square linewidth of 15.8 kHz over a measurement time of 1 ms, which is larger than the estimate of the 980A ECDL in section 4.2, which is locked to a ULE cavity.
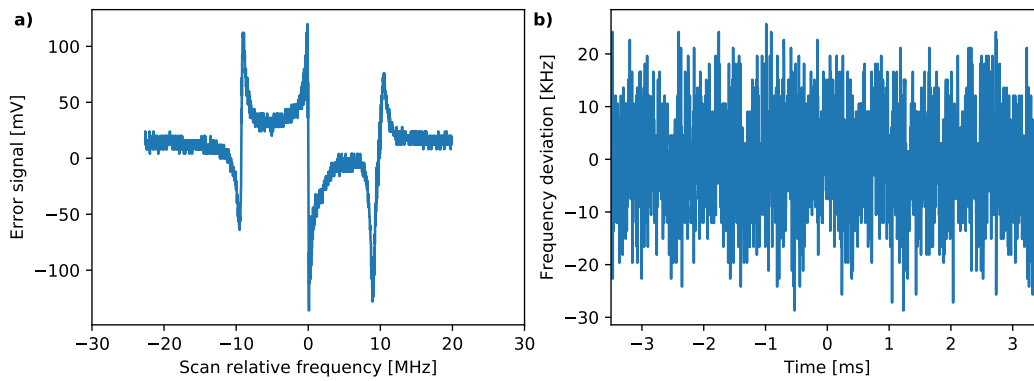

Figure 5.5: *a) Scannning PDH error signal over the resonance and **b**) in-loop error signal of the 980B ECDL.*

Figure 5.6 shows a zoom of the TEM_{00} mode through the cavity, which shows a 75% incoupling efficiency.
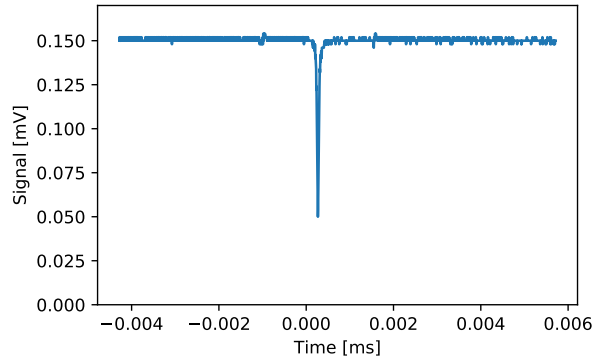

Figure 5.6: *Reflection of the 980B ECDL coupled to the filter cavity. The ECDL frequency is swept over the cavity resonance by sweeping the piezo voltage of the ECDL. Only the TEM_{00} mode and the 9 MHz sidebands are visible: all other cavity modes are coupled less than the noise level of the photodetector.*

However, we only obtain a transmission of at various input powers of 41%. Corrected for the limited incoupling of 75%, this amounts to a coating loss of 224 ppm (using equation 5.10). This is almost an order of magnitude more than the specified coating loss. Either the coating loss is higher than 30 ppm

or during the construction process dirt landed on the HR coated side of the mirrors. This also implies that the filter cavity is not useful for seeding the TA in the setup for the 980 nm laser in section 4.2. The high losses are also problematic for another reason: heating in the cavity may render the lock unstable. Therefore, an injection lock with the use of another slave laser might be necessary to seed the TA (see e.g. [100]).

5.3.2 Finesse

Figure 5.7 shows the measurement of transmission of the light after deliberately unlocking the cavity from the laser field. As the cavity still stores light when it is coupled by the laser anymore, every roundtrip time of $\tau = 2L/c = 0.67$ ns a fraction $1 - R - L$ is lost. An exponential function is fitted to the decay of transmitted light and provides a reasonable fit to the data. This method is sensitive to a background as the new lockpoint or unstable laser might have some transmission. For that reason, the first microsecond of data is not shown and not fitted to. However, in figure 5.7 the background level at 10 µs is even lower than the fit.
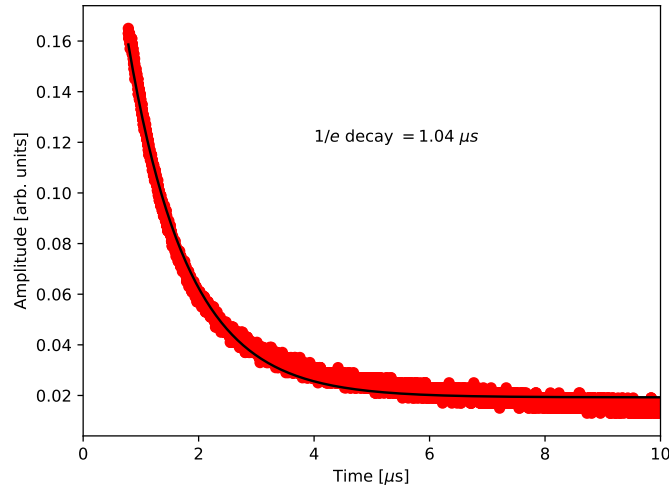

Figure 5.7: *Ringdown measurement of filter cavity using 980 nm laser, with an exponential fit supplied. The transmission photodiode signal through the cavity is shown, just after the cavity lost lock. The red curve showed the data obtained using a photodiode in transmission and the black line provides an exponential fit.*

For the filter cavity we observe a 1/e decay constant of 1.04 µs. This corresponds to a finesse of 9796, which is higher than the aimed finesse, but within the bounds reported in section 5.2.

5.4 Phase noise measurement

The phase noise of lasers can be measured in various ways. By beating two identical lasers or one laser delayed over more than its coherence length allows for determination of phase noise, similar to how it allows to measure the linewidth [84]. Furthermore, using a frequency-discriminating Fabry-Perot cavity weakly locked to the source laser enables measuring combined amplitude and frequency noise [101]. Nevertheless, without a second identical laser or a slow locking system, but with a high finesse cavity, it

is possible to estimate higher frequency phase noise [92].

5.4.1 Filter cavity beat note

5.4.1.1 Setup

An optical beat note between two light fields of frequencies ω_1 and ω_2 yields sum ($\omega_1+\omega_2$) and difference ($\omega_1-\omega_2$) terms. If both optical frequencies are close, the difference term can be detected on a photodiode. As the filter cavity filters high-Fourier frequency phase noise, a beat of the laser's output with its output transmitted through the filter cavity is uncorrelated at high Fourier frequency. This is due to the absence of high Fourier frequency components in the light transmitted through the filter cavity. Therefore, we are able to extract the power spectral density of phase noise at those Fourier frequencies [92]. The amplitude of the beat note below the 1/e width of the cavity ($\Delta f_{FWHM} = 310$ kHz) is lower than the actual noise level, as the both beams are perfectly correlated. By shifting the frequency of one the beams by 105 MHz using an AOM, we are able to perform a measurement of phase noise with a commercially available spectrum analyzer. Figure 5.8 shows the setup used. Note that the laser is locked to the cavity according to section 3.3.3. To prevent interference of the two different polarizations inside the photodiode, the polarization of both beams was turned vertical and overlapped on a non-polarizing cube.
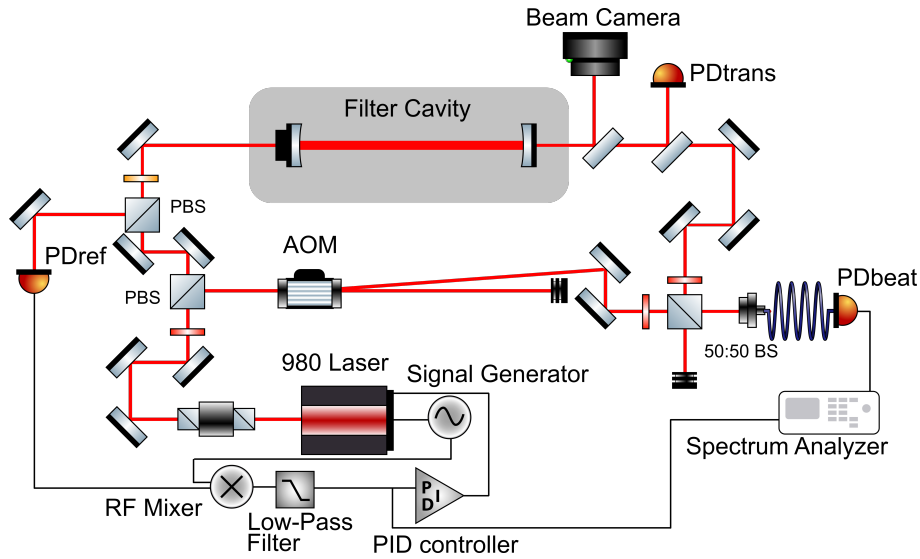

Figure 5.8: *Setup of the filter cavity for characterising and phase noise determination. For the latter, the light is split up by a PBS. One path is sent through the filter cavity and the other path is sent through an AOM. The first order of the AOM (105 MHz) and the cavity transmission are polarization matched and overlapped on a non-polarizing BS. The beat of both lasers is recorded by a fiber-coupled Thorlabs DET025AFC and analysed by a spectrum analyser (Anritsu MS2721b).*

Figure 5.9 shows the one-sided phase noise $\mathcal{L}(f) = S_\phi(f)/2$ of the 980B ECDL as calculated from the beat note (solid blue line) expressed in terms of dB under the carrier power per Hertz. The vertical black line denotes the 1/e width of the cavity: below this cut-off the results are deemed untrustworthy. By integrating the phase noise obtained over frequency from the highest available frequency f_{max} up to the frequency f, we obtain the integrated phase noise $\phi^2_{RMS}(f)$ (blue dashed line). The integrated phase noise is a measure used to describe how much power is in the noise pedestals compared to the carrier of

the lineshape [92].

To consider the phase noise with respect to other possible noise sources onto the detection signal we consider a dark measurement of the dark photodiode (red) and the AOM driver output (purple). Their backgrounds are negligible compared to the beat signal. Although the signal below the cut-off is not deemed trustworthy, we can still resolve the servo bump at 300 kHz. We observe that phase noise decreases rapidly between 300 kHz and 2 MHz. It is also observed that the beat signal slopes downward towards low frequencies and not up as we expect from $1/f$-noise at low frequencies: this is the result of beating two perfectly correlated lasers.
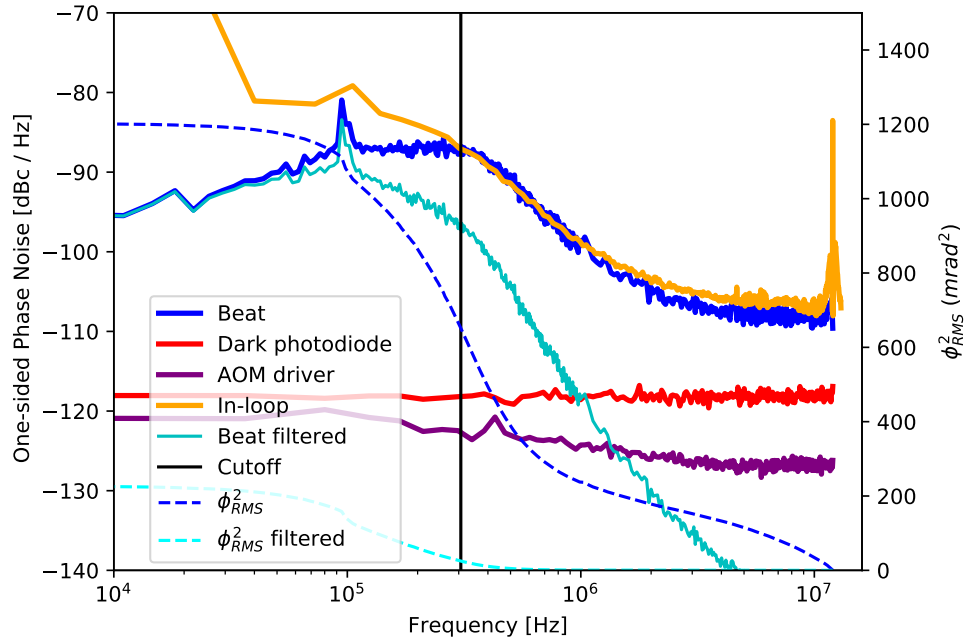

Figure 5.9: *Phase noise of the beat between an AOM-shifted 980B ECDL and its transmission through the filter cavity (blue), the dark biased photodiode (red), the noise of the AOM driver (purple). The phase noise calculated with the in-loop error signal is shown in orange. The dashed blue line shows the integrated phase noise. For all traces the Resolution Bandwidth (RBW) is 300 Hz, except for the blue trace below 2MHz: it is obtained with a RBW of 30 Hz. The beat note is obtained with 500 µW of unfiltered and 100 µW of cavity-filtered light. The vertical black line is the lower cut-off Δf_{FWHM} at which we deem our measurement trustworthy. Theoretical filtering with a cavity of finesse $\mathcal{F} = 9796$ on the blue traces is shown by the cyan traces.*

By integrating the phase noise curve from high to low frequencies we obtain the integrated phase noise ϕ_{RMS}. The power of the laser in the carrier signal can be calculated as $P_{carrier} = \exp\{-\phi_{RMS}^2\}$. Down to 100 kHz, we measure $\phi_{RMS}^2 = 1000$ mrad^2 corresponding to the integrated phase noise $\phi_{RMS} = 33$ mrad. This implies that 0.10% of total power is in the noise pedestals. Furthermore, we can analyse the theoretical filtering of the filter cavity presented. The solid cyan line in figure 5.9 shows the effect on the phase noise: at 1 MHz the phase noise is already lower than the photodiode noise level. The integrated phase noise (dashed cyan line) therefore also shows a large suppression.

5.4.2 In loop error signal

The in-loop error signal of the locked laser contains valuable spectral information, but has some drawbacks (see section 3.5.3). The error signal when the electronics are locking to a cavity resonance corresponds to the frequency difference between the reference and the laser. However, this error signal is a radiofrequency (RF) signal with a power $p(f)$ outputted by the mixer of the PDH signal. To obtain the voltage power spectral density $S^V(f)$ we have to transform the RF power:

$$S^V(f) = Z_0 p(f)/RBW \tag{5.12}$$

Where RBW is the resonance bandwidth used to obtain the trace. The voltage PSD can be converted to a frequency noise by means of the PDH discriminator k:

$$S_{\delta\nu}(f) = \frac{S^V(f)}{k(f)} \tag{5.13}$$

By considering the slope of the PDH signal at the zero crossing, one can convert a measured voltage deviation to a frequency. However, when the frequency reference, in this case the filter cavity, has a transmission window (Δf_{FWHM}) narrower than the frequencies of interest, the slope efficiency $k(f)$ is reduced. This reduction follows from the fact that the fluctuations of the field are faster than the bandwidth of the cavity. The frequency-dependent slope is [74]:

$$k(f) = \frac{k_0}{\sqrt{1 + 4f/\Delta f_{FWHM}}^2} \tag{5.14}$$

By sweeping the laser's piezo at low frequency we obtain the PDH error signal (see section 3.3). The slope at the zero crossing k_0 can be interpreted as the responsivity of the error signal to a deviation in frequency.

Subsequently, using equation 3.8 the corrected integrated phase noise can be calculated:

$$\mathcal{L}(f) = S_\phi/2 = \frac{S_{\delta\nu}(f)}{2f^2} \tag{5.15}$$

The in-loop derived phase noise is shown in figure 5.9 (orange line). We obtained a slope efficiency of $k_0 = 4.2 \cdot 10^{-6}$ V Hz^{-1}. As the PDH sidebands were obtained by modulating the current of the laser at a maximum of 15 MHz, this 15 MHz component is present in the noise: on the right hand side of the plot a peak is visible. At low frequencies, this method might be severely limited: the noise added onto the reference cavity can not be seen on the PDH signal. Furthermore, too large feedback gain leads to too large of suppression below the noise limit: it just suppresses noise from the electronics and reference cavity and not a frequency deviation of the laser. This even adds noise to the laser, but is not observed on the error signal [74].

Concluding remarks

In this chapter, a filter cavity is designed, characterised and employed to measure the phase noise of an ECDL. The phase noise measurement was in good correspondence with a phase noise measurement using the in-loop error signal. As the latter is a less demanding measurement (we need no more elements as for a

locked ECDL), it is a useful way to quantify the phase noise at the relevant frequencies. The constructed cavity has a finesse of 9796, which lies within the range expected from specified mirror reflectivities. Unfortunately the transmission through the cavity was unexpectedly low: only 41% of the incident light was transmitted. The issues with the transmission can be overcome by an injection lock scheme, which filters the light of an ECDL and feeds it to another laser diode, which is then lasing at the injected light's frequency.

Nevertheless, phase noise can be suppressed by almost 2 orders of magnitude at a Fourier frequency of 1 MHz using the cavity constructed. The actual benefit of phase noise filtering depends on the Rabi frequency used (the larger, the more of the relevant phase noise spectrum is filtered, but the lower initial phase noise density) and the extent to which the other limiting factors presented in section 2.3 affect the experiment.

However, it is not that detrimental for the two-photon setup as for the one-photon setup: phase noise increases with frequency doubling as $q\phi_{RMS}$, where q is the generated harmonic. This implies a severe effect on the one-photon setup, which uses two steps of doubling, so $q = 4$. Therefore, phase noise filtering on the one-photon setup is even more important. However, the fiber amplifier used before the filter cavities might not be able to handle a loss of seed light due to an unlock of the filter cavity. It is verified that state of the art experiments of one-photon Rydberg excitation are limited by phase noise [48].

Chapter 6

Rydberg excitation and spectroscopy

In order to create Rydberg atoms in Potassium by a two-photon transition, we need to excite the atoms with the two-step process described in chapter 2. Although usual cold atom experiments operate below $100 \, \mu$K typical for Magneto-Optical Traps, it is useful to perform a crude spectroscopy of the intermediate and Rydberg levels in a heated vapour cell to find the relevant resonances. On the two-photon resonant condition we can observe *Electromagnetically Induced Transparency (EIT)*, where we drive atoms directly from the ground to the Rydberg state by probe and coupling laser. Destructive interference between the probe field ($|1\rangle \rightarrow |2\rangle$) and the path of this indirect excitation and the coupling field ($|1\rangle \rightarrow |2\rangle \rightarrow |3\rangle \rightarrow |2\rangle$) reduce the absorption of the probe field [102]. Observing absorption of an atomic vapour is therefore a precise way to characterize three-level systems, which even allows for sub-MHz frequency stabilization for diode lasers [103].

This Chapter starts with a general discussion on atomic transitions in atomic vapours in section 6.1. The subsequent section 6.2 deals with three-level systems, how to observe and model EIT in atomic systems with inverted wavelength ordering and a detection strategy in a Doppler broadened ensemble. Ultimately, in order to find the wavelength of the lower transition we perform a spectroscopy on the three-level system that comprises the two hyperfine states of the ground state and the $5P_{1/2}$ manifold in section 6.3.

6.1 Absorption of light in atomic vapours

In sharp contrast to the environment for cold atom experiments of low temperatures and densities, vapour cell experiments deal with a large ensemble of atoms characterized by broadened transition linewidths. In order to understand absorption of light by atomic transitions in such a vapour cell, we need to understand the basics of transition strengths, their lineshape and spectral broadening, and decoherence mechanisms.

6.1.1 Absorption strength

The transmission of a laser field along $\hat{z}$- direction through an atomic vapour can be written as:

$$\mathcal{T}(z) = \exp\{-\alpha z\} \tag{6.1}$$

The absorption coefficient α from one to another hyperfine level can be obtained from the imaginary part

of the electric susceptibility $\alpha = k \operatorname{Im}\{\chi(\Delta)\}$ of a medium [104]:

$$\alpha(\Delta) = kC_f^2 d^2 \mathcal{N} \frac{1}{2(2\mathcal{I}+1)} \frac{1}{\hbar\epsilon_0} s^I(\Delta) \tag{6.2}$$

Here, k is the wave vector, $\mathcal{N}$ is the atomic number density that depends on the temperature of the atomic vapour, C_f is the transition strength, $s^I(\Delta)$ is the transition lineshape, and $\mathcal{I}$ is the nuclear spin, considered in Chapter 2 for Potassium. Here the dipole moment d is given by:

$$d = \sqrt{3}\sqrt{\frac{3\epsilon_0 \hbar \Gamma \lambda^3}{8\pi^2}} \tag{6.3}$$

Note that $C_f d = \mu$ is the dipole matrix element introduced in chapter 2. In comparison to the D1 and D2 transition in Potassium, the dipole matrix element of the $4S_{1/2} \to 5P_{1/2}$ is more than a factor of 10 lower (as seen in table 2.2): observing absorption on the $4S_{1/2} \to 5P_{1/2}$ is therefore not straightforward.

An important characteristic of atomic transitions is the saturation intensity: if laser fields exceed the saturation intensity on a closed two-level transition, the upper level is macroscopically populated.

$$I_{sat} = 2\pi \frac{hc}{\lambda^3} \frac{\Gamma_T^2}{\Gamma} \frac{1}{1.58} \tag{6.4}$$

Where Γ_T is the total decay rate from the upper level to all lower lying levels and Γ is the decay rate of the transition in scope. This implies that above this level of optical power the absolute signal does not increase, but the noise does. The Rabi frequency can also be expressed as a function of this saturation intensity and the decay rate Γ:

$$\Omega = \Gamma\sqrt{\frac{I}{I_{sat}}} \tag{6.5}$$

Therefore, single laser absorption spectroscopy has an optimal optical Rabi frequency around the linewidth Γ.

6.1.2 Linewidth broadening

The power spectral density (PSD) of a transition with a transition frequency ω_0 with decay rate $\Gamma = \gamma/2$ is given by the Fourier transform with Fourier frequency ω of the exponential $\exp\{\omega_{ij}t\}\exp\{-\gamma t/2\}$ [105]:

$$P(\omega) = P_0 \frac{\gamma/2\pi}{(\omega - \omega_{ij})^2 + (\gamma/2)^2} \tag{6.6}$$

Where P_0 is the total integrated power. This Lorentzian profile gives rise to the minimum linewidth of the transition: the natural linewidth γ. For the $4S_{1/2} \to 5P_{1/2}$ transition in Potassium, this results to a linewidth of $2\pi \cdot 1.16$ MHz [52]. To consider absorption in real media and find the relevant parameters, we have to consider the processes that broaden transition linewidth. In the following, various broadening effects are considered and the magnitude of broadening on a potassium vapour cell at 100°C is estimated.

Doppler broadening

The velocity of atoms with mass m in a cell with temperature T in the direction of the light field applied follow the 1-dimensional Maxwell-Boltzmann velocity distribution:

$$N(v) = \sqrt{\frac{m}{2\pi k_B T}} \exp\left\{ -\frac{mv^2}{2k_B T} \right\} \tag{6.7}$$

Which is a Gaussian distribution. An atom with velocity $\mathbf{v}$ undergoes a shift linear to $|\boldsymbol{k}| = 2\pi/\lambda$ [105]:

$$\omega' = \omega + \mathbf{k} \cdot \mathbf{v} \tag{6.8}$$

This broadens the power PSD with a Gaussian with FWHM:

$$\omega_0 \sqrt{\frac{8 k_B T \ln 2}{mc^2}} \tag{6.9}$$

For a 100 °C Potassium vapour, this is around 400 MHz.

Collisional broadening

Usually vapour cells have an inert buffer gas at atmospheric pressure, which contributes to the broadening [105]. Pressure, or collisional broadening effects take two different forms: through inelastic collisions the excitation energy is transferred to translational energy and through elastic collisions atomic energy levels are distorted causing an energy shift of emitted photon frequency. The former reduces the effective lifetime, broadening the transition in a Lorentzian fashion: the FWHM γ scales linear to the pressure. The latter shifts the frequency. Typical values for shift and broadening are below 100 kHz/Pa for the D2-line in Potassium, dependent on the transition and atomic species of the buffer gas. However, this figure is not known for the transitions we use. In Appendix figure B.2 we show that the potassium-potassium collision rate is kept well under 1 kHz.

Transit broadening

In a vapour cell, the excitation laser beam radius is usually limited to a few millimeter. As the excited state atoms might leave the beam in a time smaller than the excited state lifetime, the effective interaction time of laser and vapour is shorter: this is called the transit broadening. This is closely related to the Maxwell-Boltzmann distribution in radial direction. As this velocity distribution is a Gaussian distribution, the broadening is also Gaussian. The linewidth increases with z_d/v, where z_d is the diameter of the beam and $v_{RMS} = \sqrt{3k_B T/m}$ the root mean square velocity. In the case of a 100°C potassium vapour cell and a beam diameter of 1 mm, this leads to a broadening of about 300 kHz.

Resulting lineshape

Those broadening mechanisms are inhomogeneous: the broadening is different for atoms that are part of an ensemble of different velocity components. Because the aforementioned Gaussian and Lorentzian broadening processes are approximately independent, the resulting lineshape $s^I(\Delta)$ encountered in equation 6.2 becomes a Voigtian already encountered in the linewidths of lasers in section 3.2 [104].

6.1.3 Ground state decoherence

Next to the direct radiative processes from level i to level j described in the previous section, interatomic collisions can alter the spin state of the ground state electron. It was shown that in Rubidium-87 in a vapour cell in a similar Λ-scheme the ground state coherence was limited by the spin-exchange collisions (leading to a finite decoherence Γ_{21})[106]. The mean free path length of a collision process is given by:

$$\lambda = \frac{1}{n\sigma} \tag{6.10}$$

Where the mean free path as a function of the scattering rate τ is given by: $\lambda = v\tau$. At a vapour temperature of $100°$C and the cross-section $1.4 \cdot 10^{-14} \ cm^{-3}$ of the spin-exchange collisions [107], we can calculate the typical frequency of $F = 1 \leftrightarrow F = 2$ processes:

$$\frac{1}{\tau} = vn\sigma \approx 2.1 \text{ kHz} \tag{6.11}$$

Furthermore, wall-collisions occur at around 15kHz in a cell with a diameter of 30 mm and buffer gas collisions occur at higher rates. Those might also contribute to ground state decoherence.

An upper bound of ground state decoherence can be given by a previous experiment that was able to show correlations between two laser fields coupled to the two hyperfine states [108]. One field was chopped at a rate of 24 kHz and this modulation was observed in the other beam. Therefore, the ground state coherence was preserved in the chopping period and a optically pumped population difference between $F = 1$ and $F = 2$ was observed. On the other hand, a lower bound of ground state coherence can be obtained from the Ξ scheme of [109]. Using a coupling beam chopping rate of 3 kHz enables the observation of EIT features: if the ground state decoherence would have been slower than 3 kHz, the atomic population would have been in the uncoupled ground state and no atomic signal would have arisen.

6.2 Three-level systems

The resonant two-photon-transition introduced in Chapter 2 can be modelled by a 3-level system. A precise method to do spectroscopy on a hot vapour is the observation of an EIT feature. EIT can be observed in the three different possible orderings of levels and driven transitions in three level atoms (abbreviated as Λ, V and Ξ). The so-called cascade (Ξ) ordering is depicted in figure 6.1. In the following, we neglect the hyperfine structure, but will comment on the effect of incorporating them.

6.2.1 Optical Bloch Equations

An ideal Ξ-ordered three-level system subject to two (detuned) light fields can be described by the following Hamiltonian in the rotating frame (which eliminates quickly oscillating terms) on the basis $|1\rangle = 4S_{1/2}, |2\rangle = 5P_{1/2}, |3\rangle = nS_{1/2}$ [102]:
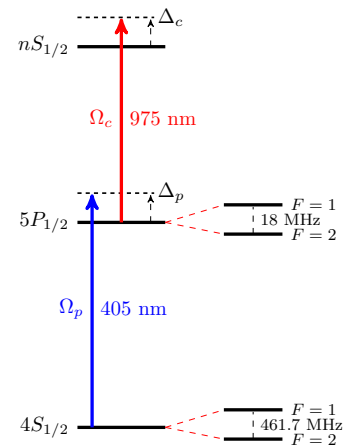

Figure 6.1: *The three-level system in scope, where the levels are coupled with Rabi frequencies Ω_p and Ω_c and blue detuned by Δ_p and Δ_c.*

$$H = \frac{\hbar}{2} \begin{pmatrix} 0 & i\Omega_p & 0 \\ \Omega_p & -\Delta_p & i\Omega_c \\ 0 & \Omega_c & -(\Delta_p + \Delta_c) \end{pmatrix} \tag{6.12}$$

Where the Rabi frequencies and detunings are indicated in figure 6.1. However, this semiclassical Hamiltonian approach disregards dephasing via levels that are not explicitly considered. For a complete description of the open quantum system we resort to a master equation approach for the density matrix [110]:

$$\dot\rho = -\frac{i}{\hbar}\left[\hat H, \rho\right] + \mathcal{L}(\rho) \tag{6.13}$$

Here ρ is the three level density matrix, which has 6 independent parameters ($\rho_{ij} = \rho_{ji}^*$) and Liouvillian $\mathcal{L}$ includes the decay through spontaneous emission ($\Gamma_{ij} = (\Gamma_i + \Gamma_j)/2$) and overall dephasing (γ_{ij}). In this three-level system, the spontaneous decay factor between levels i and j is equal to the previously discussed linewidth Γ_{ij}. To also account for the possibility of dephasing via intermediate levels that are not part of the three-level system, we combine this into independent dephasing terms $\gamma_{ij} = \Gamma_i + \Gamma_j + \gamma_{i,deph}$ [102], which might become exceptionally large in hot vapour cells because of the broadening mechanisms discussed in section 6.1.2 [109]. Applying this to equation 6.13 we obtain the Optical Bloch Equations (OBEs) for the Ξ system:

$$\begin{pmatrix} \dot\rho_{11} \\ \dot\rho_{22} \\ \dot\rho_{33} \\ \dot\rho_{12} \\ \dot\rho_{23} \\ \dot\rho_{13} \end{pmatrix} = \begin{pmatrix} 0 & \Gamma_{21} & \Gamma_{31} & i\Omega_p\hat{\mathrm{Im}} & 0 & 0 \\ 0 & -\Gamma_{21} & \Gamma_{32} & -i\Omega_p\hat{\mathrm{Im}} & i\Omega_c\hat{\mathrm{Im}} & 0 \\ 0 & 0 & -(\Gamma_{31}+\Gamma_{32}) & 0 & -i\Omega_c\hat{\mathrm{Im}} & 0 \\ -i\Omega_p & i\Omega_p & 0 & i(\Delta_p - i\gamma_{12}) & 0 & -i\Omega_c \\ 0 & -i\Omega_c & i\Omega_c & 0 & -i(\Delta_c - i\gamma_{32}) & i\Omega_p \\ 0 & 0 & 0 & -i\Omega_c & i\Omega_p & i(\Delta_p + \Delta_c - i\gamma_{31}) \end{pmatrix} \begin{pmatrix} \rho_{11} \\ \rho_{22} \\ \rho_{33} \\ \rho_{12} \\ \rho_{23} \\ \rho_{13} \end{pmatrix} \tag{6.14}$$

Where we indicate $\hat{\mathrm{Im}}$ as an operator that takes the imaginary component of ρ_{ij} to account for the $(N^2 + N)/2$ complex differential equations, where N is the number of levels involved. Nevertheless, it is still a system of N^2 linear differential equations, as the diagonal components of ρ are real. The diagonal elements of the density matrix ρ_{ii} can be interpreted as occupancies of the levels, whereas the imaginary component of the off-diagonal elements ρ_{ij} are coherences between the level i and j, which relates to the absorption of the field according to equation 6.19.

6.2.1.1 EIT in the weak probe limit

The aforementioned OBEs are usually considered in the weak probe regime to describe EIT: a weak probe beam ($\Omega_p \ll \Omega_c$) leads to a dominant ground state occupation ($\rho_{11} \approx 1, \rho_{22} \approx 0, \rho_{33} \approx 0$). Considering the solution in steady state ($\dot\rho = 0$) gives the following [102]:

$$\rho_{21} \approx \frac{-i\Omega_p/2}{(\gamma_{21} - i\Delta_p) + \frac{\Omega_c^2/4}{\gamma_{31} - i(\Delta_p - \Delta_c)}} \tag{6.15}$$

This leads to the following susceptibility for the $|1\rangle \to |2\rangle$ transition for an atomic ensemble of density n at $T = 0$:

$$\chi(\Delta_p) = -\frac{in}{\epsilon_0 \hbar} \frac{\mu_{12}^2}{\left(\gamma_{21} - i\Delta_p + \frac{\Omega_c^2/4}{\gamma_{31}/2 - i(\Delta_p + \Delta_c)}\right)} \tag{6.16}$$

In equation 6.16 exactly on-resonance ($\Delta_p = \Delta_c = 0$) the imaginary component of the susceptibility reduces and a transparency window arises. We can relate the imaginary component of the susceptibility

to transmission through a sample in $\hat{x}$-direction and density n from equation 6.1.

Nevertheless, abstracting from the weak probe limit, numerical calculation of ρ_{ij} is necessary. We can express χ is terms of ρ through calculating the polarization of the medium [102]. Assuming homogeneous Rabi frequencies for either of the two transitions we can write the expectation value of the polarization of the atomic medium as:

$$\vec{P}(t) = \mathcal{N} \left(\boldsymbol{\mu}_{12}\rho_{21}e^{-i\omega_{21}t} + \boldsymbol{\mu}_{23}\rho_{32}e^{-i\omega_{32}t} + c.c. \right) \tag{6.17}$$

Here, $\boldsymbol{\mu_{ij}}$ is the dipole matrix element between levels j and i. $\vec{P}(t)$ at frequency ω_p relates to the susceptibility as:

$$\vec{P}(t) = \epsilon_0 \chi \vec{E} \tag{6.18}$$

Where $\vec{E}$ is the total electric field and E_p the amplitude of the probe beam. As we are interested in the terms oscillating with frequency ω_{12}, we write:

$$\chi_{12} = \frac{2\mathcal{N}|\vec{\mu}_{12}|}{E_p \epsilon_0} \tilde{\rho}_{12} \tag{6.19}$$

We can thus relate the imaginary component of the susceptibility to transmission through a sample of length z by equation 6.1 [110].

6.2.2 Autler-Townes absorption

When considering an atomic ensemble at $T \neq 0$, Doppler broadening obscures the picture of section 6.2.1.1 as the two-photon resonance condition $\Delta_p + \Delta_c = 0$ becomes different for every velocity class. Hence, we need to consider the Doppler broadening in one dimension from equation 6.7. The two-photon resonance condition becomes:

$$\Delta_p = \left(\frac{1}{\lambda_p} \pm \frac{1}{\lambda_c} \right) v + \Delta_c \tag{6.20}$$

Here, for counterpropagating beams $\pm$ is $-$ and for copropagating $+$. If $\lambda_1 = \lambda_2$ the medium is Doppler-free in a counterpropagating alignment: the resonance condition is v-independent. However, the slope of the resonance condition has a different sign for the inverted ($\lambda_p < \lambda_c$) and non-inverted ($\lambda_p > \lambda_c$) cases.

The atomic absorption signal of the probe beam is a weighted (by equation 6.7) average of all velocity components in the atomic ensemble. To calculate the absorption of the probe beam per velocity component, we have to consider the absorption of single photons of the probe beam as well. Furthermore, at higher Rabi frequencies ($\Omega > \Gamma$) we also have to consider the AC Stark shift. A natural way to describe a three-level system in a strong (near-resonant) coupling light-field is the dressed-state picture [111], where the initial eigenstates $|n, N\rangle$ are characterised by atomic state n and photon number N. Considering the eigenstates of the non-interacting Hamiltonian brings the $|e, N\rangle$ and $|r, N-1\rangle$ eigen-
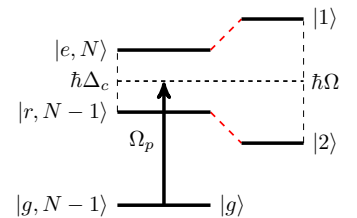

Figure 6.2: *Dressed three-level system by a strong coupling beam with Rabi Frequency Ω_c as seen by the probe beam.* 60

states together. However, adding the interaction between atom and light,
leads to the AC Stark shift between the upper two eigenstates [112]:

$$\Omega = \sqrt{\Omega_c^2 + \Delta_c(v)^2} \tag{6.21}$$

Where the velocity-dependent detuning is $\Delta_c(v) = \Delta_c(0) + \frac{v}{\lambda_c}$ and the center between the two Autler-Townes components is shifted by $-\frac{1}{2}\Delta_c(v)$. Figure 6.2 shows the spectrum of the dressed atom in the non-interacting (left) and the interacting (right) case with their respective eigenstates. The two eigenstates $|e, N\rangle$ and $|r, N-1\rangle$ split into two components with a spacing dependent on the Rabi frequency of the coupling field. The absorption condition of these two Autler-Townes components thus reads:

$$\Delta_p = \frac{v}{\lambda_p} - \frac{1}{2}\left[\Delta_c + \frac{v}{\lambda_c}\right] \pm \sqrt{\Omega_c^2 + \left(\Delta_c + \frac{v}{\lambda_c}\right)^2} \tag{6.22}$$

In order to understand the qualitative differences between the inverted and the non-inverted scheme, we plot the Autler-Townes absorption components, the EIT condition, and the two-level absorption in figure 6.3. In the inverted case of figure 6.3**a)**, for every choice of probe detuning, both the EIT resonance condition is obeyed for some velocity group, as well as the Autler Townes absorption condition. On the contrary, figure 6.3**b)** shows the case of a non-inverted scheme: a window of EIT opens up [112].
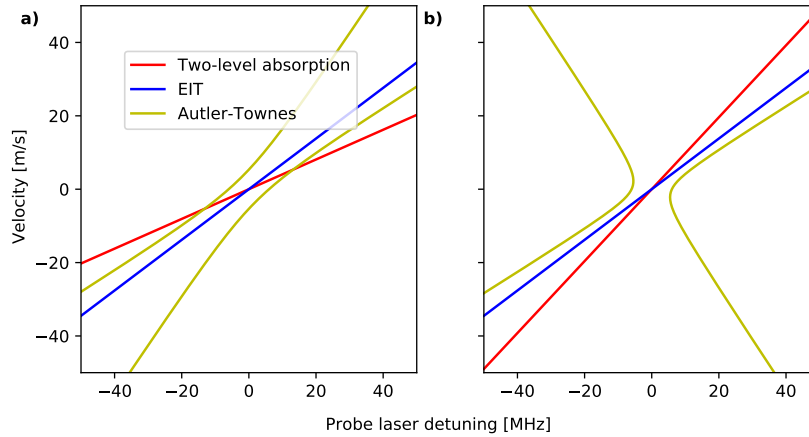

Figure 6.3: *Two-photon (EIT, blue) resonance condition and Autler-Townes components (yellow) for **a)** the inverted scheme and **b)** the non-inverted scheme (right). In the inverted order there is no choice of detuning possible such that there are no simultaneous EIT and ATS absorption conditions, whereas there are around $\Delta_p = 0$ in the non-inverted order. The one-photon absorption (red) shown applies to the two-level absorption condition in absence of a coupling beam. The parameters used are: $\Omega_c = 12$ MHz, $\Omega_p = 1$ MHz, $\Delta_c = 0$, $\lambda_{p,c} = 405, 980$ nm.*

Therefore, when the coupling beam's wavelength is larger than that of the probe beam, it is challenging to observe EIT in a Doppler broadened medium. Nevertheless, the presence of the coupling beam in the vicinity of the upper transition does affect the absorption in the probe beam. By switching the coupling beam on and off, we are able to observe changes in the absorption of the probe beam. This so-called Modulation Transfer Spectroscopy (MTS) is outlined in the next paragraph.

6.2.3 Modulation transfer spectroscopy in Rydberg Ξ scheme

Although we considered the problem of observing EIT in figure 6.3 in an inverted scheme, we used a mostly qualitative argument. For the sake of finding the resonance of the $5P_{1/2} \rightarrow 35S_{1/2}$ transition, we can resort to two methods: performing EIT using a velocity-selective scheme involving both hyperfine groundstates [108] or abstracting from the weak probe approximation [109]. However, as the expected signal is low (see section 6.2.1.1) in the former case, we explore the latter for finding the resonance initially. Both schemes involve Modulation Transfer Spectroscopy (MTS): one optical transition is driven by a beam chopped with frequency f_{chop} and this modulation f_{chop} is observed by monitoring fluorescence or absorption of another optical transition of the same atom. To find the most favourable parameters, we resort to a numerical analysis of the Optical Bloch Equations of section 6.2.

6.2.3.1 Modelling

In order to solve the Optical Bloch Equations (OBEs), we have to solve a system of complex coupled Ordinary Differential Equations (ODEs). We solve this using the Python package **scipy**, which has a procedure **complex_ode** that is able to solve complex ODEs. We use the initial conditions $\rho(t = 0) = \begin{bmatrix} 1 & 0 & 0 & 0 & 0 & 0 \end{bmatrix}$. Although this initial conidition is not realistic when chopping the coupling beam on and off, other physically realistic initial conditions for $\rho(t = 0)$ yield the same result as the initial condition used after convergence is reached. Furthermore, we use the fitted parameters from [109], which has a large Rydberg level dephasing parameter γ_{13}. Due to this, the coherences converge in around 1 μs. As we are interested in the MTS signal by modulating the coupling beam, we want to know the difference in absorption of the probe beam when the coupling beam is on and when it is off. Therefore, we have to solve the OBEs twice for every realization. This parameter $\zeta_{12}(v, \Delta_p)$ that proxies the signal strength for velocity group v is thus defined as:

$$\zeta_{12}(v, \Delta_p) = \rho_{12}^{(on)}(v, \Delta_p) - \rho_{12}^{(off)}(v, \Delta_p) \tag{6.23}$$
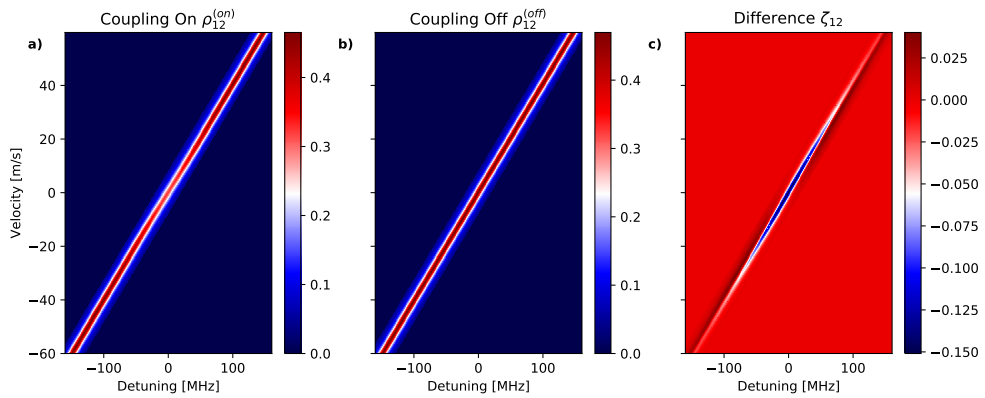

Figure 6.4: *A typical profile of the coherences between levels $|1\rangle$ an $|2\rangle$ as a function of probe beam detuning and atom velocity for both the case where the coupling beam is **a)** on, **b)** off, and **c)** the difference. The Rabi frequencies are $\Omega_p = 5$ MHz and $\Omega_c = 5$ MHz.*

To obtain the final signal strength, we have to integrate $\zeta_{12}(v, \Delta_p)$ over the Maxwell-Boltzmann distribution to obtain the relative signal strength $\zeta_{12}(\Delta)$. However, first we need to obtain the predicted signal

$\zeta_{12}(v, \Delta_p)$ for all velocity groups and for all detunings. We discretize these parameters and we compute $\zeta_{12}(\Delta_p)$. Figure B.1 shows $\zeta_{12}(\Delta_p = 0)$ as a function of the number of points of the discretization: a higher resolution leads to a higher (and correcter signal). Therefore, we require a resolution of at least 200 points per axis. To further reduce the computation time, we use a band of 40 MHz around the two-photon resonance condition if the signal is low in a single pixel band at 40 MHz.

Figure 6.4 shows a typical map of the coherence with $\Omega_p = 5$ MHz, $\Omega_c = 5$ MHz. We observe that the absorption resonance is slightly wider for the case where the coupling beam is on and in the middle the absorption is lower. To obtain the signal strength, we have to integrate those plots over the one dimensional Maxwell-Boltzmann distribution to obtain the relative signal strength ζ as a function of probe beam detuning Δ_p. Figure 6.5 shows $\rho_{12}^{(on,off)}$, ζ_{12} and $\zeta_{12}/\rho_{12}^{(off)}$ as a function of probe detuning for the same parameters as figure 6.4. We observe a FWHM that is approximately 10 times smaller than the Doppler width.
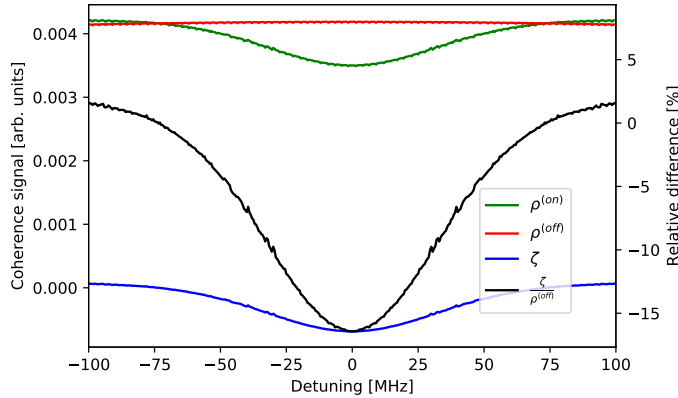

Figure 6.5: *Integrated coherences at $\Omega_p = 5$ MHz, $\Omega_c = 5$ MHz as a function of probe beam detuning with the coupling beam on (green), off (red), the absolute difference ζ (blue) and the relative difference (black). A clear Autler-Townes feature arises.*

As the expected signal is fairly low, we want to find the optimal parameters for the experimental setting. The two Rabi frequencies map out a complicated combination of the Autler-Townes absorption components and an EIT feature. Therefore, we perform a scan for both Rabi frequencies, including the weak probe regime where EIT is usually observed. To finally calculate the strength of the maximum signal at optimal attainable Rabi frequencies, we use equation 6.19 and 6.1 to obtain the differential absorption $\alpha(\zeta)$ over the whole spectroscopy cell length. Figure 6.6 shows the percentual difference in probe beam absorption for a range of Rabi frequencies that is experimentally available. The effective number density in the spectroscopy cell $\mathcal{N}_{eff}$ is obtained from section 6.3.2, which discusses the effect of the chopping frequency on the signal strength. The other vapour cell parameters are given in section 6.3.1.

It is observed that the absorption becomes negative when the probe beam detuning is zero: this is an EIT feature at low probe beam strength and the transparency window between the two Autler-Townes components at higher powers. However, in between the signal strength crosses zero as observed in 6.6 **a)**. Hence, to observe the signal with largest contrast, the EIT-regime is most favourable: small Ω_p and large Ω_c. The strength of the EIT transmission dip is determined by the parameter γ_{31} [112]. As this
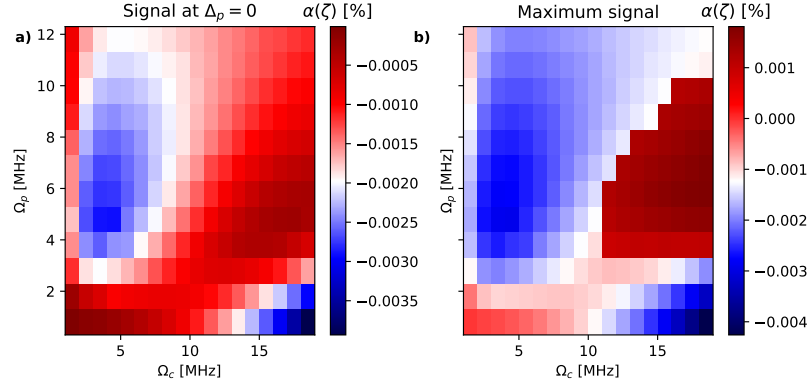
Figure 6.6: *Percentage difference in probe beam absorption ($\alpha(\zeta) \cdot 100$) along the length of the vapour cell at 125°C for the Ξ system for **a)** $\Delta_p = 0$ and **b)** the absolute maximum at any Δ_p.*

parameter is found to be large due to various broadening effects [109], the transmission dip (as observed in figure 6.5) does not exceed 15%. Furthermore, at larger probe beam frequencies and small coupling Rabi frequencies, a EIT signal gradually appears. In addition, a real beam does not have a homogeneous intensity. Operating at Rabi frequencies around the diagonal of figure 6.6 may render the signal even smaller, as various intensity components of the beam have different sign.

6.2.4   Modulation transfer spectroscopy in groundstate Λ system

Similar to the previous section, this section calculates the absorption expected from an MTS scheme by coupling to both hyperfine ground states of the $4S_{1/2}$ manifold and the $5P_{1/2}$ state with two fields detuned by the hyperfine splitting. The scheme is displayed in figure 6.7. This calculation is relevant for two reasons:
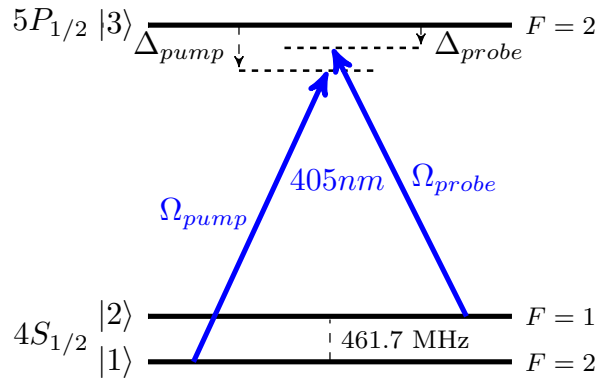

Figure 6.7: *Lambda scheme using two ground states from the same hyperfine manifold coupled by a coherent laser pair at 405 nm with Rabi frequencies Ω_{pump} and Ω_{probe} to the upper $5P_{1/2}$ state.*

- In order to perform the EIT-scheme of section 6.2.3, we first of all need to find the $4S_{1/2} \rightarrow 5P_{1/2}$ resonance.

- The relative difference between the absorption strengths of the Ξ scheme with respect to the Λ

scheme tells us how strong the expected signal should be, given the measured strength of the Λ scheme.

There are some important differences to the cascade configuration shown previously. First of all, our light fields originate from the same laser and are only detuned by the hyperfine splitting: their mutual coherence length is around 1 meter. Secondly, there is hence only a single detuning δ_p, which is equally affecting both lasers. Furthermore, the two-photon resonance condition in a Λ scheme has a different sign compared to the Ξ scheme. In our case, the two-photon resonance condition is only obeyed for $v = 0$:

$$\Delta_{pump} = +\frac{v}{\lambda_{pump}} + \delta_p = -\frac{v}{\lambda_{probe}} + \delta_p = \Delta_{probe} \qquad (6.24)$$

Because the two-photon resonance condition only holds for a single velocity component, in a hot vapour it is obscured by absorption at other velocity groups (see section 6.2.2): an EIT feature can not be observed. Nevertheless, a spectroscopy as precise as the linewidth of the upper state ($5P_{1/2}$) can be performed. In our analysis we neglect the crosswise effect due to the limited hyperfine splitting of the ground state: the probe beam slightly drives the coupling transition and the other way around. However, they do so at very distinct velocity components. The OBEs for the Λ system have been solved, where we added the ground state decoherence term $\Gamma_{12} = \Gamma_{21} = 20$ kHz to have a symmetric effect between $|1\rangle$ and $|2\rangle$: in a vapour cell without light fields both states are equally populated. Figure 6.8 shows the counterpart of figure 6.5 for the Λ-system. The same parameters used for the Xi-scheme for the vapour cell and effective number density are used here.
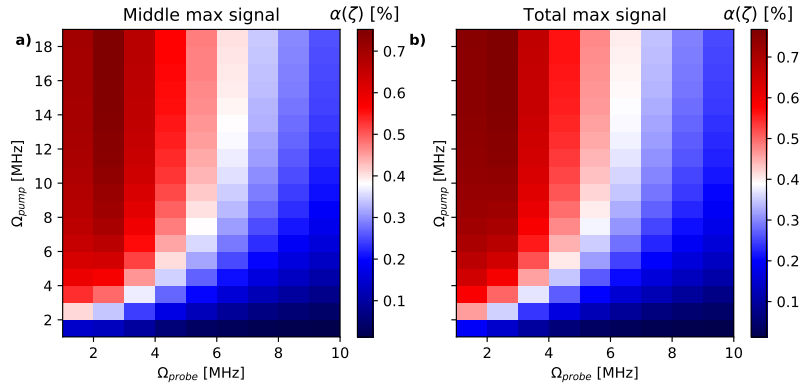

Figure 6.8: *Percentage difference in probe beam absorption ($\alpha(\zeta) \cdot 100$) along the length of the vapour cell at $125°C$ for the Λ ground state system for **a)** $\Delta_p = 0$ and **b)** the absolute maximum at any Δ_p.*

In the Λ system, the maximal MTS signal always occurs at $\Delta_p = 0$: hence, figure 6.8 **a)** and **b)** are the same.

6.2.5   Comparison of Rabi frequencies

We choose the $35S_{1/2}$ level as our Rydberg level of interest, as Rydberg excitation to this level has been shown by [59] in the non-inverted wavelength ordering (see section 2.2). This level is sufficiently low that other states are not in the vicinity and has relatively high Rabi frequencies. The optimal Rabi frequencies for both schemes can be considered in figure 6.6 and 6.8. For the Λ system the optimal Rabi frequency

for the probe beam is around 2-3 MHz, whereas the pump beam needs to be sufficiently strong (around 10 MHz). This corresponds to a power of less than 100 µW in the probe and 1 mW in the pump beam. For the Ξ system the optimal Rabi frequency for the probe beam is around 5 MHz, whereas the coupling beam needs to be around 5 MHz as well. This corresponds to a power of 200 µW in the probe and 10 mW in the coupling beam.

Given the optimal Rabi frequencies found, the signal of the Λ ground state scheme is 200 times larger than that of the Ξ Rydberg scheme, corresponding to 23 dB. As discussed in section 6.3.2, the Λ scheme also works at larger chopping frequencies, which shows a larger effective number density. However, the analysis here considers absolute absorption, which is not a perfect measure of signal strength with respect to noise. At larger optical powers, amplitude noise of the laser increases the photodiode noise floor and it might be wise to limit powers.

6.3   Inverted scheme EIT in a hot vapour cell

In this section, the settings sketched in section 6.2 are considered in a vapour cell. First of all, the vapour cell is considered in section 6.3.1 and the effect of chopping on the effective number density is described in 6.3.2. Subsequently, 6.3.3 discusses the setup used and section 6.3.4 shows the realization of MTS on the Λ scheme.

6.3.1   Vapour cell

To consider the MTS technique in a realistic setting, one needs to consider the temperature of the cell and thus the chopping frequencies to use. At temperatures larger than the melting point of Potassium (63.5°C), the vapour pressure and thus also the number density $\mathcal{N}$ strongly increase as a function of temperature [113, 114].
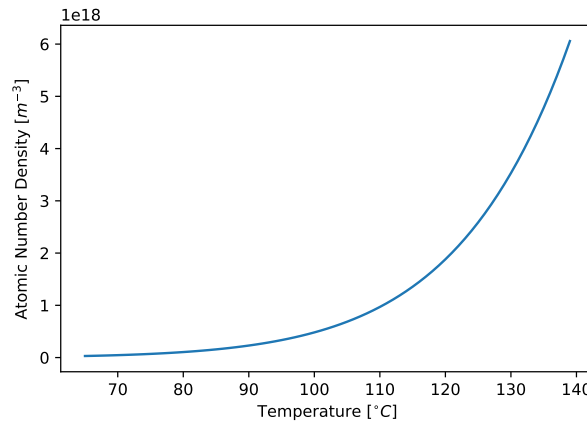

Figure 6.9: *Atomic number density of potassium per cubic meter as a function of vapour cell temperature.*

Figure 6.9 shows the number of atoms per cubic meter as a function of temperature: we operate our aluminium-foil wrapped vapour cell at around 125°C. The vapour cell is approximately cylindrical with a length of 5 cm and a radius of 3 cm with counterpropagating beams aligned at a waist of 1.0 mm. The

number density in the cell is approximately $2 \cdot 10^{18}$ m^{-3}, leading to around $2 \cdot 10^{11}$ atoms within the beam diameter.

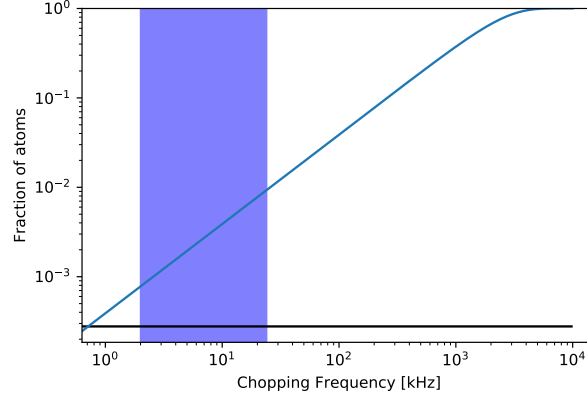### 6.3.2   Chopping frequencies

Figure 6.10: *Fraction of atoms that is sufficiently slow to not pass the beam within $1/f_{chop}$. The blue-shaded area denotes the possible range for the ground state decoherence, whereas the black-line provides a lower bound to the fraction of atoms by considering wall collisions (equation 6.25).*

As the atoms have a finite temperature and thus a finite velocity, the optimal absorption signal is limited: if we modulate a laser field at frequency f_{chop} and the atom traverses the beam in a time $\tau \ll 1/f_{chop}$, we don't obtain a signal. This not only affects the atomic dynamics through the transit broadening, but also reduces the signal that can be obtained in a modulation transfer spectroscopy. The fraction of atoms sufficiently slow to remain in the beam size of 1 mm during one chopping period as a function of beam chopping frequency in figure 6.10.

However, assuming wall collisions are ballistic: their v_z doesn't change: this might lead to a resonance for particular chopping frequencies - or averaging for very low chopping frequencies. A lower bound for the atoms in scope is then:

$$V_{beam}/V_{cell} = \left(\frac{R_{Beam}}{R_{cell}} \right)^2 \approx 1/3600 \tag{6.25}$$

This is noted as the black horizontal line in figure 6.10. It appears that this lower bound is not limiting given the chopping frequencies that we use. The blue-shaded area in figure 6.10 shows the range of the estimated ground state decoherence in section 6.1.3. As discussed in section 6.1, the ground state decoherence happens at a rate lower than 24 kHz and due to broadening effects the Rydberg state linewidth is likely larger than that by considering the fitted γ_{31} from [109]. As this frequency is lower than than the cut-off frequency in figure 6.10, the maximum signal is substantially lower than calculated in section 6.2.3.1. Therefore, in the Ξ scheme, as we couple to only one of the ground states, chopping of the coupling beam needs to be sufficiently slow to prevent the population of the uncoupled ground state. Considering the chopping rate of 3 kHz [109], approximately 1 in 1000 atoms contribute to the signal: $\mathcal{N}_{eff} = \mathcal{N}/1000$. On the contrary, in the Λ scheme, the chopping frequency needs to exceed the ground state decoherence rate, as we couple to both hyperfine ground states. Therefore, the upper bound of chopping frequencies is much higher for the Λ scheme.

6.3.3 Setup

Figure 6.11 shows the setup for two-photon excitation in a vapour cell. The sources, coupled free-space from figure 4.5 and coupled through a fiber from figure 4.7, are described in chapter 4. The 405 nm beam is split into two separate beams by a Polarizing Beam Splitter (PBS) cube and afterwards the polarization is turned vertical to the base of the AOMs. The AOMs (Gooch and Housego I-M110-3C10BB-3-GH27) have an optimal behaviour at an RF input of 110 MHz. As we overcome the hyperfine splitting (461.7 MHz) by two AOMs, we need to use both AOMs in double pass-configuration (the AOMs have an optimal operating frequency of 105 MHz). The AOM's ± 1 orders need to be spatially separated. Initially polarization-separation by a polarizing beam cube before and a $\lambda/4$ waveplate was set up. However, the diffraction efficiency of the specific AOM model was very dependent on polarisation, leading to a poor double pass efficiency. To resolve this, the beams need to be spatially separated by a retroreflector mirror after the AOM, and the backreflected beam needs to be outcoupled by a D-shaped mirror in vertical direction. A double-pass AOM efficiency of around 50% is achieved for the probe branch, whereas it is substantially lower for the pump branch due to a large angle for optimal AOM efficiency that led spatially separation to reduce the efficiency. To improve this, another AOM should be used or a horizontal retrore-flectror with a perfect 90° angle.

Both 405 nm beams are aligned on the spectroscopy cell, in counterpropagating configuration: as the wavelengths of both beams are near identical, this makes the spectroscopy near Doppler-free (see equation 6.20). The pump beam is diverging due to an optional $f = -50$ mm concave lens, which makes overlapping the beams easier. By turning the polarization by a $\lambda/2$ waveplate on the other side of the cell, we can couple out the probe branch and detect it. The 980 nm (coupling) laser was carefully overlapped with the pump branch by using a dichroic mirror (DMLP550) that transmits 980nm and reflects 405 nm. Overlap between the probe beam and the coupling beam was ensured by fiber coupling the probe beam into the fiber where the 980 nm enters. By adjusting the beam-shaping elements shown in 6.11 and the collimation lens of the 980 nm fiber outcoupler, we are able to realize beams with waists of 0.5 mm and 0.6 mm. To ensure a temperature of 125° by using resistive heating elements, the vapour cell had to be wrapped in aluminium foil. The 405 nm beam that originates from the probe branch impinges on the homebuilt photodiode. To prevent the 980 nm light to impinge the photodiode, a 405±50 nm bandpass filter was used in front of the photodiode. To retrieve modulated signals, we use a lock-in amplifier (Femto LIA-MV-200-H)

The presented setup is able to realize the Λ and Ξ systems introduced in this Chapter. Control over the optical powers and chopping frequencies is possible by tuning the RF power supplied to the AOM drivers. To sweep the detuning of the ECDLs, the large sidebands discussed in section 3.3.3 can be swept.

6.3.4 Groundstate Λ system

The Λ-configuration of 6.7 was explored using the probe and pump branch in figure 6.11. Unfortunately no data with the lock-in amplifier could be taken as the transfer cavity was not locked, as the 770 nm laser was used for another purpose. In a previous stage, a mixer was used to demodulate the MTS signal. Figure 6.13 shows a part of the sweep over detuning frequency over the $4S_{1/2} \rightarrow 5P_{1/2}$ resonance chopping the pump AOM at 250 kHz. The resonance was found at 809.6707(3) nm. The accuracy is limited by the wavemeter used.

We observe three peaks, where the two outer peaks are approximately spaced by the hyperfine splitting.
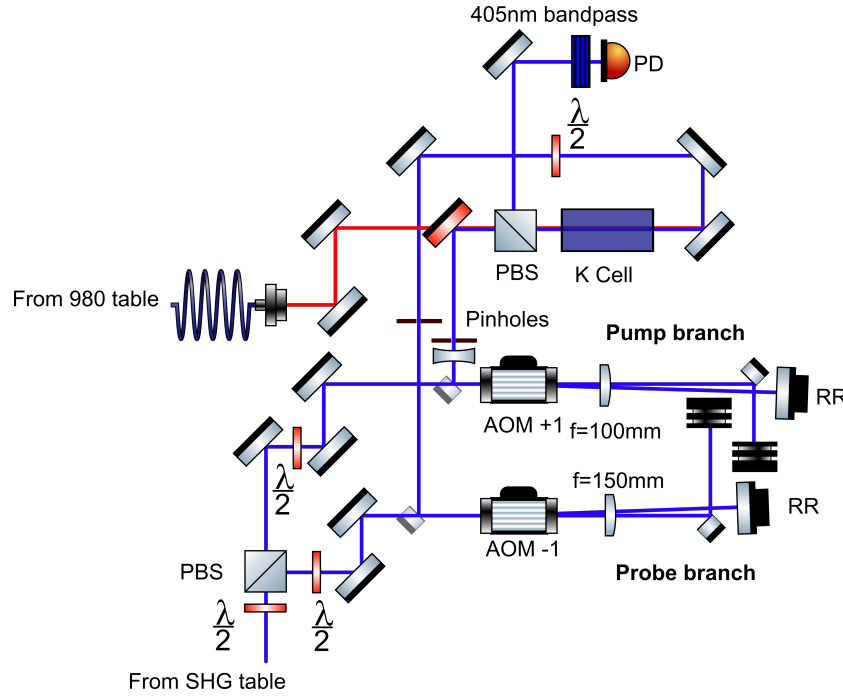
Figure 6.11: *Setup of the two-photon setup onto a Potassium vapour cell, which allows to probe the Λ and Ξ system considered in section 6.2. The setup is seeded by the setups from figure 4.5 and 4.7. RR - Retroreflecting mirror, PBS - Polarizing Beam Splitter.*
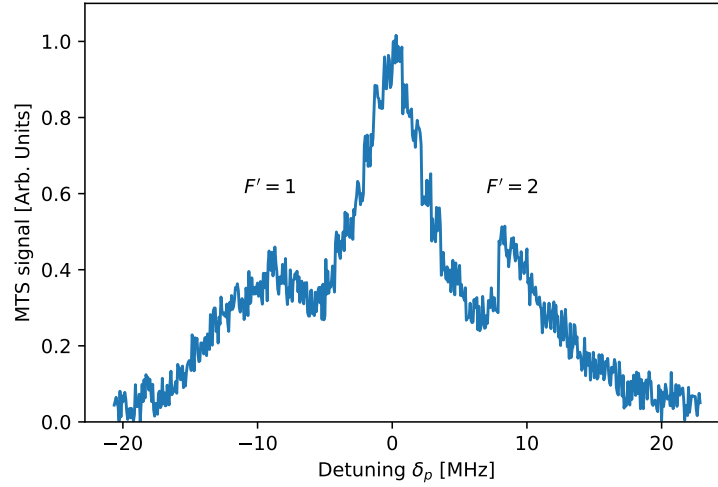

Figure 6.12: *Probe beam MTS signal $\zeta(\delta_p)$ as a function of shared probe and pump beam detuning δ_p. Approximate Rabi frequencies are $Omega_{probe} = 10MHz$ and $Omega_{pump} = 5MHz$. The scan is obtained using a chopping frequency of 250 kHz and a vapour cell temperature of $125°C$.*

This can be explained by the hyperfine structure (splitting of 18.1 MHz) of the $5P_{1/2}$ state. Moreover, a large velocity component ($v = cf_{hf}/f_{probe}$) shows an inverted level structure of probe and pump: the

velocity component $v = c\frac{f_{hf}}{f_{probe}}$ interchanges the role of probe and pump beam as it shifts their frequency by $\pm f_{hf}$ This gives 4 distinct contributions around the two-photon resonance in the lab frame. The resonance of the probe (thin line) and pump (thick line) beam of both the $v = 0$ and the $v = c f_{hf}/f_{probe} \approx$ 182 m s^{-1} component to both hyperfine levels is shown in figure 6.13. This gives rise between a splitting of 18 MHz between the two contributions that address $F' = 1$ and the two contributions that address $F' = 2$. Exactly in the middle a cross-over of the two contributions arises.
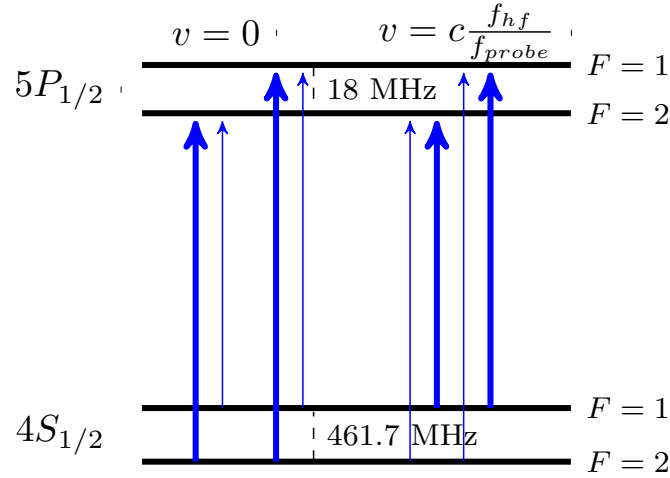

Figure 6.13: *Resonance condition in the Λ scheme forvelocity components $v = 0$ and $v = c\frac{f_{hf}}{f_{probe}}$. Thin lines refer to the probe beam whereas thick lines refer to the pump beam.*

The asymmetry in figure 6.13 arises due to a difference in strength between the two: the transition to the $F' = 2$-state is somewhat stronger [109].

Concluding remarks

In this Chapter it was argued why it is hard to observe an EIT spectroscopy using the $5P_{1/2}$ as an intermediate state. First of all, the transition strength is simply lower than that of e.g. the D1 and D2 transitions. In addition, as the inverted wavelength ordering has Doppler components that absorb light simultaneously with Doppler components that fulfill the EIT condition, the usually sharp EIT feature is obsured. To observe small atomic signals, Modulation Transfer Spectroscopy by using two atomic transitions is regularly used in combination with a lock-in amplifier.

As the upper two-photon transition was not observed after various spectroscopy attempts, it was decided to calculate the optimal parameters to find the $5P_{1/2} \to nS_{1/2}$ transition and compare it to the strength of the transition between both hyperfine ground states and the $5P_{1/2}$. It was found that for a large range of Rabi frequencies for both beams the expected MTS signal is small and even reverses sign, which is detrimental for non-homogeneous beams. Furthermore, it was shown that the Λ scheme is at least 23 dB stronger than the Ξ scheme, which is even more at larger chopping frequencies. Nevertheless, the $4S_{1/2} \to 5P_{1/2}$ transition was characterized at a chopping frequency of 250 kHz with a center wavelength of 809.6707(3) nm.

Chapter 7

Conclusion

This thesis discussed the construction of a two-photon inverted scheme Rydberg setup, superseding and extending the setup built and characterised in [60]. Interference Filter-based ECDLs at 810 nm and 980 nm were constructed to replace grating-based Littrow lasers. The ECDL at 980 nm fulfilled the requirements of a large Mode-Hop Free Tuning Range (7 GHz), single mode lasing and sufficient power to seed a Tapered Amplifier enabling up to 450 mW fiber-coupled light. On the contrary, two diodes at 810 nm with different gain profiles did not show single mode behaviour for all settings of current and temperature, leading to a reduced mode-hop free tuning range of 4 GHz. To characterise the behaviour of those lasers, a procedure has been written that sweeps laser current and temperature and calculates the AC and DC components of the ECDL output. Although outcoupler reflectivities were increased to enhance the feedback supplied back to the laser diode, limiting behaviour persisted for the 810 nm ECDLs. After an SHG stage, it was possible to achieve a power of more than 100 mW of 405 nm light.

To reduce the detrimental effect of phase noise on Rydberg excitation decoherence, a filter cavity with a sufficiently narrow transmission profile has been constructed, with a measured finesse of 9796. Unfortunately, the transmission of a 980 nm ECDL was only 41%, attributable to intracavity losses. As this would lead to an output power of less than 20 mW, the Tapered Amplifier would not be properly seeded, which leads to a higher unwanted Amplified Spontaneous Emission background and lower power in the cavity mode. Nevertheless, the constructed cavity has been used to measure the phase noise of a 980 nm laser. The phase noise measurement corresponded well to an alternative measurement using the in-loop error signal. An integrated phase noise ϕ_{RMS} of 33 mrad has been measured down to 100 kHz.

To characterize the atomic transitions to be used, a vapour cell spectroscopy was set up. Initially it was aimed for to perform a velocity-selective Electro-magnetically Induced Transparency (EIT) scheme. However, finding the $5P_{1/2} \rightarrow 35S_{1/2}$-transition showed to be challenging. Therefore, the optical Bloch equations were solved to find the optimal Rabi frequencies to observe either an EIT signal or an Autler-Townes transmission window. Although using with an MTS scheme to characterize the $4S_{1/2} \rightarrow 5P_{1/2}$ transition was observed at a wavemeter value of 809.6707(3) nm, the $5P_{1/2} \rightarrow 35S_{1/2}$ was not observed.

Outlook

First of all, the laser system built at 980 and 405 nm is suitable for two-photon excitation of Rydberg atoms as single mode behaviour, low linewidth, and moderate powers have been achieved. However,

the 810 nm laser showed limiting behaviour both in terms of mode-hop free tuning range and long-run mode stability. As it was identified that neither a lack (through Lang-Kobayashi dynamics) nor an excess (through spatial hole burning) of feedback was not the cause of this, it is most likely that the diode limits this behaviour. Although it was able to perform scans of the laser frequency, trying different diodes that show more favourable behaviour might be useful.

Secondly, the filter cavity has a sufficient finesse to filter laser phase noise at relevant Fourier frequencies. However, to use this specific cavity, an injection lock is required. In such a setup, the cavity-filtered ECDL output would be used to provide feedback to a bare laser diode. This stimulated emission of the injection-locked laser diode has similar spectral characteristics as the seed laser.

Ultimately, an EIT feature to perform a spectroscopy on the $35S_{1/2}$ level was not observed. To find the right wavelength for the transition the optimal Rabi frequencies from this thesis could be used to increase the Alternatively, it might be worthwhile to do this in a cold atom environment, rather than the Doppler-broadened hot vapour cell. However, this requires the alignment of the excitation lasers onto the tweezer trapped atoms within the vacuum chamber. In this way, the one-photon setup based on the 1150 nm ECDL built, can be used to find the right wavelength of $4S \rightarrow nP$ transitions, given the knowledge of the $4S_{1/2} \rightarrow 5P_{1/2}$ transition obtained in this thesis.

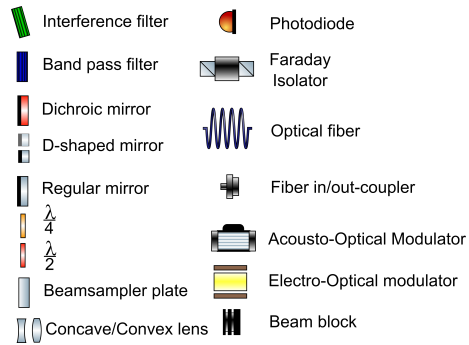# Appendices

Appendix A

Legend to setups

Figure A.1: *Legend for the most common elements of the figures of setups relevant to the main text of this thesis*
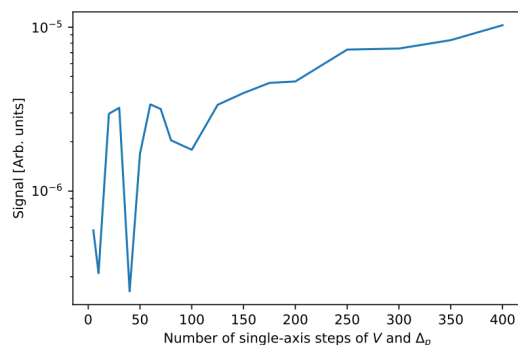
Appendix B

OBE additional figures

Figure B.1: *It appears that at least 200x200 resolution in v and Δ_p is required to obtain a converging solution of $\chi(\Delta_p = 0)$: The fact that for low resolution we underestimate stems from the effect that for three-level system the resonance is broader than for the two-level system: around the midpoint the three level signal is accurately captured, but the two level signal is underestimated because we only take 1 value on the peak ridge, which is likely to be off-centered and thus does not capture the maximum very well. The parameters here were $\Omega_p = 13$ MHz, $\Omega_c = 9$ MHz, $\Delta_c = 0$.*
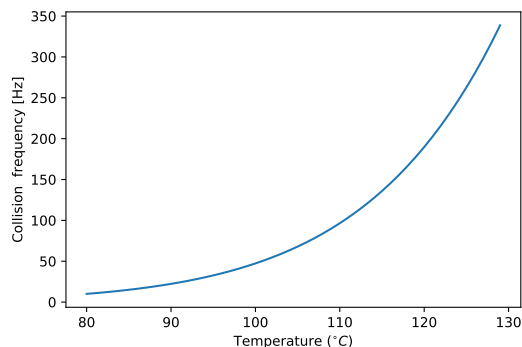

Figure B.2: *Calculated Potassium-Potassium collision rate in a hot vapour cell.*

Appendix C
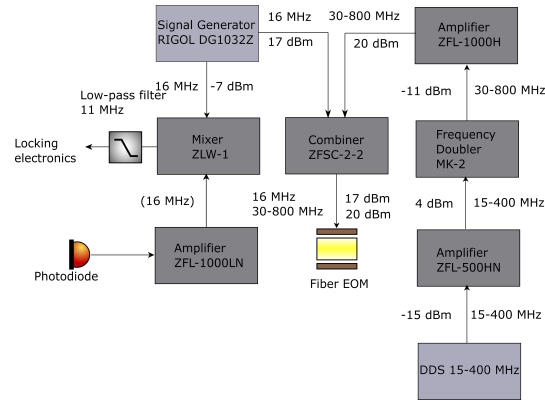
PDH electronics

Figure C.1: *Locking electronics circuit for the 980 nm ECDL to the ULE cavity. Dark gray rectangles are from Mini-Circuits, except for the ENA-210T, which is from RFBay. The locking circuit for the 810 nm ECDL to the ULE is similar, but uses a Mini-Circuits ZFL-1000H+ which amplifies up to 20 dBm, which suffices for the 810 nm fiber EOM, but not for the 980 nm fiber EOM.*

Bibliography

[1] Georgescu, I., Ashhab, S., and Nori, F. *Reviews of Modern Physics* **86**, 153 (2013).

[2] Davis, K. B., Mewes, M. O., Andrews, M. R., van Druten, N. J., Durfee, D. S., Stamper-Kurn, D. M., and Ketterle, W. *Phys. Rev. Lett.* **75**, 3969–3973 (1995).

[3] Anderson, M. H., Ensher, J. R., Matthews, M. R., Wieman, C. E., and Cornell, E. A. *Science* **269**, 198–201 (1995).

[4] DeMarco, B. and Jin, D. S. *Science* **285**(5434), 1703–1706 (1999).

[5] Chu, S., Bjorkholm, J. E., Ashkin, A., and Cable, A. *Phys. Rev. Lett.* **57**, 314–317 (1986).

[6] Bloch, I. *Nat. Phys.* **1**, 23–30 (2005).

[7] Kim, H., Lee, W., Lee, H.-g., Jo, H., Song, Y., and Ahn, J. *Nature Communications* **7** (2016).

[8] Bakr, W., Gillen, J., Peng, A., Fölling, S., and Greiner, M. *Nature* **462**, 74–7 (2009).

[9] Cheuk, L. W., Nichols, M. A., Okan, M., Gersdorf, T., Ramasesh, V. V., Bakr, W. S., Lompe, T., and Zwierlein, M. W. *Phys. Rev. Lett.* **114**, 193001 (2015).

[10] Greiner, M., Mandel, O., Esslinger, T., Hänsch, T. W., and Bloch, I. *Nature* **415**(6867), 39–44 (2002).

[11] Simon, J., Bakr, W., Ma, R., Tai, M., Preiss, P., and Greiner, M. *Nature* **472**, 307–12 (2011).

[12] Lahaye, T., Menotti, C., Santos, L., Lewenstein, M., and Pfau, T. *Reports on Progress in Physics* **72**(12), 126401 (2009).

[13] Lukin, A., Rispoli, M., Schittko, R., Tai, M., Kaufman, A., Choi, S., Khemani, V., Leonard, J., and Greiner, M. *Science* **364**, 256–260 (2019).

[14] Eckardt, A., Hauke, P., Soltan-Panahi, P., Becker, C., Sengstock, K., and Lewenstein, M. *Europhysics Letters* **89**(1), 10010 (2010).

[15] Cooper, N. R., Dalibard, J., and Spielman, I. B. *Rev. Mod. Phys.* **91**, 015005 (2019).

[16] Schauß, P. *Unpublished* (2017).

[17] Chin, C., Grimm, R., Julienne, P., and Tiesinga, E. *Rev. Mod. Phys.* **82**, 1225–1286 (2010).

77

[18] Nicholson, T., Campbell, S., Hutson, R., Marti, G., Bloom, B., Mcnally, R., Zhang, W., Barrett, M., Safronova, M., Strouse, G., Tew, W., and Ye, J. *Nature Communications* **6**, 6896 (2015).

[19] Phillips, W. D. *Rev. Mod. Phys.* **70**, 721–741 (1998).

[20] Salomon, G., Fouché, L., Wang, P., Aspect, A., Bouyer, P., and Bourdel, T. *Europhysics Letters* **104**(6), 63002 (2013).

[21] Gröbner, M., Weinmann, P., Kirilov, E., and Nägerl, H.-C. *Phys. Rev. A* **95**, 033412 (2017).

[22] Muldoon, C., Brandt, L., Dong, J., Stuart, D., Brainis, E., Himsworth, M., and Kuhn, A. *New Journal of Physics* **14** (2012).

[23] Grünzweig, T., Hilliard, A., McGovern, M., and Andersen, M. *Nature Physics* **6** (2011).

[24] Barredo, D., Léséleuc, S., Lienhard, V., Lahaye, T., and Browaeys, A. *Science* **354** (2016).

[25] Kumar, A., Wu, T.-Y., Giraldo, F., and Weiss, D. *Nature* **561**, 83–87 (2018).

[26] Saffman, M., Walker, T. G., and Mølmer, K. *Rev. Mod. Phys.* **82**, 2313–2363 (2010).

[27] Weimer, H., Müller, M., and Lesanovsky, I. *Nature Physics* **89**(6), 382–388 (2010).

[28] Urban, E., Johnson, T., Henage, T., Isenhower, L., Yavuz, D., Walker, T., and Saffman, M. *Nature Physics* **5** (2008).

[29] Isenhower, L., Urban, E., Zhang, X. L., Gill, A. T., Henage, T., Johnson, T. A., Walker, T. G., and Saffman, M. *Phys. Rev. Lett.* **104**, 010503 (2010).

[30] Schauß, P., Cheneau, M., Endres, M., Fukuhara, T., Hild, S., Omran, A., Pohl, T., Gross, C., Kuhr, S., and Bloch, I. *arXiv preprint 1209.0944* (2012).

[31] Zeiher, J. *Realization of Rydberg-dressed quantum magnets*. PhD thesis, Ludwig-Maximilians-Universität, München, (2017).

[32] Barredo, D., Labuhn, H., Ravets, S., Lahaye, T., Browaeys, A., and Adams, C. S. *Phys. Rev. Lett.* **114**, 113002 (2015).

[33] Labuhn, H., Barredo, D., Ravets, S., Léséleuc, S., Macri, T., Lahaye, T., and Browaeys, A. *Nature* **534**, 667–670 (2016).

[34] Bernien, H., Schwartz, S., Keesling, A., Levine, H., Omran, A., Pichler, H., Choi, S., Zibrov, A., Endres, M., Greiner, M., Vuletic, V., and Lukin, M. *Nature* **551**, 579–584 (2017).

[35] Barredo, D., Lienhard, V., Leseleuc, S., Lahaye, T., and Browaeys, A. *Nature* **561**, 79082 (2018).

[36] Omran, A., Levine, H., Keesling, A., Semeghini, G., Wang, T. T., Ebadi, S., Bernien, H., Zibrov, A. S., Pichler, H., Choi, S., Cui, J., Rossignolo, M., Rembold, P., Montangero, S., Calarco, T., Endres, M., Greiner, M., Vuletić, V., and Lukin, M. D. *Science* **365**(6453), 570–574 (2019).

[37] Barredo, D., Lienhard, V., Scholl, P., de Léséleuc, S., Boulier, T., Browaeys, A., and Lahaye, T. *arXiv preprint 1908.00853* (2019).

[38] Jau, Y.-Y., Hankin, A., Keating, T., Deutsch, I., and Biedermann, G. *Nature Physics* **12**, 71–74 (2016).

[39] Gaul, C., DeSalvo, B. J., Aman, J. A., Dunning, F. B., Killian, T. C., and Pohl, T. *Phys. Rev. Lett.* **116**, 243001 (2016).

[40] Zeiher, J., Bijnen, R., Schauß, P., Hild, S., Choi, J.-Y., Pohl, T., Bloch, I., and Gross, C. *Nature Physics* **12**, 1095–1099 (2016).

[41] Arias, A., Lochead, G., Wintermantel, T. M., Helmrich, S., and Whitlock, S. *Phys. Rev. Lett.* **122**, 053601 (2019).

[42] Borish, V., Marković, O., Hines, J., Rajagopal, S., and Schleier-Smith, M. *arXiv preprint 1910.13687* (2019).

[43] Goldschmidt, E. A., Boulier, T., Brown, R. C., Koller, S. B., Young, J. T., Gorshkov, A. V., Rolston, S. L., and Porto, J. V. *Phys. Rev. Lett.* **116**, 113001 (2016).

[44] Pupillo, G., Micheli, A., Boninsegni, M., Lesanovsky, I., and Zoller, P. *Phys. Rev. Lett.* **104**, 223002 (2010).

[45] Glaetzle, A. W., Dalmonte, M., Nath, R., Gross, C., Bloch, I., and Zoller, P. *Phys. Rev. Lett.* **114**, 173002 (2015).

[46] de Léséleuc, S., Barredo, D., Lienhard, V., Browaeys, A., and Lahaye, T. *Phys. Rev. A* **97**, 053803 (2018).

[47] Levine, H., Keesling, A., Omran, A., Bernien, H., Schwartz, S., Zibrov, A., Endres, M., Greiner, M., Vuletić, V., and Lukin, M. D. *Phys. Rev. Lett.* **121**(12), 123603 (2018).

[48] Madjarov, I. S., Covey, J. P., Shaw, A. L., Choi, J., Kale, A., Cooper, A., Pichler, H., Schkolnik, V., Williams, J. R., and Endres, M. (2020).

[49] Seaton, M. J. *Reports on Progress in Physics* **46**(2), 167–257 (1983).

[50] Gallagher, T. *Rydberg Atoms*. Cambridge University Press, Cambridge, (2014).

[51] Beterov, I., Ryabtsev, I., Tretyakov, D., and Entin, V. *Physical Review A* **79**, 052504 (2009).

[52] Šibalić, N., Pritchard, J., Adams, C., and Weatherill, K. *Computer Physics Communications* **220**, 319–331 (2017).

[53] Browaeys, A. and Lahaye, T. *Interacting Cold Rydberg Atoms: A Toy Many-Body System*, 177–198. Springer International Publishing, Cham (2016).

[54] Henkel, N. *Rydberg-dressed Bose-Einstein condensates*. PhD thesis, Technische Universitä Dresden, Dresden, (2013).

[55] Scully, M. O. and Zubairy, M. S. *Quantum Optics*. Cambridge University Press, (1997).

[56] Audi, G., Kondev, F. G., Wang, M., Huang, W., and Naimi, S. *Chinese Physics C* **41**(3), 030001 (2017).

[57] Tiecke, T. G. (2011).

[58] Peper, M., Helmrich, F., Butscher, J., Agner, J. A., Schmutz, H., Merkt, F., and Deiglmayr, J. *Phys. Rev. A* **100**, 012501 (2019).

[59] Arias, A., Helmrich, S., Schweiger, C., Ardizzone, L., Lochead, G., and Whitlock, S. *Opt. Express* **25**(13), 14829–14839 (2017).

[60] Hirthe, S. Master's thesis, Ludwig-Maximilians-Universität, München, (2018).

[61] Thompson, D. J. and Scholten, R. E. *Review of Scientific Instruments* **83**(2), 23107 (2012).

[62] Martin, M. J. *Quantum Metrology and Many-Body Physics: Pushing the Frontier of the Optical Lattice Clock*. PhD thesis, University of Colorado, Denver, (2013).

[63] Buus, J. and Amann, M.-C. *Tunable Laser Diodes and Related Optical Sources*. John Wiley & Sons, Bridgewater, (2005).

[64] Peters, F. H. and Cassidy, D. T. *J. Opt. Soc. Am. B* **8**(1), 99–105 (1991).

[65] Lawrence, J. S. *Diode Lasers with Optical-Feedback, Optical-Injection, and Phase-Conjugate Feedback*. PhD thesis, Macquarie University, Sydney, (2000).

[66] Zhang, T., Poizat, J.-P., Grelu, P., Roch, J.-F., Grangier, P., Marin, F., Jost, V., Levenson, M., and Giacobino, E. *Quantum and Semiclassical Optics: Journal of the European Optical Society Part B* **7**, 601 (1999).

[67] Marin, F., Giacobino, E., Zhang, T., Poizat, J.-P., Roch, J.-F., and Grangier, P. *Phys. Rev. Lett.* **75**, 4606–4609 (1996).

[68] Zhang, Y., Miyakawa, S., Kasai, K., Okada-Shudo, Y., and Watanabe, M. *Applied Physics B* **108**(1), 39–42 (2012).

[69] Hadley, G. *IEEE Journal of Quantum Electronics* **22**(3), 419–426 (1986).

[70] Tkach, R. and Chraplyvy, A. *Journal of Lightwave Technology* **4**(11), 1655–1661 (1986).

[71] Lang, R. and Kobayashi, K. *IEEE Journal of Quantum Electronics* **16**(3), 347–355 (1980).

[72] Dutta, S., Elliott, D., and Chen, Y. *Applied Physics B: Lasers and Optics* **106** (2011).

[73] Domenico, G. D., Schilt, S., and Thomann, P. *Appl. Opt.* **49**(25), 4801–4807 (2010).

[74] Tarallo, M. G. *Development of a Strontium optical lattice clock*. PhD thesis, Universita' degli Studi di Pisa, (2009).

[75] Patil, D. S. *Semiconductor laser diode technology and applications*. IntechOpen, London, (2012).

[76] Henry, C. *IEEE Journal of Quantum Electronics* **18**(2), 259–264 (1982).

[77] Hall, J. L. and Zhu, M. (1992).

[78] Cladé, P. *Oscillations de Bloch d'atomes ultrafroids et mesure de la constante de structure fine*. PhD thesis, Université Paris 6, Paris, (2004).

[79] Torrance, J. S., Sparkes, B. M., Turner, L. D., and Scholten, R. E. *Opt. Express* **24**(11), 11396–11406 (2016).

[80] Black, E. *American Journal of Physics* **69**, 79–87 (2001).

[81] Fox, R. W., Oates, C. W., and Hollberg, L. W. In *Cavity-Enhanced Spectroscopies,* van Zee, R. D. and Looney, J. P., editors, volume 40 of *Experimental Methods in the Physical Sciences*, 1 − 46. Academic Press (2003).

[82] Cook, E., Martin, P., Brown-Heft, T., Garman, J., and Steck, D. *The review of scientific instruments* **83**, 043101 (2012).

[83] Zorabedian, P. and Trutna, W. R. *Opt. Lett.* **13**(10), 826–828 (1988).

[84] Baillard, X., Gauguet, A., Bize, S., Lemonde, P., Laurent, P., Clairon, A., and Rosenbusch, P. *Optics Communications* **266**(2), 609 − 613 (2006).

[85] Rana, F., editor. *Semiconductor Optoelectronics*, volume 1 of *11*, New York, (2018). Cornell University.

[86] Gallaher, N. *Narrow linewidth, diode laser pumped, solid state lasers*. PhD thesis, University of St Andrews, (1994).

[87] Adema, J. Internal documentation, (2019).

[88] Staub, E. Master's thesis, Ludwigs-Maximilians-Universität, München, (2019).

[89] Heumier, T. A. *Mode Hopping in Semiconductor Lasers*. PhD thesis, Montana State University, Bozeman, (1992).

[90] Blakemore, J. S. *Journal of Applied Physics* **53**(10), 123–181 (1982).

[91] Ludvigsen, H., Tossavainen, M., and Kaivola, M. *Optics Communications* **155**(1), 180–186 (1998).

[92] Schmid, F., Weitenberg, J., Hänsch, T. W., Udem, T., and Ozawa, A. *Opt. Lett.* **44**(11), 2709–2712 (2019).

[93] Chen, M., Meng, Z., Wang, J., and Chen, W. *Opt. Express* **23**(5), 6803–6808 (2015).

[94] Walpole, J. N. *Optical and Quantum Electronics* **28**(6), 623–645 (1996).

[95] Boyd, R. W. *Nonlinear Optics, Third Edition*. Academic Press, Inc., USA, 3rd edition, (2008).

[96] Risk, W., Gosnell, T., and Nurmikko, A. *Compact Blue-Green Lasers*. Cambridge University Press, Cambridge, 1 edition, (2003).

[97] Nikogosyan, D. N. *Applied Physics A: Materials Science & Processing* **52**(6), 359–368 (1991).

[98] Kogelnik, H. and Li, T. *Appl. Opt.* **5**(10), 1550–1567 (1966).

[99] Adema, J. Internal documentation, (2019).

[100] Sterr, U., Legero, T., Kessler, T., Schnatz, H., Grosche, G., Terra, O., and Riehle, F. *Proc SPIE* **7431** (2009).

[101] Hrabina, J., Hola, M., and Cíp, O. *Sensors (Basel)* **13**, 2206–19 (2013).

[102] Fleischhauer, M., Imamoglu, A., and Marangos, J. P. *Rev. Mod. Phys.* **77**, 633–673 (2005).

[103] Abel, R. P., Mohapatra, A. K., Bason, M. G., Pritchard, J. D., Weatherill, K. J., Raitzsch, U., and Adams, C. S. *Applied Physics Letters* **94**(7), 071107 (2009).

[104] Siddons, P., Adams, C. S., Ge, C., and Hughes, I. G. *Journal of Physics B: Atomic, Molecular and Optical Physics* **41**(15), 155004 (2008).

[105] Demtröder, W. *Atoms, Molecules, and Photons*. Springer, New York, 3rd edition, (2018).

[106] Shuker, M., Firstenberg, O., Sagi, Y., Ben-kish, A., Davidson, N., and Ron, A. *Phys. Rev. A* **78**, 063818 (2008).

[107] Happer, W. *Rev. Mod. Phys.* **44**, 169–249 (1972).

[108] Xu, W. and DeMarco, B. *Phys. Rev. A* **93**, 011801 (2016).

[109] Chen, T.-L., Chang, S.-Y., Huang, Y.-J., Huang, Y.-C., Suen, T.-H., Kuan, T.-Y., Shy, J.-T., and Liu, Y.-W. *arXiv preprint 1912.06741* (2019).

[110] Gavryusev, V., Signoles, A., Ferreira-Cao, M., Zürn, G., Hofmann, C. S., Günter, G., Schempp, H., de Saint-Vincent, M. R., Whitlock, S., and Weidemüller, M. *Journal of Physics B: Atomic, Molecular and Optical Physics* **49**(16), 164002 (2016).

[111] Cohen-Tannoudji, C. N. *The Autler-Townes Effect Revisited*, 109–123. Springer New York, New York, NY (1996).

[112] Shepherd, S., Fulton, D. J., and Dunn, M. H. *Physical Review A* **6**(54), 5393–5399 (1996).

[113] Edmondson, W. and Egerton, A. *Proceedings of the Royal Society of London. Series A, Containing Papers of a Mathematical and Physical Character* **113**(765), 520–533 (1927).

[114] Alcock, C. B., Itkin, V. P., and Horrigan, M. K. *Canadian Metallurgical Quarterly* **23**(3), 309–313 (1984).

Acknowledgements

A master student talking to PhD students about their setup must sound a lot like a patient explaining his symptoms to a medical doctor. In my memory, this became clare on a morning in April. After a one-minute rage about a laser that does not want to lock, Nikolaus "Dr. House" Lorenz noted immediately: "You have a polarization problem". After turning a waveplate the patient (me) was left dumbfounded that his insurmountable problem could have a cure that easy. Connecting symptoms to diagnoses taught me a lot about optics and quantum computing, but also about electronics and technical aspects. For all those diagnoses, I would like to thank to following:

- Rudolf Gross and Immanuel Bloch for the formal supervision.

- Christian Gross for accepting me as a student on the Potassium experiment, the supervision and the always useful suggestions after encountering problems.

- The thorough proofreading by Lorenzo Festa and Lea-Marina Steinert (up to the nitty gritty details), which really made me think twice about the whole manuscript.

- Lorenzo Festa, Nikolaus Lorenz, Phillip Osterholz, Lea-Marina Steinert and Robin Eberhard for the help and the possibility to ask for support, explanations, and also the sometimes stubbornly rejected suggestions (and of course the 10 and 4 o'clock coffee talks about whatever not).

- Petar Bojović for the interesting discussions on the ECDLs and Anton Wallner for cooperatively building the 810 nm ECDLs

- Everyone of the Bloch group that played kicker (physical activity is healthy) after lunch breaks, which was an entertaining outlet for laser-related frustrations. I am sure got a bit better.

- Anton Mayer and Olivia Mödl, who produced the many parts that we needed over the course of a year and for generating an admiration for the technical occupation, by pointing out how limited the technical knowledge of the average Physics student is.

- My colleagues at the ifo institute, where I worked once a week, for valueing me and involving me in research that involves a completely different aspect of the world and motivating me to apply for a PhD position at the LMU.

- I want to greatly thank my friends, who took the effort to hang out far from home and shared my joy in visiting places around Europe and my colleagues of the Campus Cneipe who helped me grasp German language better but also the fun nights of friendship.

- Being far away from beloved ones is not always easy, and finding a balance between Groningen, Zagreb and München posed a challenging temporal and spatial constraint. My parents, although seeing your only child a few weeks a year, seemingly supported me going abroad to study, and find out what I want in life.

- Last and foremost, I would like to thank my Maja for the unconditional support and great moments over the last year. I hope the many videocalls made up for my physical absence.

I noted over the year that I am not born to be an experimental physicist as overcoming technical issues appeared more a joy of my colleagues than of myself. Although I won't continue my career in the field most of the aforementioned persons work in, I learned many useful skills that I can use in my further life.